THÈSE DE DOCTORAT
DE L'UNIVERSITÉ DE LILLE

Laboratoire de Mécanique multiphysique et multiéchelle - FRE 2016

Présenté par

YuLong Zhang

pour obtenir le grade de

DOCTEUR DE L'UNIVERSITÉ LILLE

Domaine

GÉNIE CIVIL

Sujet de la thèse

Contribution à l'étude de déformation et de rupture des roches par une approche discrète

Soutenue le 18 septembre 2018 devant le jury composé de :

M.J JIANG	**PR**	Université de Tongji, Chine	*Rapporteur*
Z.Y YIN	**HDR**	Ecole Centrale Nantes	*Rapporteur*
Y. JIA	**MCF**	LaMcube, Université de Lille	*Membre*
F. NICOT	**HDR**	IRSTEA	*Membre*
J.F. SHAO	**PR**	LaMcube, Université de Lille	*Co-encadrant*
G. De SAXCE	**PR**	LaMcube, Université de Lille	*Directeur de thèse*

LaMcube-L'UNIVERSITÉ DE LILLE

Abstract

In this work, a new bond model with nonlinear shear failure criterion is first proposed and implemented in the particle flow code for describing mechanical behavior of isotropic cohesive granular materials such as sandstone. A large number of compression tests have been performed on two and three-dimensional samples. The results show that the effect of confining pressure on compressive strength and failure pattern is well described by the proposed bond model. Effects of loading path and the intermediate principal stress on deformation and failure have been also investigated. After further extending parameters with respect to elastic and strength, two bond models: the proposed bond model and the improved smooth join model, are coupled to character the anisotropy of strength and deformation in anisotropic cohesive materials such as sedimentary rocks. A series of conventional triaxial compression tests with different loading paths have been performed and numerical results are in good agreement with experimental data, especially for elastic response and strength properties. The failure mode transformation between weakness layer and rock matrix under different confining pressures has been well described. Furthermore, the proposed bond model has been extended to study hydraulic fracturing process in cohesive materials. A representative hydraulic fracture propagation process has been presented. Influences of different factors, such as confining pressure, fluid viscosity and fluid injection rate, on hydraulic fracture extension have been investigated. Finally, we have developed a dimensional reconstruction method of block shape irregularity and studied its effects on block impacts using an energy based approach.

Keywords: New bond model, DEM, Particle flow code, Sandstone, Shale, Hydraulic fracture, Rockfall

Résumé

Dans ce travail, un nouveau modèle de liaison avec critère de rupture de cisaillement non linéaire est d'abord proposé et mis en œuvre dans le code d'écoulement des particules pour décrire le comportement mécanique des matériaux granulaires cohérents isotropes tels que le grès. Un grand nombre de tests de compression ont été effectués sur des échantillons à deux et trois dimensions. Les résultats montrent que l'effet de la pression de confinement sur la résistance à la compression et le modèle de rupture est bien décrit par le modèle de liaison proposé. Les effets du chemin de chargement et de la contrainte principale intermédiaire sur la déformation et la rupture ont également été étudiés. Après avoir étendu les paramètres relatifs à l'élasticité et à la force, deux modèles de liaison: le modèle de liaison proposé et le modèle de joint lisse amélioré, sont couplés pour caractériser l'anisotropie de la résistance et de la déformation des matériaux cohésifs anisotropes tels que les roches sédimentaires. Une série d'essais de compression triaxiale conventionnels avec différents trajets de chargement ont été réalisés et les résultats numériques sont en bon accord avec les données expérimentales, en particulier pour les propriétés de réponse élastique et de résistance. La transformation du mode de défaillance entre la couche de faiblesse et la matrice rocheuse sous différentes pressions de confinement a été bien décrite. En outre, le modèle de liaison proposé a été étendu pour étudier le processus de fracturation hydraulique dans les matériaux cohésifs. Un processus de propagation de fracture hydraulique représentatif a été présenté. Les influences de différents facteurs, tels que la pression de confinement, la viscosité du fluide et le débit d'injection du fluide, sur l'extension de la fracture hydraulique ont été étudiées. Enfin, nous avons développé une méthode de reconstruction dimensionnelle de l'irrégularité de forme de bloc et étudié son effets sur les impacts de bloc en utilisant une approche basée sur l'énergie

Mots clés: Nouveau modèle de liaison, DEM, code de flux de particules, grès, fracture hydraulique, chutes de pierres

Acknowledgement

Firstly, I would like to express my most sincere gratitude to my main supervisor Professor Jian-fu SHAO. It is his precious guidance, unlimited patience, selfless help and constant encouragement that continuously supported me to finish this work in the last four years. It is my honor to be one of his students.

Secondly, I am deeply grateful to Professor Gery De SAXCE for his helps that provide me a chance to stay University Lille for four years. I am also thankful to MR. Zaobao LIU for his useful advice.

Thirdly, thanks to my friends in LaMcube selflessly providing their help and support during my stay in Lille. I will cherish the delight moment that we shared knowledge, skills and fun at together in the past time.

Finally, I also want to express my great thanks to my parents and sisters for their unconditional trust, support and encouragement in my academic career.

Thanks for all.

Table Of Contents

General Introduction

Most rocks are cohesive materials. Their microstructure is mainly composed of mineral grains, interfaces between grains and voids. Their mechanical behaviors are complex and strongly dependent on loading history, such as volumetric dilatancy, transition from brittle to ductile behavior, induced damage, initial and induced anisotropy. As an alternative way to classical plastic and damage models, discrete modeling provides an efficient method to capture those complex mechanical properties. In this context, a cohesive rock material is replaced by an equivalent discrete medium composed of grains and voids. In general, the inter-granular contact interfaces in cohesive rocks are bonded, generating a certain macroscopic tensile strength and uniaxial compression strength. Further, the deformation and failure of materials are inherently related to bonds breaking or contact interfaces cracking and grain crushing. The main issue is to capture the physical processes at the contact scale and their impacts on macroscopic responses. As one of the widely used discrete approaches, the particle flow model that has the ability to simultaneously consider the combined role of mineral grains and voids, will be adopted in this work to investigate the mechanical behavior of cohesive rocks, especially for capturing the failure evolution from the diffused micro cracks to forming local failure band. In this method, the used bond model of interface between particles plays an important role in describing the mechanical behavior of cohesive materials. Thus, the main outline of the work is first to propose a suitable bond model for isotropic cohesive materials, and then to extend it for materials with structural anisotropy. Furthermore, this bond model is extended to hydromechanical coupling for modeling hydraulic fracturing in saturated rocks.

On the other hand, rockfall is another common engineering problem. It refers to the

phenomenon of bedrock fragments rapidly moving downward from a cliff face. During the rockfall process, there is always colliding between the falling block and the slope. The colliding mechanism of rockfall is complicated and influenced by many factors such as falling block morphology, surface characteristics, incident angle, block volume, block strength and other bedrock properties. Due to the fact that classical continuum methods have difficulty in solving non-continuous motions, the discrete method is here used to investigate these effects of various factors, such as the morphological randomness and irregularity of impacting rocks, which have so far rarely been taken into account in rockfall analysis. Hence, this work is also devoted to three-dimensional modeling of small falling rocks in block impact analysis in energy view using the particle flow method.

This present dissertation consists of four chapters: The first chapter concerns the investigation of sandstone which can be treated as isotropic cohesive materials. The focus is on describing the strength nonlinearity observed in experiments. A new bond model with nonlinear failure criterion will be first proposed and implemented in the particle flow code to describe both tensile and shear cracking of bonded contact interfaces for a large range of stress state. Then, fully three-dimensional simulations will be performed on both cylindrical and cubic samples for different loading paths. Effects of confining pressure and loading path on deformation behavior and failure process of typical bonded granular materials will also be clearly demonstrated.

The second chapter is devoted to study on strength and deformation of anisotropic cohesive materials. The nonlinear failure criterion used in simulation of sandstone will be first introduced in two bond models, the bond model and the smooth joint model, to consider tensile and shear failure respectively in weakness layer and rock matrix for a large range of normal stress. A useful procedure for characterizing micro-structure of anisotropic material with two bond models is proposed, and corresponding stiffness and strength parameters related to deformation and failure are further developed. This developed method will be implemented in the Particle Flow Code and applied to model a typical anisotropic sedimentary rock. Moreover, the effect of the intermediate principal stress on anisotropy will also be predicted.

In the third chapter, the break down pressure as well as failure evolution process of cohesive material in hydraulic fracture tests will be described using the particle flow code with the proposed bond model. Effects of confining pressures, fluid viscosity and injection rate on mechanical behavior are respectively investigated.

In the last chapter, the discrete method will be applied to rockfall analysis. Three-dimensional modeling of small falling rocks in block impact analysis in energy view using the particle flow method is mainly conducted in this part. The restitution coefficient of rockfall collision is introduced from the energy consumption mechanism to describe rockfall-impacting properties. Three-dimensional reconstruction of falling block is conducted with the help of spherical harmonic functions that have satisfactory mathematical properties, such as orthogonality and rotation invariance. Furthermore, the effects of rockfall morphology, surface characteristics, velocity, and volume, colliding damping and relative angle on restitution coefficients will be further investigated.

Chapter I

Effects of confining pressure and loading path on deformation and strength of cohesive granular materials: a three-dimensional DEM analysis

Contents

Acta Geotechnica
https://doi.org/10.1007/s11440-018-0671-4

RESEARCH PAPER

Effects of confining pressure and loading path on deformation and strength of cohesive granular materials: a three-dimensional DEM analysis

Yulong Zhang[1,2] · Jianfu Shao[1,2] · Zaobao Liu[2] · Chong Shi[1] · Géry De Saxcé[2]

Received: 27 May 2017 / Accepted: 17 April 2018

Abstract
This paper is devoted to numerical analysis of strength and deformation of cohesive granular materials. The emphasis is put on the study of effects of confining pressure and loading path. To this end, the three-dimensional discrete element method is used. A nonlinear failure criterion for inter-granular interface bonding is proposed, and it is able to account for both tensile and shear failure for a large range of normal stress. This criterion is implemented in the particles flow code. The proposed failure model is calibrated from triaxial compression tests performed on representative sandstone. Numerical results are in good agreement with experimental data. In particular, the effect of confining pressure on compressive strength and failure pattern is well described by the proposed model. Furthermore, numerical predictions are studied, respectively, for compression and extension tests with a constant mean stress. It is shown that the failure strength and deformation process are clearly affected by loading path. Finally, a series of numerical simulations are performed on cubic samples with three independent principal stresses. It is found that the strength and failure mode are strongly influenced by the intermediate principal stress.

Keywords Bonded contact model · Cohesive granular materials · Contact interface · Discrete element method (DEM) · Loading path · Sandstone

1 Introduction

A large number of engineering materials, in particular rock-like and cement-based materials, can be investigated in the class of cohesive granular materials. Their microstructure is mainly composed of mineral grains and voids. Unlike cohesionless granular materials such as powders and soils, the inter-granular contact interfaces in cohesive materials are bonded, generating a nonvanished macroscopic tensile strength and uniaxial compression strength. In this class of materials, the physical processes of deformation and failure are inherently related to bonds breaking or contact interfaces cracking and grain crushing. A great number of experimental, theoretical and numerical studies on various granular materials have been so far conducted. For instance and without giving an exhaustive list of reported studies, a thermomechanical constitutive model for cemented granular materials has been proposed using quantifiable internal variables by [5, 32]. Yang and Luo [34] have explored the relationship between critical state and particle shape for cohesionless granular materials. Kruyt and Rothenburg [16] have provided a micromechanical study of dilatancy in granular materials. Duriez et al. [9] have tried to identify the micromechanical nature of stresses in triphasic granular media with interfaces. La Ragione [18] has investigated the incremental response of a stressed and anisotropic granular material under loading and unloading conditions. Sibille et al. [31] have established a plastic theory for granular materials based on discrete mechanics. Borja et al. [1] have investigated shear band in sand with spatially varying density. The localization in a granular material has also been studied using a micromechanical prediction by [19].

✉ Jianfu Shao
jian-fu.shao@polytech-lille.fr

[1] Key Laboratory of Ministry of Education for Geomechanics and Embankment Engineering, Hohai University, Nanjing 210098, China

[2] Laboratory of Mechanics of Lille, University of Lille, 59650 Villeneuve d'Ascq, France

Published online: 30 April 2018

The main issue is to capture the physical processes at microscopic scale and their impacts on macroscopic responses. For this purpose and with the fast progress of computing technology, various discrete elements methods have made a great progress during the last decades. The common feature of these methods is to replace a continuum medium by an equivalent discrete medium. Without giving an exhaustive list of different approaches, two main families of discrete media have been generally adopted, an assembly of spherical grains for granular morphology and a set of polygon blocks for polycrystal structure. For granular materials, the particle flow model is one of the widely used discrete approaches and has been extended to cohesive granular materials. Cundall and Strack [4] have first proposed a discrete numerical model and developed a particle flow code (PFC) for cohesionless granular materials. Potyondy and Cundall [27] have then developed a bonded-particle model for rock-like cohesive materials. Different extensions and improvements have been successively achieved by various authors in order to improve the quality of numerical results in terms of volumetric dilation, cracks propagation, post-peak strain softening and strain localization process [24, 39]. In particular, Jiang et al. [14] have proposed a rigid plastic element for contact interfaces and an efficient approach to capturing bonding effect in naturally microstructural sands. Jiang et al. [15] have also studied shear behavior and strain localization in cemented sand by two-dimensional distinct element method. References [7, 29] have proposed a new contact model to improve the simulated ratio of unconfined compressive strength to tensile strength in bonded-particle models. Mehranpour and Kulatilake [23] have examined and compared six major intact rock failure criteria in predicting intact rock strength under the true-triaxial stress condition using original bond models in a particle flow approach. Further, He et al. [11] have also conducted a detailed comparison of nine intact rock failure criteria using polyaxial intact coal strength data obtained through PFC simulations. Other applications of discrete element methods to rock-like materials have also been reported [3, 33]. The discrete element method has also been used to modeling fracturing process in cohesive materials [6, 20, 28]. In some studies, the discrete element method has also been applied to modeling anisotropic rocks [8, 17, 38] and jointed rock mass [10, 22, 26, 36]. Using a DEM method, Zhu et al. [40] have tried to define a common critical state for both localized and diffuse failure modes in cohesionless soil-like materials. Some similar discrete approaches have been developed for modeling cracking and fracturing in cohesion rock-like materials and compared with discrete element method [37].

In most previous studies using particle flow code, two-dimensional simulations for cohesionless materials [2, 21] as well as three-dimensional calculations for rocks [23, 25] are limited in using the same bond models, such as the contact bond model (CBM) and parallel bond model (PBM), to simulate failure behaviors of cohesive granular materials under different stress states. There is no detailed discussion so far on whether the original bond models are perfectly appropriate to describe the mechanical responses of cohesive granular materials under a large range of confining pressure and for different kinds of loading paths. In general, conventional triaxial compression tests on cylindrical samples have been considered in most studies. Further, the effect of the intermediate principal stress on deformation and failure of granular materials has not been sufficiently studied. The new contribution of the present study is then to partially complete the shortcoming of previous studies. To this end, a new failure criterion will first be proposed to describe both tensile and shear cracking of bonded contact interfaces for a large range of stress state. Fully three-dimensional simulations will then be performed on both cylindrical and cubic samples for different loading paths. Effects of confining pressure and loading path on deformation behavior and failure process of typical bonded granular materials will be clearly demonstrated. For convenience, the following stress and stress sign convention will be adopted throughout the paper: compressive stresses and strains are counted as positive quantities.

2 Failure criterion for a new bond model

In cohesive granular materials, the macroscopic strength and deformation are essentially controlled by the local behavior of inter-granular interfaces. For rock-like materials, the interfaces are generally bonded. Two types of bond models, i.e., the contact bond model (CBM) and parallel bond model (PBM), are used in standard particle flow code (PFC3D) [12, 13, 27]. There are three basic components involved in general bond model: (1) contact stiffness behavior, (2) bonding behavior and (3) slip behavior. Similarly, a brief introduction of the newly proposed bond model is provided in describing these three components as below.

2.1 Contact stiffness behavior

The deformation and failure of interfaces are closely related to local stresses. For calculation of local stresses at contacts, two main contact stiffness models (the linear and Hertz model) in PFC3D are, respectively, used to describe elastic and non-elastic behaviors of contacts, depending on the mechanical properties of the studied entities. Thus, in this work, the linear model is applied to represent the

elastic behavior of cohesive materials. The relationships between force and contact stiffness are illustrated by the following equations:

$$F_{\mathrm{n}} = k_{\mathrm{n}} u_{\mathrm{n}} \tag{1}$$

$$\Delta F_{\mathrm{s}} = -k_{\mathrm{s}} \Delta u_{\mathrm{s}} \tag{2}$$

where the values of F_{n}, k_{n} and u_{n} are, respectively, the normal force, normal stiffness and displacement at the contact; ΔF_{s}, k_{s} and Δu_{s} denote, respectively, the shear force, shear stiffness and relative displacements. Note that the normal stiffness, k_{n}, is a secant modulus that relates to the total displacement and force. The shear stiffness, k_{s}, on the other hand, is a tangent modulus that relates to the incremental displacement and force.

2.2 Failure criterion of new bonding behavior

The failure status of interfaces can be determined by comparing the calculated local stresses and bond strength at a contact. In failure analysis of interfaces, two debonding processes should be taken into account, i.e., the tensile cracking and frictional sliding. For tensile cracking, the failure condition is generally dependent on the normal tensile stress. The frictional sliding process is otherwise more complex, depending on both normal stress and tangential shear stress. The local shear strength of interfaces is strongly influenced by the normal stress. Thus, two types of bond models of interfaces, i.e., the contact bond model (CBM) and parallel bond model (PBM), are generally adopted for analyzing cohesive materials in PFC. In the CBM, the tensile and shear strength are directly regarded as a constant. Different from the PBM, the shear strength is described by a linear Mohr–Coulomb type criterion which is defined by the frictional angle and cohesion. The shortcoming of these criterions is that the effect of normal stress on the shear strength cannot be correctly described for a large range of normal stress.

Therefore, a new criterion is proposed here. The tensile failure occurs when the normal contact force $F_{\mathrm{t,f}}$ reaches the tensile strength φ_{nt}. For the shear cracking, the shear strength generally increases nonlinearly with normal pressure. The failure envelope is a convex curved surface. For the sake of simplicity, the shear strength of interfaces is here approximated by a bilinear function of normal contact force. When the normal contact force F_{n} is less than the transition threshold φ_{ncr}, the shear strength is defined by the cohesion φ_{s} and frictional angle ϕ_1. When the normal force is higher than φ_{ncr}, a second frictional angle ϕ_2 is introduced with $\phi_2 < \phi_1$ to define the shear strength. The peak shear strength envelope is presented in Fig. 1. The failure criterion for contact interface is then expressed in the following form:

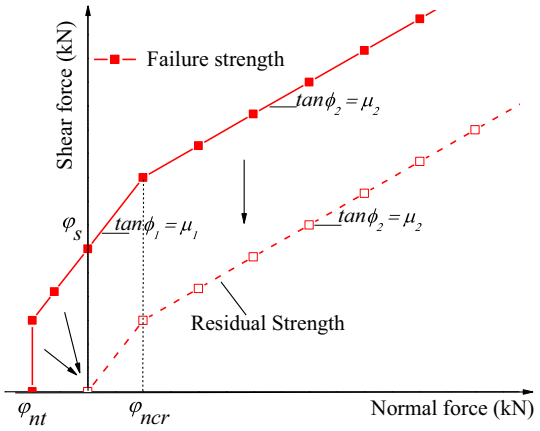

Fig. 1 Peak and residual strength envelopes of bonded contact model

$$F_{\mathrm{n}} = \varphi_{\mathrm{nt}}, \quad \text{tensile failure} \tag{3}$$

$$F_{\mathrm{s,f}} = \begin{cases} 0, & F_{\mathrm{n}} < \varphi_{\mathrm{nt}} \\ \varphi_{\mathrm{s}} + F_{\mathrm{n}} \tan\phi_1, & \varphi_{\mathrm{nt}} \le F_{\mathrm{n}} \le \varphi_{\mathrm{ncr}}, \ \text{shear failure} \\ \varphi_{\mathrm{s}} + \varphi_{\mathrm{ncr}}(\tan\phi_1 - \tan\phi_2) & \\ \quad + F_{\mathrm{n}} \tan\phi_2, & F_{\mathrm{n}} \ge \varphi_{\mathrm{ncr}} \end{cases} \tag{4}$$

where $F_{\mathrm{s,f}}$ denotes the peak shear strength, φ_{s} the shear force applied to the interface.

2.3 Slip behavior after bond failure

When the contact surface is broken, the tensile strength is completely vanished. However, due to the frictional force along rough interfaces, there is a residual shear strength which increases with compressive normal stress. Further, it is generally observed that the frictional angle is barely affected by interface failure, while the cohesion is drastically reduced. In the present model, it is assumed that the residual interface cohesion is reduced to zero, while the same value of frictional angles can be used for the residual shear strength. The residual strength envelope is shown in Fig. 1, and the following criterion is formulated.

$$F_{\mathrm{s,r}} = \begin{cases} 0 & , \quad F_{\mathrm{n}} \le 0 \\ F_{\mathrm{n}} \tan\phi_1 & , \quad 0 < F_{\mathrm{n}} \le \varphi_{\mathrm{ncr}} \\ \varphi_{\mathrm{ncr}}(\tan\phi_1 - \tan\phi_2) + F_{\mathrm{n}} \tan\phi_2 & , \quad F_{\mathrm{n}} > \varphi_{\mathrm{ncr}} \end{cases} \tag{5}$$

The proposed failure criterion is implemented in the standard particle flow code. A series of numerical simulations are performed in order to investigate effects of confining pressure, loading path and the intermediate principal stress on deformation, failure process and macroscopic strength of cohesive granular materials.

3 Calibration and validation for the new bond model

The calibration and validation of the proposed new bond model as well as the effect of particle size distribution are presented hereafter in order to introduce the new nonlinear failure criterion to describe the mechanical response of cohesive materials for a large range of confining pressures.

3.1 Calibration of micromechanical parameters

As indicated in the above equations, there are seven micro mechanical parameters need to be identified in the proposed new bond model. The calibration process includes two main tasks: calibrating the elastic and strength parameters. For identifying the elastic, there is an approximating relationship between the Young's modulus E_c and the micromechanical parameters of contact as denoted by the following equation parameters [12, 13, 23]:

$$k_n = 4E_cR, \quad k_s = k_rk_n \tag{6}$$

where R is the average radius between two adjacent particles, k_r is the ratio of normal and shear stiffness, which is related to the Poisson's ratio and generally taken as 1.0–3.0 as done in previous work [7, 15, 35]. The value of k_r is set to be unit for the sake of simplicity. Then, setting the bond strength $\varphi_{nt}\varphi_s$ at a greater value, the calibration of Young's modulus E can be done by adjusting E_c to match the values from laboratory experiments. Afterward, the Poisson's ratio can be also determined by varying k_r. Finally, the elastic parameters k_n, k_s, k_r can be further obtained after an optimal process of adjustments.

In calibration of strength parameters, the normal and shear contact bond strengths φ_{nt}, φ_s have the following relationships with the material strengths σ_c, τ_c for pure axial and pure shear loading [30, 36]:

$$\varphi_{nt} = 4\sigma_cR^2, \quad \varphi_s = 4\tau_cR^2 \tag{7}$$

The commonly used strategy to calibrate the strength parameters φ_{nt} and φ_s is to specify the mean and standard deviations of the material normal strength σ_c as well as the shear ones τ_c according to Eq. (7). However, the ratio of the mean values to standard deviations of material strength can induce different failure models for the same sample. To avoid this uncertainty, the micro-parameters in this work are directly calibrated by the following method. Firstly, the frictional angle ϕ_1 and ϕ_2 was initially set equal as unity to reduce the number of independent parameters. Then, by reducing the normal and shear bond strengths $\varphi_{nt}\varphi_s$, the peak strength between the numerical test and laboratory experiments can be approximately matched. It should be noticed that the aforementioned calibration process of strength is carried out under one confining pressure. Finally, further adjustments for frictional angle ϕ_1, ϕ_2 and the transition threshold φ_{ncr} are needed to account for peak strengths of laboratory experiments under a large range of confining pressure.

3.2 Size effects

According to the above-mentioned calibration process, it can be found from Eq. (6) that the variation of particle average radius R will directly result in change of contact stiffness and further affect the local stress calculation. It has been reported that the size effects can have influence on the macro-mechanical strength of geomaterials in modeling. For example, Mehranpour and Kulatilake [23] have conducted a large number of uniaxial compression tests to study this effect. But for a large range of confining pressure, this effect is still needed to be verified and clarified. A series of triaxial compression tests are carried out in this paper to investigate the size effects by considering (a) constant average particle radius R to investigate the effect of particle numbers or sample size; (b) constant ratio of average particle size sample dimension to investigate the effect of particle size.

The effect of sample size is investigated by setting constant average particle radius R. Two confining pressures such as 5 and 50 MPa are considered. In the simulation, the samples are generated with ten size grades as shown in Fig. 2. The average particle radius R is 8 mm, and the diameters of sample vary from 150 to 550 mm. The micromechanical parameters for the new bond model are taken as E_c= 45 GPa, k_r = 1.0, k_n = 1.5 × 10^9 N/m, k_s = 1.5 × 10^9 N/m, φ_{nt}= 3.5 × 10^4 N, φ_s= 7 × 10^4 N, φ_{ncr}= 1.5 × 10^5 N, $\tan\phi_1$ = 0.3, $\tan\phi_2$ = 1.6, which are calibrated according to the aforementioned procedure. It is shown in Fig. 3 that both the strength and Young's

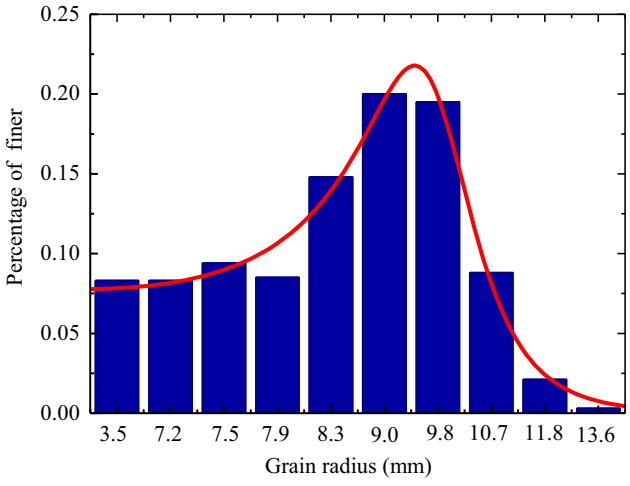

Fig. 2 Particles size distribution used in DEM simulations

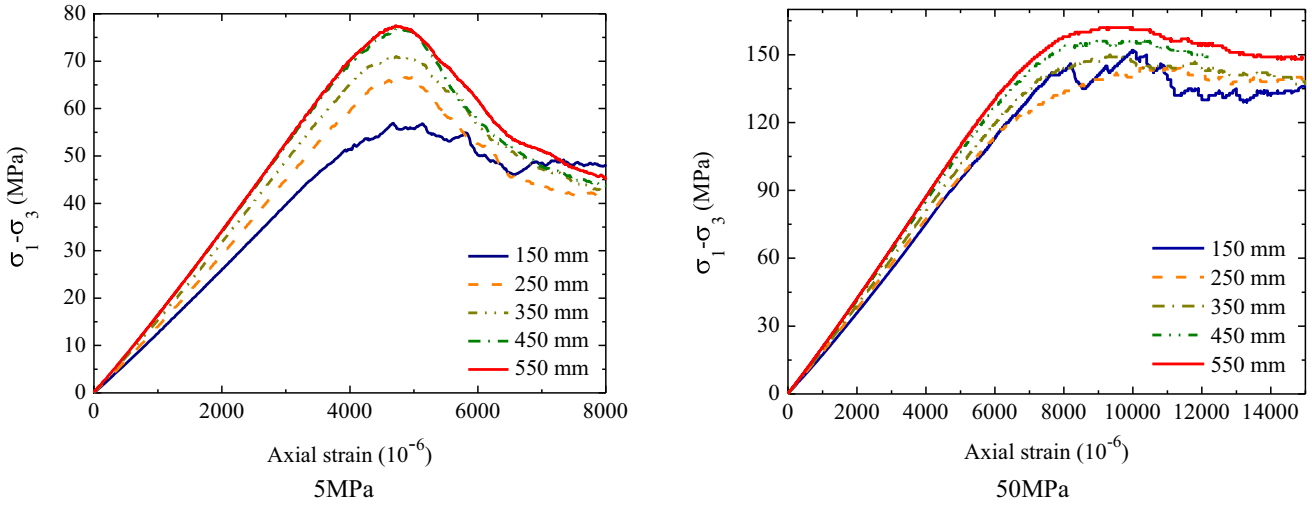

Fig. 3 Stress–strain curves for samples with the particle average radius of 8.0 mm and sample dimensions of 150, 250, 350, 450, and 550

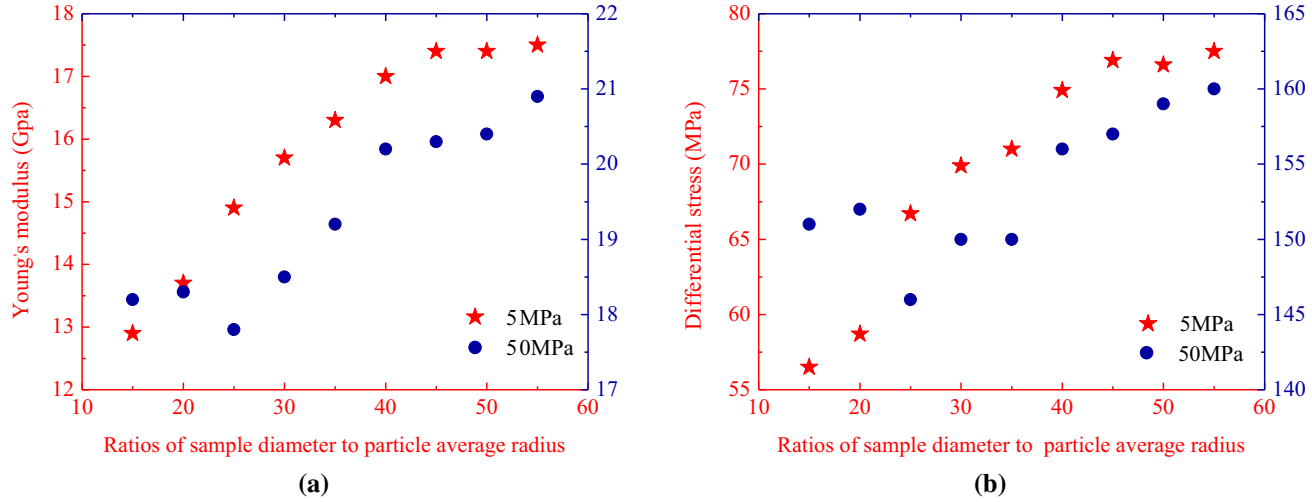

Fig. 4 Effect of ratio of sample diameter to particle average radius on **a** Young's modulus and **b** peak strength of sample under different confining pressures

modulus of the sample seem to increase as the sample dimension increases. However, the increasing trend is negligible when the sample diameter is over 40 times of particle average radius as shown in Fig. 4a, b.

Thus, we further do numerical experiments at the constant ratio 1/50 between the particle radiii to the sample diameters to show the effects of particle size. These micromechanical parameters are calibrated by optimizing values according to the relationships in Eqs. (6) and (7). As shown in Fig. 5, average particle radius versus sample dimension is, respectively, as 1/50, 2/100, 4/200, 8/400 and 16/800. One can note that the Young's moduli are similar for different samples under both confining pressures, whereas peak strength increases a little as increasing sample size. It further indicates in Fig. 6 that the size variations have a very slight effect on Young's modulus as well as strength for samples with the same ratio of diameter to average particle radius, which indicates that size effects can be reduced when sample diameter is 50 times larger than particle radius.

Therefore, size effects exist in the PFC modeling and the particle size is not an independent parameter that affects modeling results. The sample size effects can be reduced or even negligible when the ratio between sample diameter and particle radius is at a given value.

3.3 Comparison between different bond models

In order to investigate and validate the proposed new bond model, a series of triaxial compression tests using different bond models are conducted under confining pressure of 5, 20, 50 and 60 MPa. The friction coefficient is set to 0.3 and

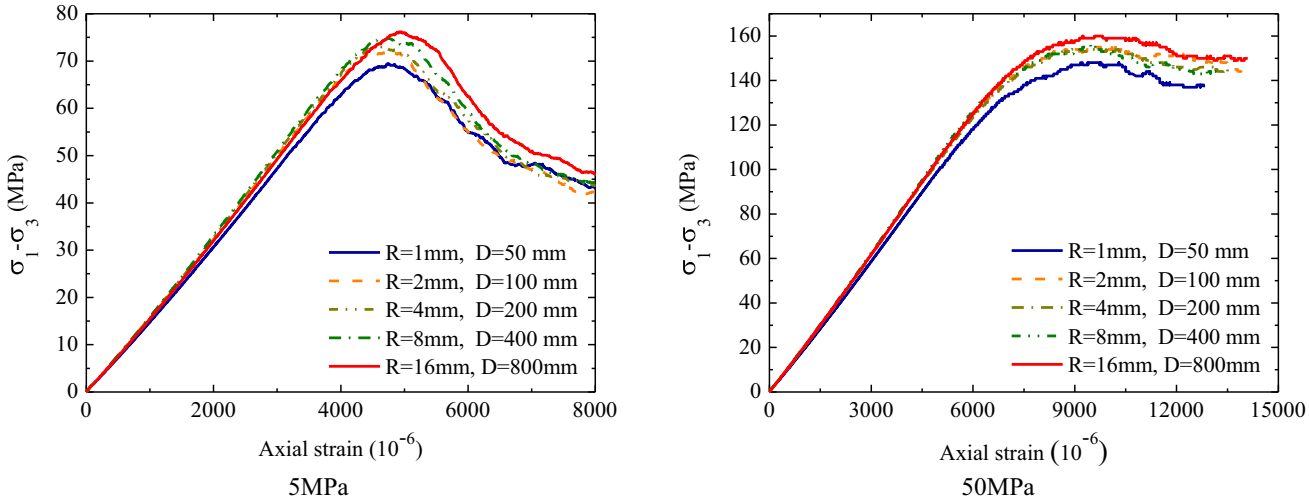

Fig. 5 Stress–strain curves for samples with the particle average radius/sample diameter of 1/50, 2/100, 4/200, 8/400, and 16/800 mm

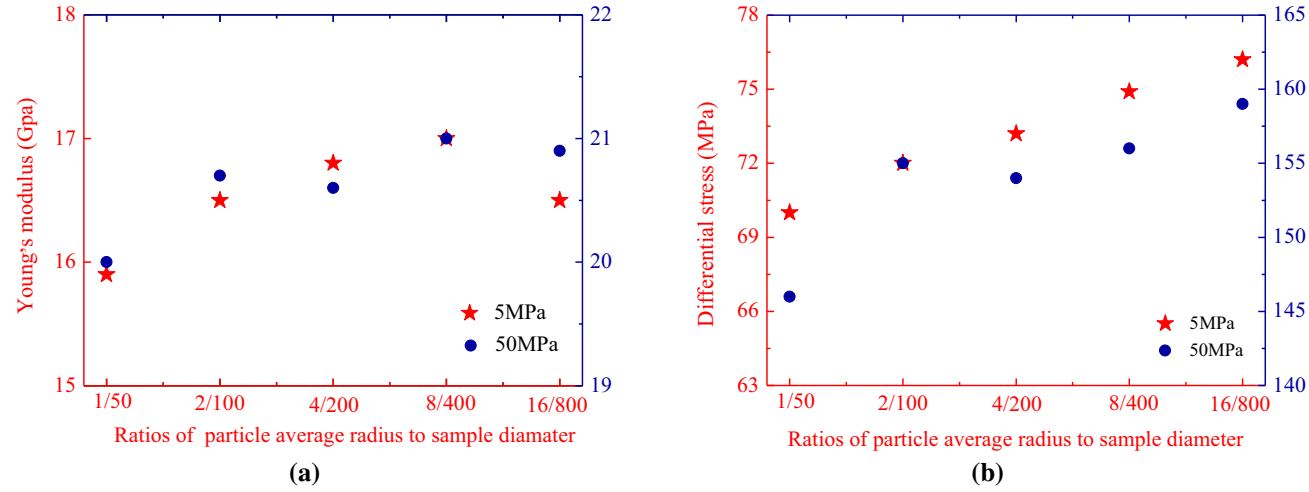

Fig. 6 Effect of both changing sample dimension and particle average radius on **a** Young's modulus and **b** peak strength of modeled sample under different confining pressures

no critical normal stress is included in the PFC incorporated contact bond models. The other micromechanical parameters are taken the same as those in the proposed new bond model.

The results shown in Fig. 7 indicate that the peak stress under low confining pressure with the proposed new bond model is lower than that with the contact bond model (CBM). However, when confining pressure increases up to 60 MPa, this trend becomes different. As shown in Fig. 8, the envelope of peak strength obtained by the proposed new bond model has an obvious nonlinear characteristic, which is different from that obtained using the contact bond model (CBM).

4 Three-dimensional simulation of conventional triaxial compression test

In order to further validate the new bonded model in application of labriation, three-dimensional studies of conventional triaxial compression tests are also performed. Numerical results are compared with experimental data obtained on sandstone.

4.1 Experimental tests

The experimental tests of sandstone were performed in Laboratory of Mechanics of Lille, France. A series of conventional triaxial tests were conducted on cylindrical

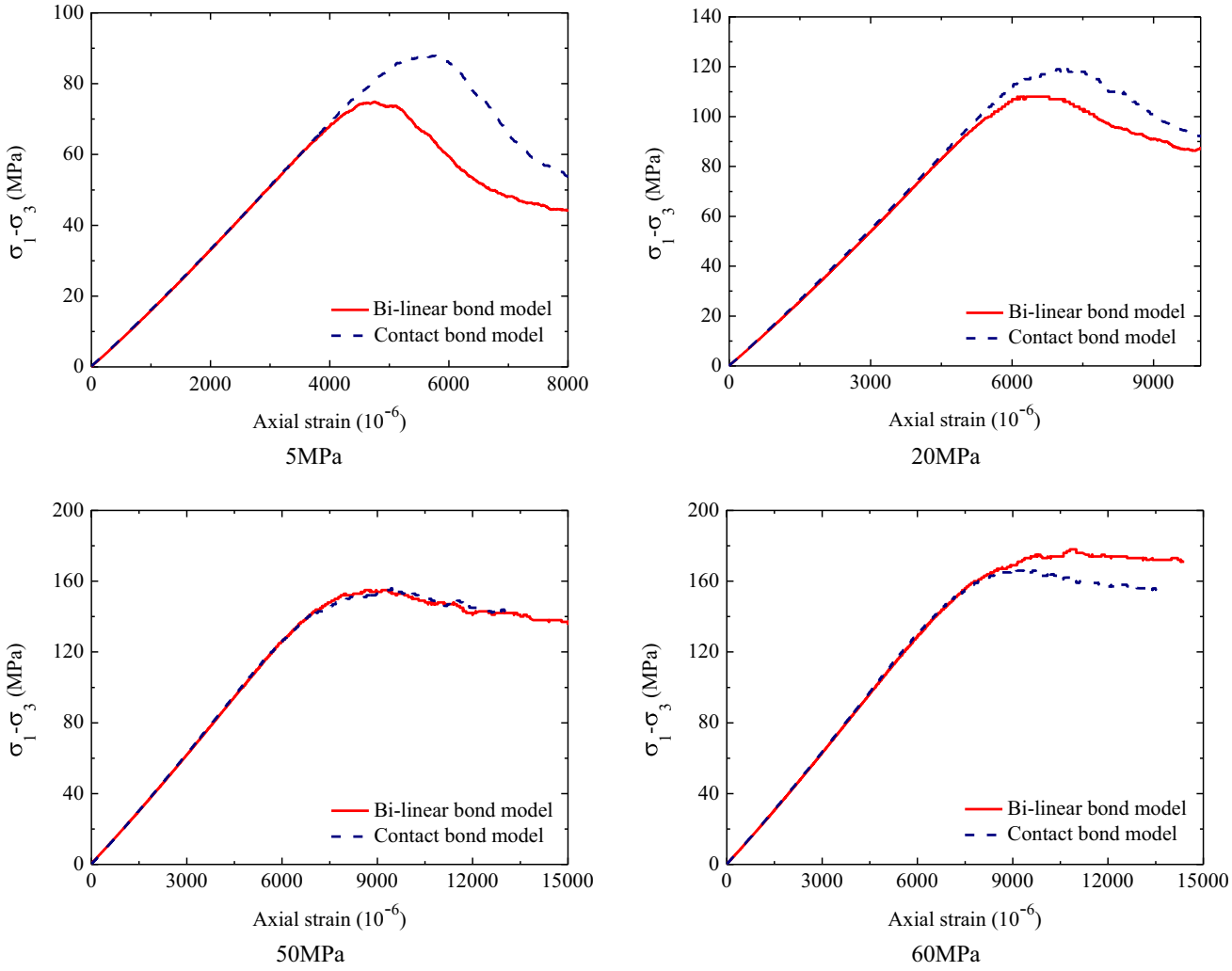

Fig. 7 Different stress–strain curves obtained from results, respectively, simulated using new bond model and contact bond model in PFC3D

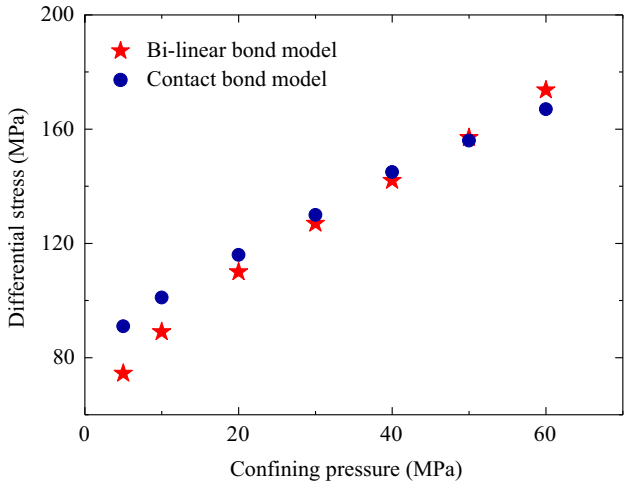

Fig. 8 Comparison between new bond model and contact bond model (CBM) in describing mechanical response of sample with the same micro-parameters

samples of 37 mm in diameter and 75 mm in height under the confining pressures of 5, 20, 40 and 60 MPa. It can be obtained from the results that the Young's modulus of sample increases from 15 to 18 GPa with the confining pressure changing from 5 to 60 MPa, and the envelope of strength presents an obvious nonlinear characteristic as shown in Fig. 9.

4.2 Sample generation and boundary conditions

The real microstructure of cohesive granular materials such as sandstone is complex. It is generally not possible to completely reproduce all details of the microstructure. The real material sample is replaced by a numerical sample which is an assembly of spherical grains of different diameter. In the present study, the numerical sample is constituted about 20,000 particles with ten different size grades, as shows in Figs. 2 and 10. The largest radius of particle is 13.6 mm, and the smallest one is 3.5 mm. The

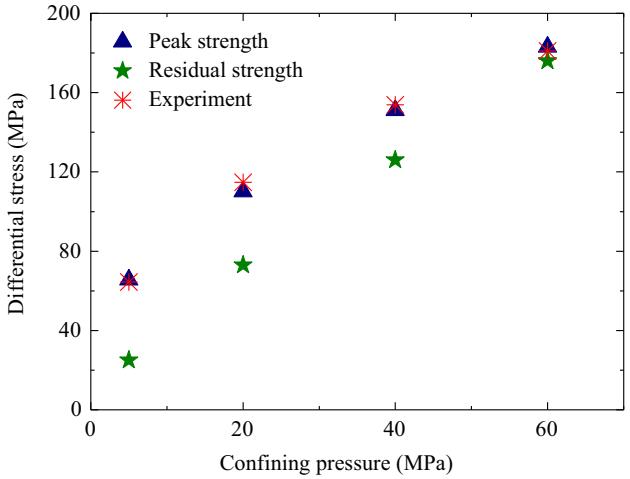

Fig. 9 Macroscopic peak and residual strength obtained in conventional triaxial compression tests and comparison with experimental data on sandstone

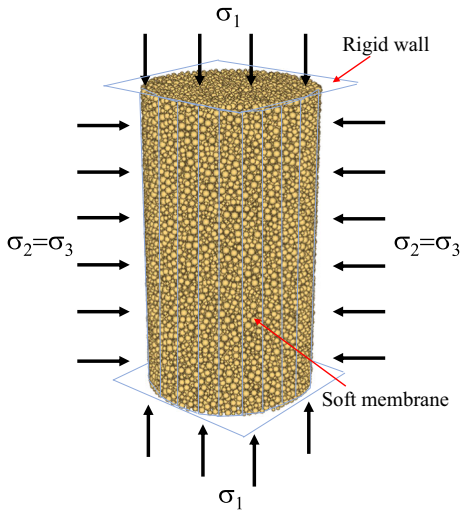

Fig. 10 Sample used in DEM modeling of triaxial compression tests

numerical sample is a cylinder of 370 mm wide and 740 mm high. The total porosity is about 0.2. The ratio of sample diameter to particle average radius is about 50.

Differently with a continuum medium, the numerical specimen of granular material is composed of spherical grains. Therefore, it is not possible to directly apply a uniform stress or displacement on its boundary. In general, in order to prescribe a uniform displacement on boundary of specimen, a rigid wall is added on the top and bottom surfaces, while a soft membrane is used on the lateral surface to confine the specimen. In this way, the macroscopic axial and lateral stresses are calculated as the average reaction forces generated on the top and lateral surfaces. The axial and lateral displacements are applied in an iterative way so that the equilibrium conditions are verified with the applied confining pressure or lateral stress. Further, the axial displacement is applied symmetrically on the top and bottom walls.

4.3 Stress–strain responses and comparison with experiment

By adopting a numerical optimal procedure aforementioned, a set of model's parameters is defined and given in Table 1. Using these parameters for the proposed bonded contact model, four conventional triaxial compression tests are calculated with different confining pressures such as 5, 20, 40 and 60 MPa. Comparisons between numerical results and experimental data are presented in Fig. 11. An overall good agreement is obtained. It is seen that with the increase in confining pressure, the peak differential stress significantly increases. This effect of confining pressure is correctly reproduced by the numerical model. Unfortunately, due to the technical limit of experimental device, the mechanical responses in the post-peak regime are not available in the laboratory tests. However, according to the numerical results obtained, one can see a clear transition from a brittle behavior under a low confining pressure to a ductile one when the confining pressure becomes higher. This kind of transition is a representative property of most rock-like materials. On the other hand, the volumetric strain exhibits a transition from compressibility and dilatancy with the increase in differential stress. The occurrence threshold of the transition also depends on confining pressure. Under a low confining pressure such as 5 MPa, the compressibility–dilatancy transition occurs clearly before the peak stress. When the confining pressure is high enough, the volumetric dilatancy occurs only when the peak stress is approached. Physically, the volumetric

Table 1 Geometrical, physical and mechanical parameters used in three-dimensional DEM simulations of experimental tests

3D Sample	
Width of sample (mm)	370
Height of sample (mm)	740
Total grain number in sample	20,000
Radius (mm)	See Fig. 2
Initial void ratio	0.2
Mechanical parameters for new bond model	
Normal contact stiffness for test k_n (N/m)	1.516×10^9
Shear contact stiffness for test k_s (N/m)	1.516×10^9
Inter-particle coefficient of friction $\tan\phi_1$	0.27
Inter-particle coefficient of friction $\tan\phi_2$	1.7
Normal bond strength φ_{nt} (N)	0.32×10^5
Shear bond strength φ_s (N)	0.9×10^5
The critical normal stress φ_{ncr} (N)	2.1×10^5

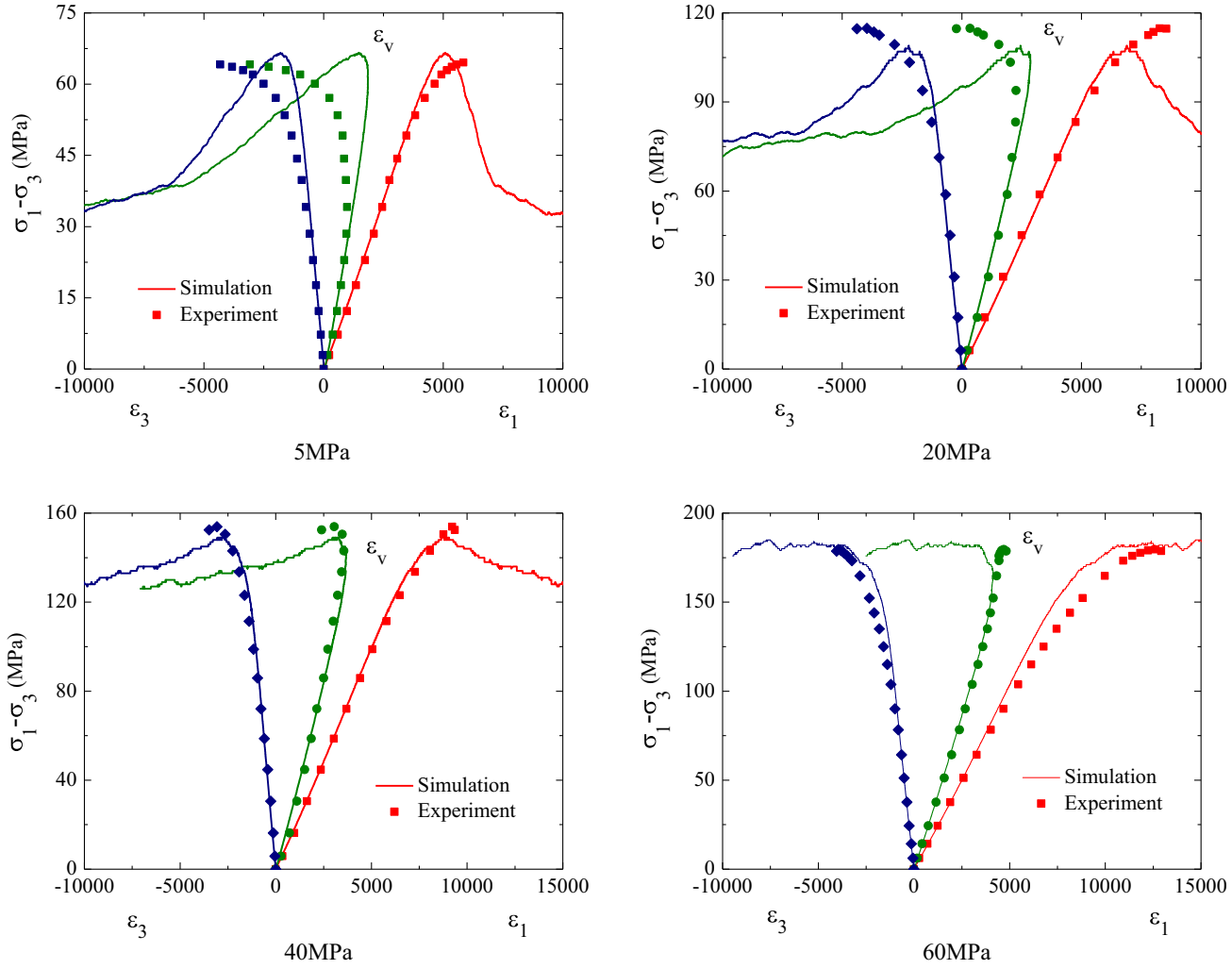

Fig. 11 Axial (red), volume (green) and lateral (blue) strains (10^{-6}) versus differential stress in conventional compression tests with different confining pressures: comparison between numerical results (continuous lines) experiment data

dilatancy in rock-like materials is generally the macroscopic consequence of deboned interfaces opening. The opening can be generated by both tensile failure and frictional sliding of contact interfaces in granular materials. When the confining pressure is low, a large number of broken contact interfaces in granular materials produce a normal opening contributing to the macroscopic dilatancy. Under a high confining pressure, most broken contact interfaces are closed and their normal opening is prevented by a high normal compressive stress. In this case, the dilatancy occurs only when there is the occurrence of localized shear strain bands around the peak stress. In the post-peak regime, the macroscopic response is mainly controlled by the deformation of localized strain bands. As most contact interfaces are broken inside the localization bands, an important volumetric dilatancy can be produced due to large relative displacements between grains.

4.4 Macroscopic strength analysis

In order to have a deep insight into the macroscopic strength of material, the macroscopic peak and residual differential stresses obtained from numerical simulations are shown in Fig. 9. The peak strength is further compared with experimental data, and a good agreement is obtained. From this figure, one can see that the peak strength envelope cannot be approached by a linear line, but it should be described a curved convex line. This nonlinear strength property is correctly reproduced by the proposed model. Further, it is interesting to observe that the distance between the peak and residual strengths decreases when the confining pressure increases. This is a direct consequence of the transition from brittle to ductile behavior with the increase in confining pressure.

5 Failure process in cohesive granular materials

The deformation and failure process of cohesive granular materials is inherently related to the breakage of bonded contact interfaces between grains. Using the proposed failure criterion, the macroscopic failure process of material is here investigated in terms of microscopic debonding.

5.1 Bond breakage analysis

At the initial state before applying differential stress, there are about 66,000 bonded inter-granular interfaces in the numerical specimen. With the increase in differential stress, bonds are progressively broken according to the proposed local failure criterion. For convenience, each broken bond is here seen as a crack. One can distinguish two families of cracks, tensile and shear cracks. The evolution of crack number can be calculated by the numerical model during the differential loading. In Fig. 12, one can see the evolution of tensile and shear cracks as a function of axial strain in four conventional triaxial compression tests with different confining pressures. The differential stress is also plotted on the same figure. In order to quantify the contact debonding process, the following bond breakage rate is defined:

$$V_{\mathrm{n}} = \frac{(\mathrm{CN}_{\varepsilon+\Delta\varepsilon} - \mathrm{CN}_{\varepsilon})}{\mathrm{CN}_{*\varepsilon}} \tag{8}$$

$\mathrm{CN}_{\varepsilon}$ and $\mathrm{CN}_{\varepsilon+\Delta\varepsilon}$ are, respectively, the broken contact numbers at the strain states ε and $\varepsilon + \Delta\varepsilon$; $\mathrm{CN}_{*\varepsilon}$ represents the total number of broken contacts in the specified strain interval $*\varepsilon$. The evolutions of debonding rate in four triaxial compression tests are presented in figure. One can see that for all confining pressures considered here, the debonding process starts before the peak strength is reached (see the points A1, B1, C1 and D1). However, only a very small number of cracks are developed in the pre-peak stage. The number of cracks increases very quickly when the peak strength is approached, and the highest

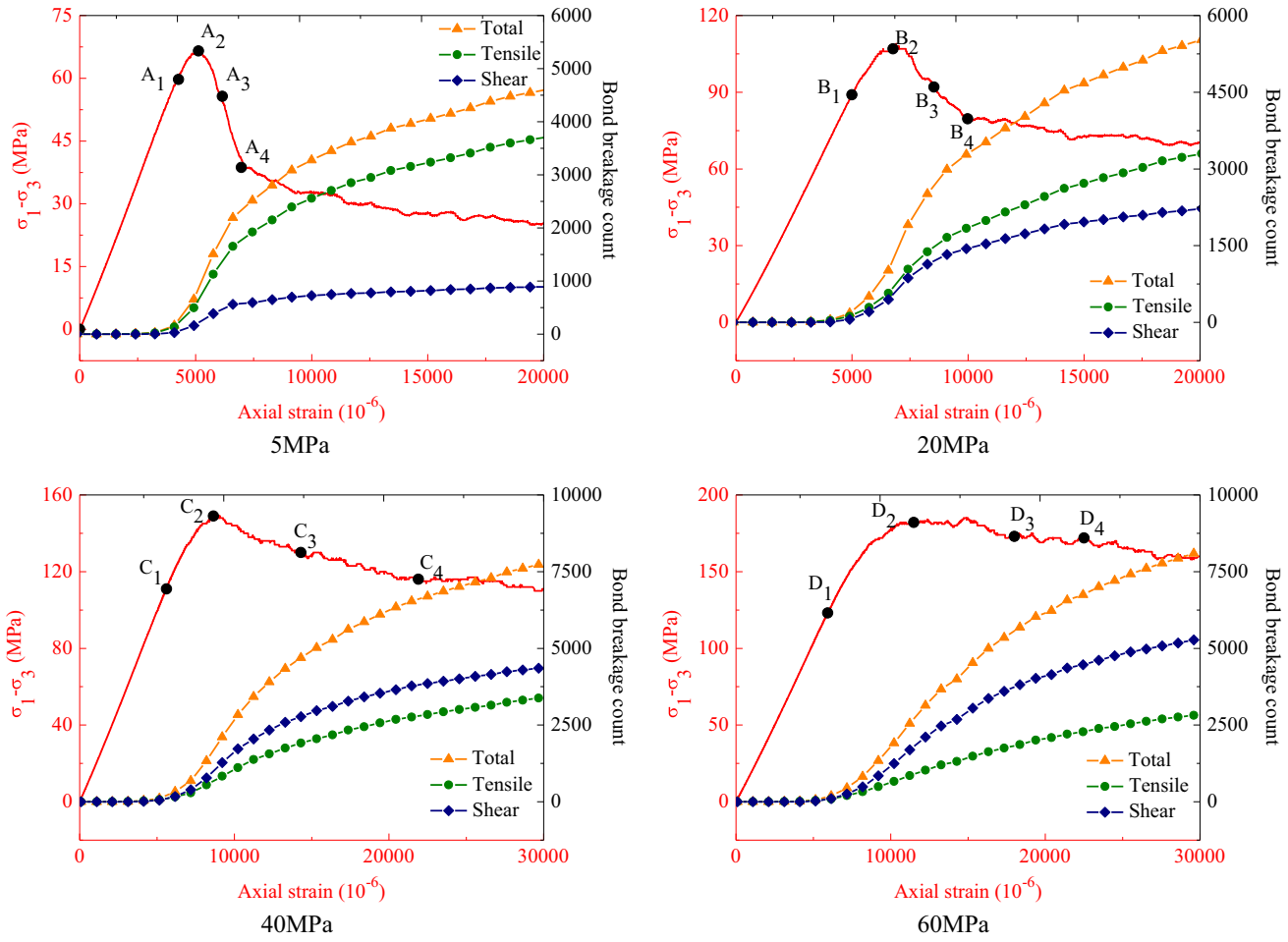

Fig. 12 Evolution of bonds breakage number versus axial strain and differential stress in conventional triaxial compression tests with different confining pressures

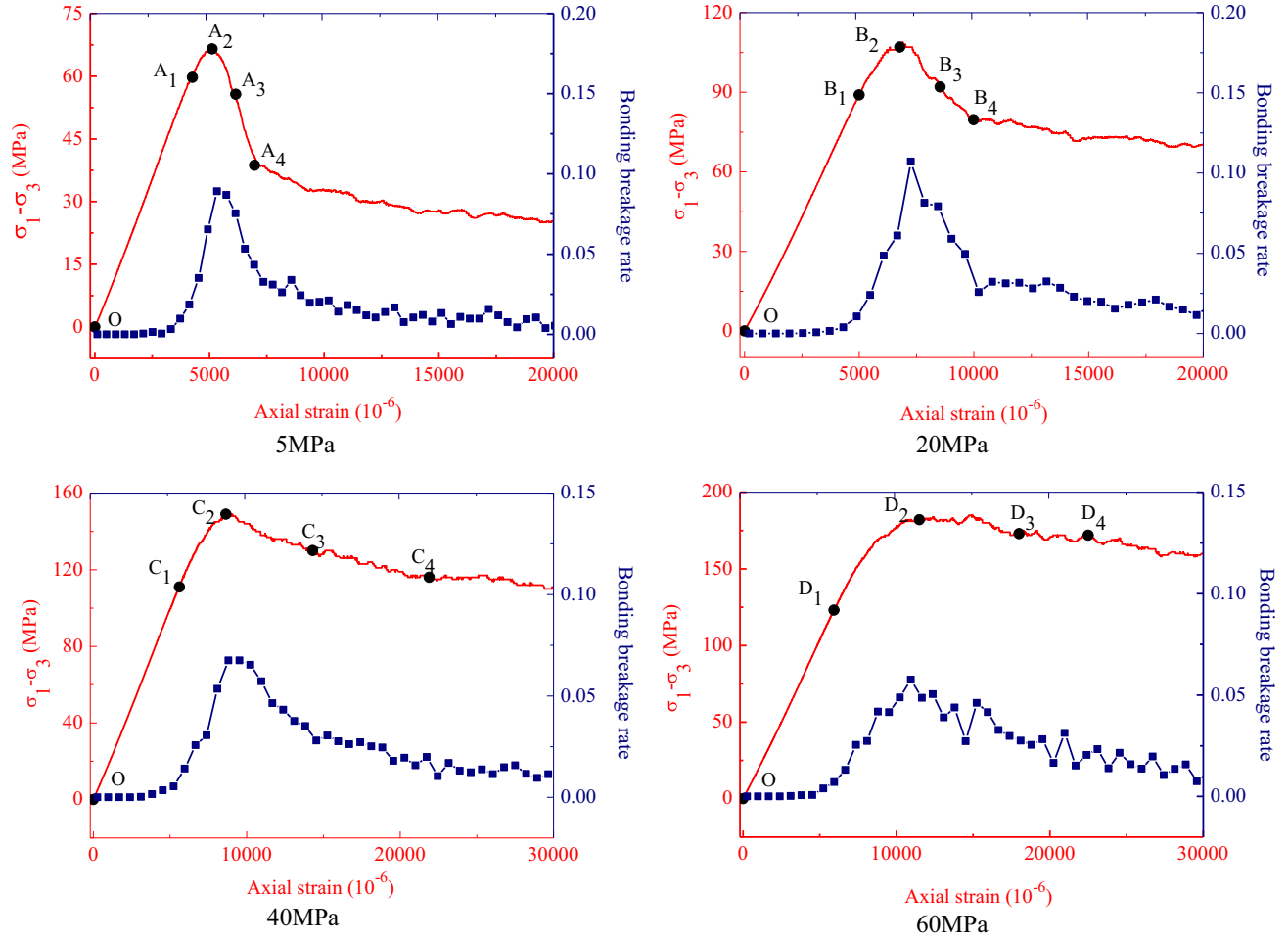

Fig. 13 Evolution rate of bond breakage number versus axial strain and differential stress in conventional triaxial compression tests with different confining pressures

debonding rate is obtained at the peak stress point (A2, B2, C2 and D2). The evolution of breakage rate in the post-peak regime is strongly influenced by confining pressure. The curve of breakage rate is clearly correlated to that of differential stress. Under low confining pressures (5 and 20 MPa), the breakage rate drops quickly after the peak stress (see the points A3 and B3) and evolves toward a stationary value when the residual strength is reached (see the points A4 and B4). Differently, under high confining pressures (40 and 60 MPa), the breakage rate decreases slowly but continuously in the post-peak regime. It is not easy to identify a clear residual phase (see the points C4 and D4). On the other hand, it is also very interesting to see that the cracking mode is also influenced by confining pressure. Under low confining pressures (5 and 20 MPa), the number of tensile cracks is clearly higher than that of shear cracks. This is the main reason of the macroscopic brittle failure obtained under a low confining pressure and of the important dilatancy obtained. When the confining pressure becomes high (40 and 60 MPa), the number of shear cracks becomes higher than that of tensile cracks. As a consequence, one obtains a ductile macroscopic failure behavior which is dominated by the frictional sliding along broken bonds (Fig. 13).

Furthermore, in Fig. 14, one shows the distributions of displacement inside the three-dimensional specimen and in the normal section during a selected strain interval in the post-peak regime (A3–A4, B3–B4, C3–C4 and D3–D4) for four triaxial compression tests. It can be observed that the displacement distribution is also affected by confining pressure. Under low confining pressures, an inclined narrow band is obtained with an important displacement gradient on the boundary between this band and outside zones. This is in agreement with the brittle failure process of specimen. With the increase in confining pressure, the inclination angle with the axial load axis as well as the width of band increases. And finally one obtains a large and quasi-horizontal zone in the central part of specimen. This kind of displacement distribution corresponds to a ductile macroscopic failure behavior.

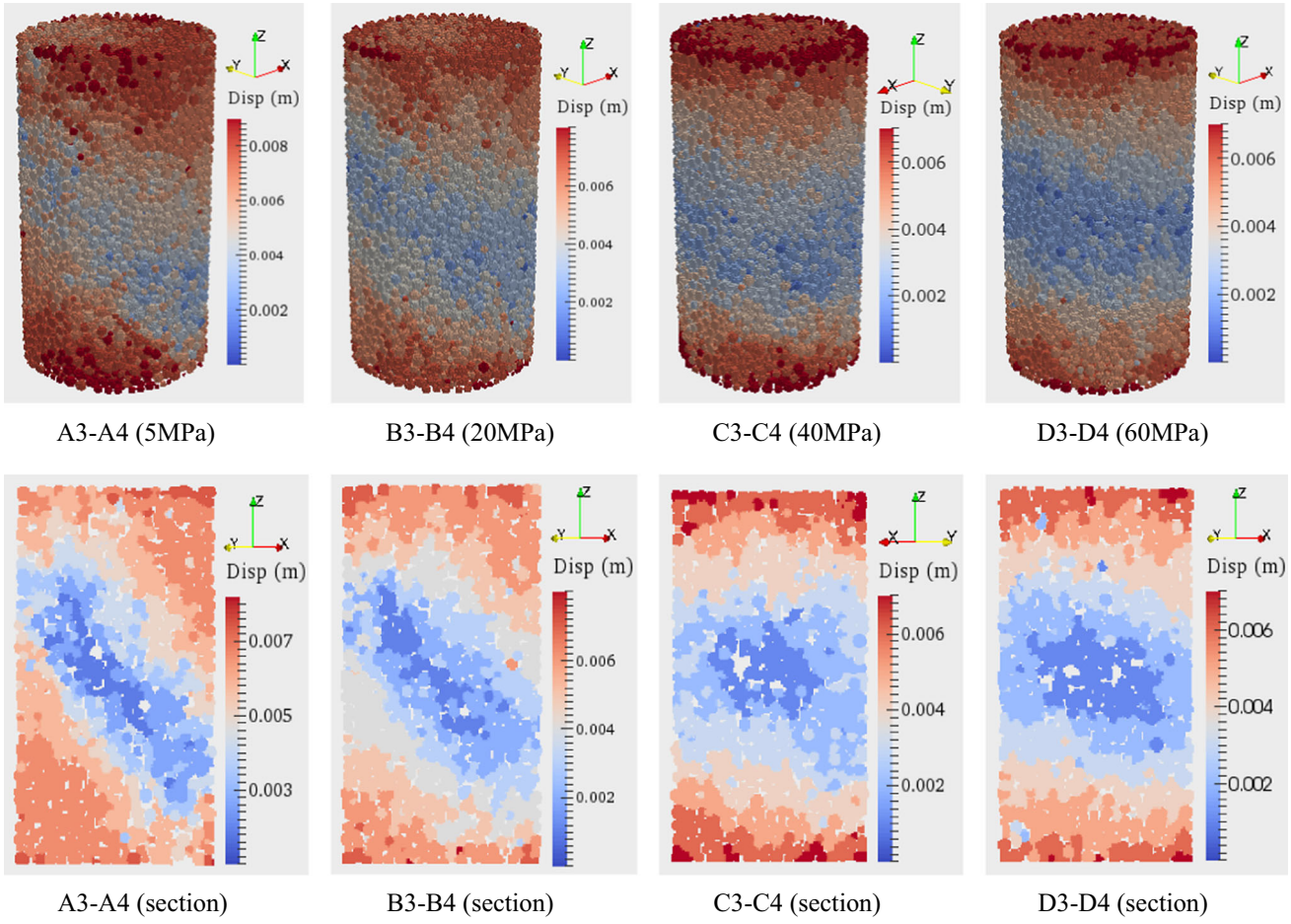

Fig. 14 Illustration of displacement fields inside 3D whole specimen and in central section in conventional triaxial compression tests with different confining pressures

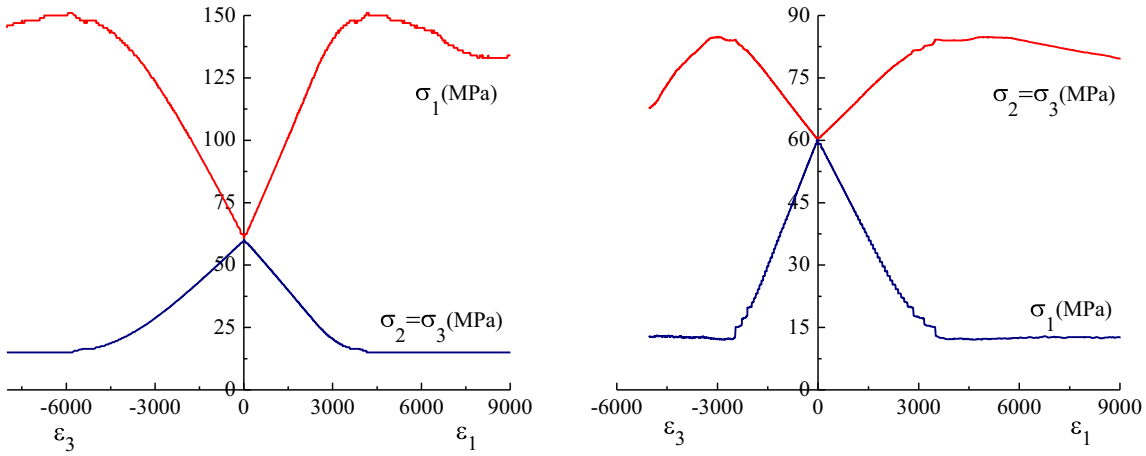

Fig. 15 Stress–strain curves in lateral extension test (left) and axial extension test (right) with an initial hydrostatic stress of 60 MPa

5.2 Effect of loading path

The deformation and failure process is generally related to loading path. In the context of mechanics of geomaterials, two typical loading paths are particularly interesting to investigate because they could represent stress evolutions around an underground cavity. It is the lateral extension and the axial extension with a constant mean stress. In the

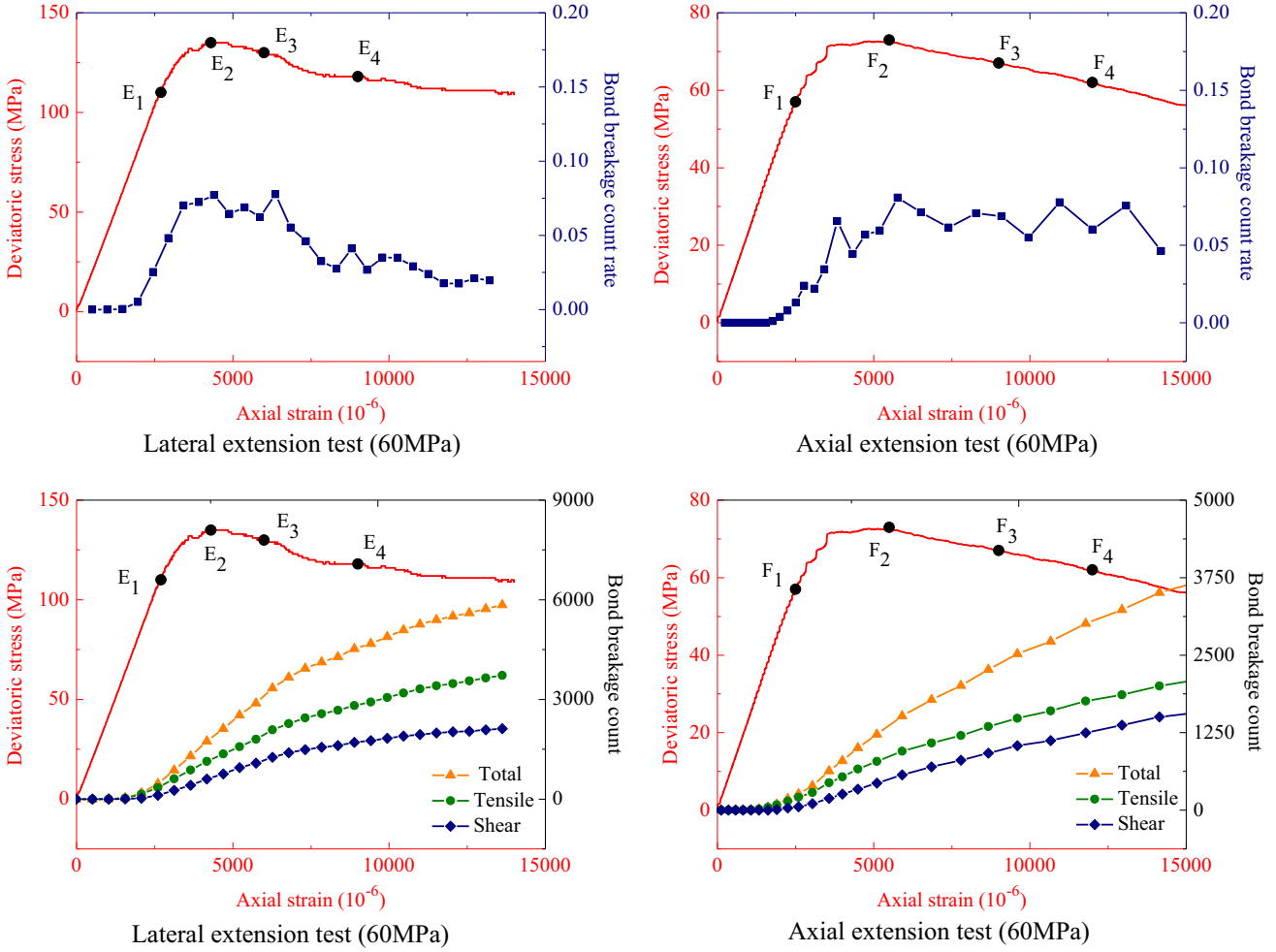

Fig. 16 Evolutions of bond breakage number and rate in lateral extension test (left) and axial extension test (right) with an initial hydrostatic stress of 60 MPa

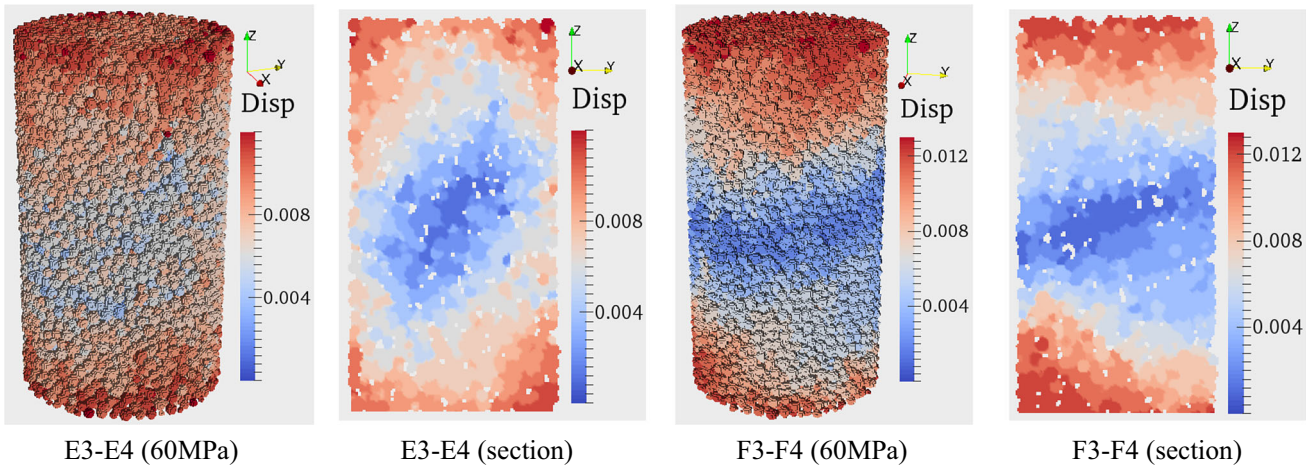

Fig. 17 Displacement fields in lateral extension test (two left figures) and axial extension test (two right figures) with an initial hydrostatic stress of 60 MPa

first path, starting from a hydrostatic compression stress state, the lateral stress or confining pressure (here noted as $\sigma_2 = \sigma_3$) is reduced ($\Delta\sigma_2 = \Delta\sigma_3 < 0$), while the axial stress (noted as σ_1) is increased ($\Delta\sigma_1 > 0$) so that the mean stress

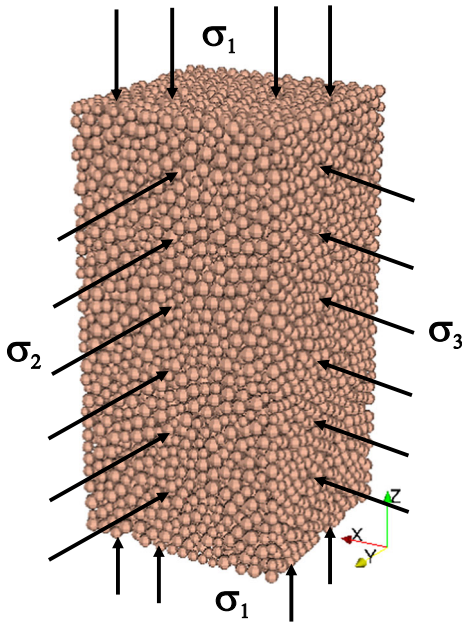

Fig. 18 Cubic sample subjected to three independent principal stresses

is unchanged ($2\Delta\sigma_2 + \Delta\sigma_1 = 0$). In the case of axial extension, also starting from a hydrostatic compression stress state, the lateral stress or confining pressure (here noted as $\sigma_2 = \sigma_3$) is increased ($\Delta\sigma_2 = \Delta\sigma_3 > 0$), while the axial stress (noted as σ_1) is decreased ($\Delta\sigma_1 < 0$) so that the mean stress is unchanged ($2\Delta\sigma_2 + \Delta\sigma_1 = 0$). The values of Lode angle for these two loading paths are, respectively, equal to $\theta = \pi/6$ and $\theta = -\pi/6$. Therefore, the comparison between these two paths allows investigating the influence of Lode angle or the third stress invariant on deformation and failure process of materials. In the present study, as an example, the initial hydrostatic stress is taken as 60 MPa.

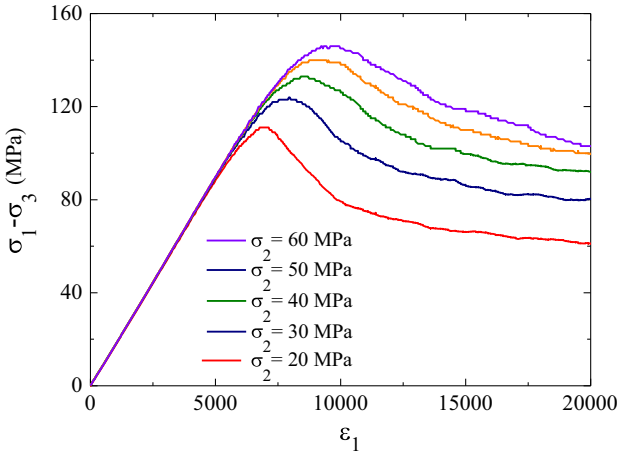

Fig. 20 Influence of the intermediate stress on stress–strain curves of cubic specimen with 20 MPa of minor stress (strain in 10^{-6})

The obtained stress–strain curves are presented in Fig. 15. It is shown that the peak differential stress ($|\sigma_1 - \sigma_3|$) for the lateral extension is significantly higher than that for the axial extension. The evolution of bonds breakage for the two loading paths is presented in Fig. 16. One can see that the breakage rate is quite different between the two paths. For the lateral extension, the highest rate is obtained around the peak differential stress, and the bond breakage rate decreases in the post-peak regime. However, for the axial extension, it seems that there is a quasi-stationary rate of debonding after the peak differential stress. Finally, in Fig. 17, the fields of displacement inside the specimen and in the normal section are presented. For the lateral extension, one observes an inclined localization band similarly to that in conventional triaxial compression. But for the axial extension, there is a quasi-horizontal localization band which covers all the width of specimen.

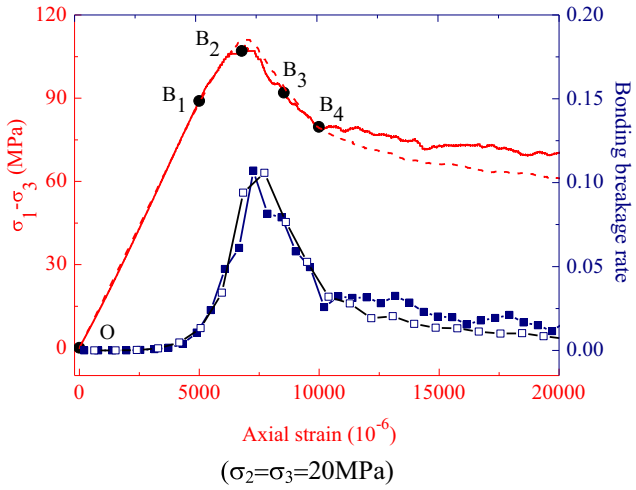

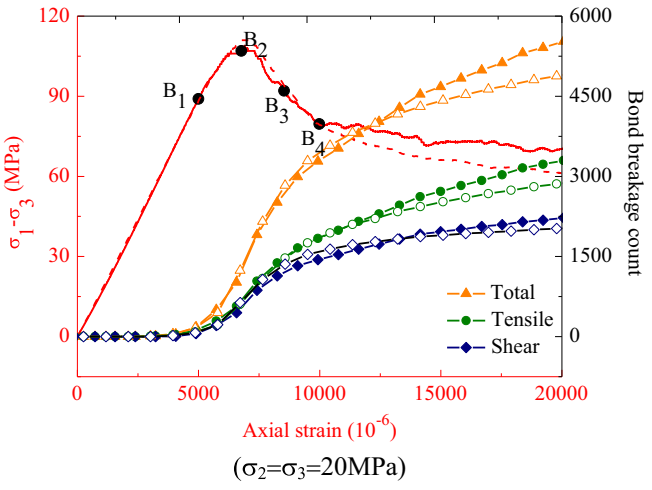

Fig. 19 Evolutions of bonding breakage rate and accumulated number together with stress–strain curves in a triaxial compression test, respectively, on cubic sample (continuous lines) and cylinder sample (dotted lines)

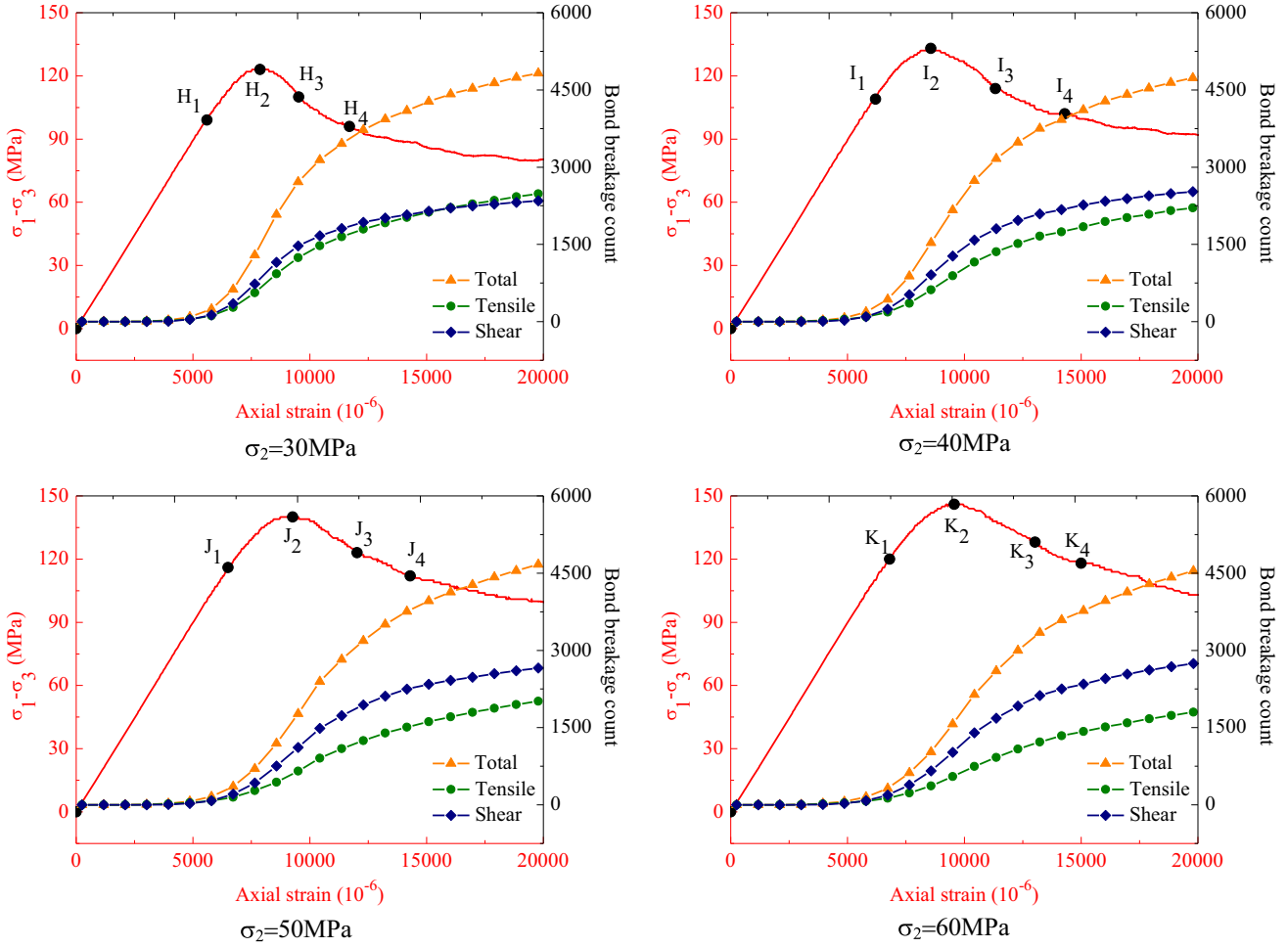

Fig. 21 Evolutions of accumulated bonds breakage number for different values of intermediate principal stress (σ_3 = 20 MPa)

5.3 Effect of intermediate principal stress

In cylinder samples considered above, two principal stresses are identical ($\sigma_2 = \sigma_3$). Based on this kind of experimental data, most failure criteria developed for geomaterials involve the major and minor principal stresses only. The role of the intermediate principal stress is generally neglected. However, in general loading conditions, three principal stresses are different and independent. Therefore, it is needed to investigate the effect of the intermediate principal stress on failure and deformation of cohesive granular materials. For this purpose, a cubic sample is considered and shown in Fig. 18. Two lateral walls are used to independently prescribe two different principal stresses. The same parameters as those given in Table 1 are used. We have performed a series of numerical tests on the cubic sample. The minor principal stress is kept to be constant and equal to 20 MPa. Different values of the intermediate principal stress ranging from 20 to 60 MPa are considered. For a selected set of two principal stresses, the axial strain is prescribed in order to generate the variation of axial stress which is the major principal stress. In Fig. 19, one compares first the numerical results obtained from both the cylinder and cubic samples when two lateral stresses are identical and equal to 20 MPa. In this particular case, the overall stresses are identical for two samples. One can see that the difference between two calculations is very small. Therefore, the effect of sample geometrical form seems to be negligible. In Fig. 20, the differential stress ($\sigma_1 - \sigma_3$) versus axial strain (ε_1) curves are presented for five different values of the intermediate principal stress (σ_2). One can see that the peak strength of granular material is significantly affected by the intermediate principal stress. The peak stress increases with the intermediate stress increase. In order to further explore the failure process in each case, the evolutions of tensile and shear cracks with axial strain are presented in Fig. 21 for each value of the intermediate stress. While the total number of cracks

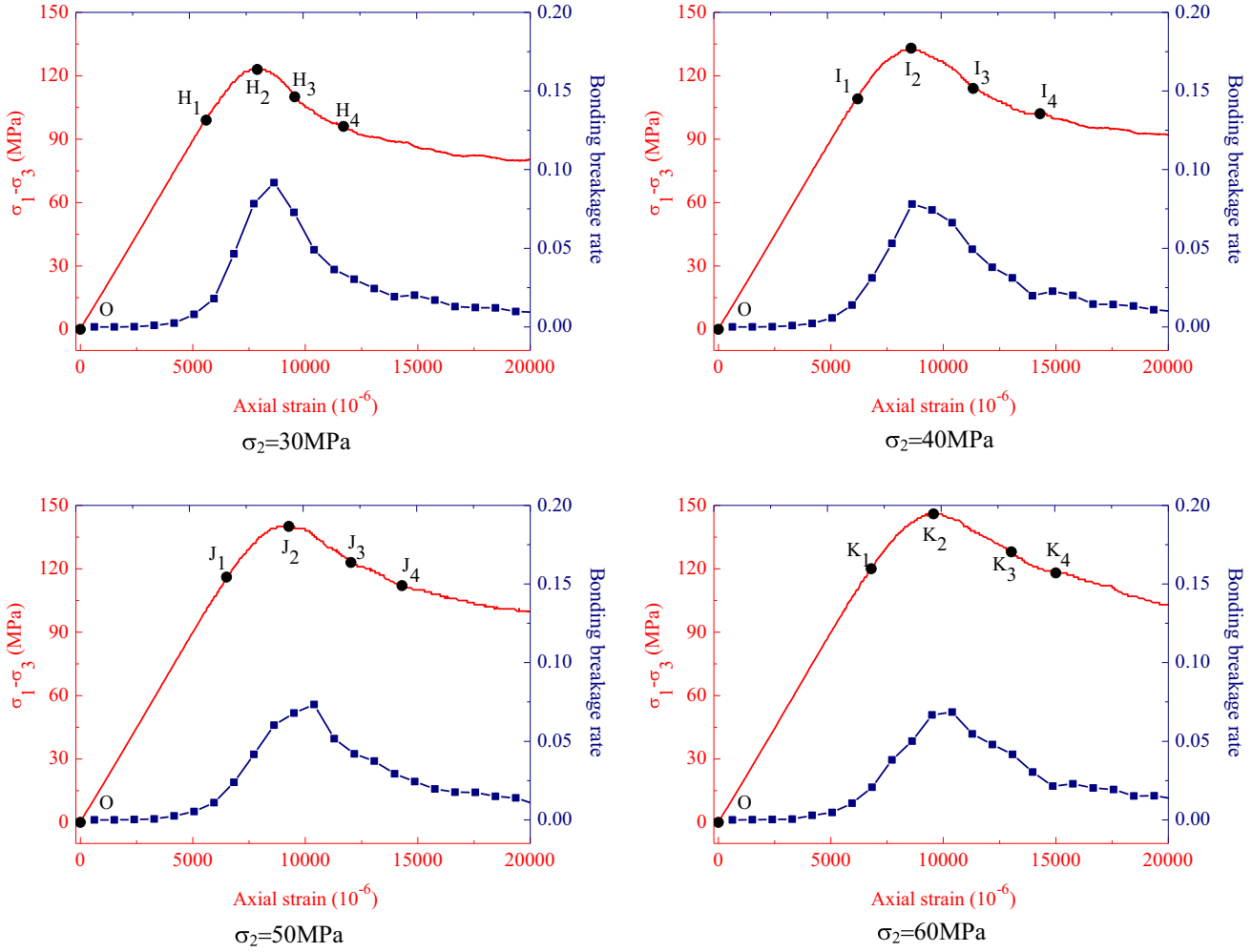

Fig. 22 Evolutions of differential stress and bond breakage rate for different values of intermediate principal stress (σ_3 = 20 MPa)

remains similar between five cases, the repartition between tensile and shear cracks is clearly different. With the increase in the intermediate principal stress, the shear cracking becomes the dominant process with respect to the tensile cracking. Regarding the rate of total bonds breakage shown in Fig. 22, it seems that the sharp change of breakage rate is attenuated with the increase in the intermediate principal stress. Finally, one shows the three-dimensional and two-dimensional displacement fields, respectively, inside the whole specimen and in the normal section in Fig. 23 for a strain interval in the post-peak regime. The kinetics of deformation is clearly affected by the intermediate principal stress. When the difference between two lateral stresses ($\sigma_2 - \sigma_3$) is high, the kinetics of deformation of cubic sample is progressively controlled by the sliding along an inclined direction with respect to the vertical axis (σ_1). The sliding occurs on the boundary of a parallelepiped zone in the plane $z - x$. In contrary, for a law difference of $\sigma_2 - \sigma_3$, the deformation kinetics is rather dominated by lateral expansion of sample.

6 Conclusions

Mechanical strength and deformation of cohesive granular materials have been investigated in this paper. A new criterion for failure modeling of bonded contact interfaces between grains is proposed. Using this criterion, it is possible to describe strength and deformation of granular materials for a wide range of stresses. It is found that the overall strength of cohesive granular materials cannot be described by a linear surface but by a convex curved surface. Further, under the conventional compression condition, the tensile cracking is controlling the failure process under low confining pressure, while the shearing cracking becomes the dominating process when the confining

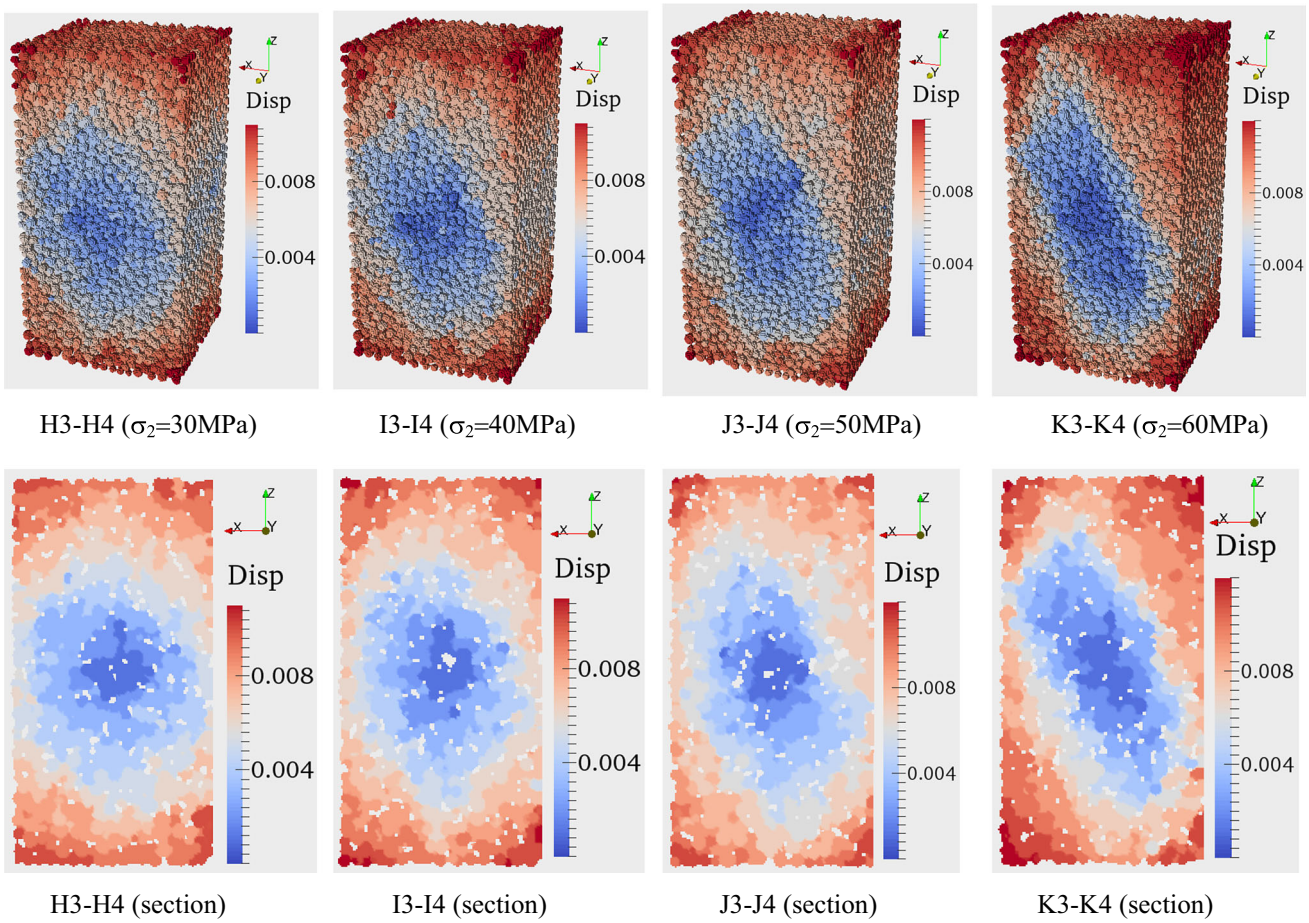

Fig. 23 Distribution of displacement inside whole cubic samples and in normal sections for different values of intermediate principal stress (σ_3 = 20 MPa)

pressure is high. There is a clear transition from a brittle to ductile behavior with the increase in confining pressure. This transition has been correctly predicted by the numerical model. The volumetric dilatancy of cohesive granular materials is directly related to opening of debonded contact interfaces. The strength and deformation of cohesive granular materials are influenced by loading path. For a given mean stress, the strength is lower in an extension loading than in a compressive one. Therefore, the influence of the third stress invariant or Lode angle should be taken into account. Finally, the influence of the intermediate principal stress on the strength and deformation has been studied. It is found that the compressive strength of cohesive granular materials significantly increases with the increase in the intermediate principal stress. Further, the shear cracking is the main failure process under high values of the intermediate stress. The kinetics of deformation and failure is also affected by the intermediate principal stress. The material failure is controlled by the lateral expansion for low values of the intermediate stress but by the sliding process for high ones. Interstitial fluid should play an important role in strength and deformation of cohesive granular materials, and this feature will be investigated in future studies.

Acknowledgements The work is jointly supported by the lxNational Basic Research Program of China (973 Program) (Grant 2015CB057903) and the National Natural Science Foundation of China (Grant 51309089).

References

1. Borja RI, Song X, Rechenmacher AL, Abedi S, Wu W (2013) Shear band in sand with spatially varying density. J Mech Phys Solids 61:219–234
2. Chen Y, Munkholm LJ, Nyord T (2013) A discrete element model for soil–sweep interaction in three different soils. Soil Tillage Res 126:34–41
3. Cheung LYG, O'Sullivan C, Coop MR (2013) Discrete element method simulations of analogue reservoir sandstones. Int J Rock Mech Min Sci 63:93–103. https://doi.org/10.1016/j.ijrmms.2013.07.002
4. Cundall PA, Strack OD (1979) A discrete numerical model for granular assemblies. Geotechnique 29:47–65

5. Das A, Tengattini A, Nguyen GD, Viggiani G, Hall SA, Einav I (2014) A thermomechanical constitutive model for cemented granular materials with quantifiable internal variables. Part II—validation and localization analysis. J Mech Phys Solids 70:382–405
6. Debecker B, Vervoort A (2013) Two-dimensional discrete element simulations of the fracture behaviour of slate. Int J Rock Mech Min Sci 61:161–170. https://doi.org/10.1016/j.ijrmms.2013.02.004
7. Ding X, Zhang L (2014) A new contact model to improve the simulated ratio of unconfined compressive strength to tensile strength in bonded particle models. Int J Rock Mech Min Sci 69:111–119
8. Duan K, Kwok CY (2015) Discrete element modeling of anisotropic rock under Brazilian test conditions. Int J Rock Mech Min Sci 78:46–56. https://doi.org/10.1016/j.ijrmms.2015.04.023
9. Duriez J, Eghbalian M, Wan R, Darve F (2017) The micromechanical nature of stresses in triphasic granular media with interfaces. J Mech Phys Solids 99:495–511
10. Gehle C, Kutter HK (2003) Breakage and shear behaviour of intermittent rock joints. Int J Rock Mech Min Sci 40:687–700. https://doi.org/10.1016/S1365-1609(03)00060-1
11. He P-F, Kulatilake PH, Yang X-X, Liu D-Q, He M-C (2017) Detailed comparison of nine intact rock failure criteria using polyaxial intact coal strength data obtained through PFC3D simulations. Acta Geotechn. https://doi.org/10.1007/s11440-017-0566-9
12. Itasca C (1999) PFC 3D-User manual Itasca Consulting Group, Minneapolis
13. Itasca C (2008) PFC 3D Manual, Version 4.0. Itasca Consulting Group, Minneapolis
14. Jiang M, Yu HS, Leroueil S (2007) A simple and efficient approach to capturing bonding effect in naturally microstructured sands by discrete element method. Int J Numer Methods Eng 69:1158–1193
15. Jiang M, Yan H, Zhu H, Utili S (2011) Modeling shear behavior and strain localization in cemented sands by two-dimensional distinct element method analyses. Comput Geotechn 38:14–29
16. Kruyt N, Rothenburg L (2016) A micromechanical study of dilatancy of granular materials. J Mech Phys Solids 95:411–427
17. Kulatilake P, Malama B, Wang J (2001) Physical and particle flow modeling of jointed rock block behavior under uniaxial loading. Int J Rock Mech Min Sci 38:641–657
18. La Ragione L (2016) The incremental response of a stressed, anisotropic granular material: loading and unloading. J Mech Phys Solids 95:147–168
19. La Ragione L, Prantil V, Jenkins J (2015) A micromechanical prediction of localization in a granular material. J Mech Phys Solids 83:146–159
20. Lee H, Jeon S (2011) An experimental and numerical study of fracture coalescence in pre-cracked specimens under uniaxial compression. Int J Solids Struct 48:979–999. https://doi.org/10.1016/j.ijsolstr.2010.12.001
21. Mak J, Chen Y, Sadek M (2012) Determining parameters of a discrete element model for soil–tool interaction. Soil Tillage Res 118:117–122
22. Mas Ivars D, Pierce ME, Darcel C, Reyes-Montes J, Potyondy DO, Paul Young R, Cundall PA (2011) The synthetic rock mass approach for jointed rock mass modelling. Int J Rock Mech Min Sci 48:219–244. https://doi.org/10.1016/j.ijrmms.2010.11.014
23. Mehranpour MH, Kulatilake PH (2016) Comparison of six major intact rock failure criteria using a particle flow approach under true-triaxial stress condition. Geomech Geophys Geo-Energy Geo-Resourc 2:203–229
24. Nakase H, Annaka T, Katahira F, Kyono T (1992) An application study of the distinct element method to plane strain compression test. Doboku Gakkai Ronbunshu 1992:55–64
25. Park B, Min K-B (2015) Bonded-particle discrete element modeling of mechanical behavior of transversely isotropic rock. Int J Rock Mech Min Sci 76:243–255
26. Park J-W, Song J-J (2009) Numerical simulation of a direct shear test on a rock joint using a bonded-particle model. Int J Rock Mech Min Sci 46:1315–1328. https://doi.org/10.1016/j.ijrmms.2009.03.007
27. Potyondy D, Cundall P (2004) A bonded-particle model for rock. Int J Rock Mech Min Sci 41:1329–1364
28. Scholtès L, Donzé F-V (2012) Modelling progressive failure in fractured rock masses using a 3D discrete element method. Int J Rock Mech Min Sci 52:18–30. https://doi.org/10.1016/j.ijrmms.2012.02.009
29. Schöpfer MP, Abe S, Childs C, Walsh JJ (2009) The impact of porosity and crack density on the elasticity, strength and friction of cohesive granular materials: insights from DEM modelling. Int J Rock Mech Min Sci 46:250–261
30. Shi C, Zhang Y-L, Xu W-Y, Zhu Q-Z, Wang S-N (2013) Risk analysis of building damage induced by landslide impact disaster. Eur J Environ Civil Eng 17:s126–s143
31. Sibille L, Hadda N, Nicot F, Tordesillas A, Darve F (2015) Granular plasticity, a contribution from discrete mechanics. J Mech Phys Solids 75:119–139
32. Tengattini A, Das A, Nguyen GD, Viggiani G, Hall SA, Einav I (2014) A thermomechanical constitutive model for cemented granular materials with quantifiable internal variables. Part I—theory. J Mech Phys Solids 70:281–296
33. Utili S, Nova R (2008) DEM analysis of bonded granular geomaterials. Int J Numer Anal Meth Geomech 32:1997–2031
34. Yang J, Luo X (2015) Exploring the relationship between critical state and particle shape for granular materials. J Mech Phys Solids 84:196–213
35. Yang S-Q, Huang Y-H, Jing H-W, Liu X-R (2014) Discrete element modeling on fracture coalescence behavior of red sandstone containing two unparallel fissures under uniaxial compression. Eng Geol 178:28–48. https://doi.org/10.1016/j.enggeo.2014.06.005
36. Yang X, Kulatilake P, Jing H, Yang S (2015) Numerical simulation of a jointed rock block mechanical behavior adjacent to an underground excavation and comparison with physical model test results. Tunn Undergr Space Technol 50:129–142
37. Yao C, Jiang QH, Shao JF (2015) Numerical simulation of damage and failure in brittle rocks using a modified rigid block spring method. Comput Geotechn 64:48–60. https://doi.org/10.1016/j.compgeo.2014.10.012
38. Yao C, Jiang Q, Shao J, Zhou C (2016) A discrete approach for modeling damage and failure in anisotropic cohesive brittle materials. Eng Fract Mech 155:102–118
39. Zhang X-P, Wong LNY (2012) Cracking processes in rock-like material containing a single flaw under uniaxial compression: a numerical study based on parallel bonded-particle model approach. Rock Mech Rock Eng 45:711–737
40. Zhu H, Nguyen HN, Nicot F, Darve F (2016) On a common critical state in localized and diffuse failure modes. J Mech Phys Solids 95:112–131

Chapter II

Three-dimensional DEM investigation for effect of confining pressure on deformation and failure in anisotropy cohesive materials

Contents

1 Introduction

In large number of underground engineering materials, such as sedimentary and metamorphic rocks, due to the cohesive microstructure often presenting well-defined weakness layer in terms of bedding, stratification, or layering, the deformation and failure mechanism of such materials generally have a distinct anisotropic feature. In order to interpret the failure mechanism, a large number of experiment, theoretical and numerical studies on different kinds of anisotropic rock materials have been so far conducted.

For instance and without giving an exhaustive list, [Jaeger, 1960]; [Hoek and Brown, 1980]; [Nova, 1980]; [Amadei and Savage, 1989] and [Duveau et al., 1998] have first conducted different attempts to take into account the strength anisotropy in their own familiar field. [Niandou et al., 1997] have investigated the effect of the weakness layer on the plastic deformation and failure mechanisms of shale under different confining pressures. [Pietruszczak et al., 2002]; [Tien et al., 2006] and [Lee and Pietruszczak, 2008] have investigated the fracture initiation and propagation of transversely isotropic rock to classify failure modes as sliding and non-sliding failures. [Tavallali and Vervoort, 2010]; [Debecker and Vervoort, 2013] have performed a series of experimental studies of facture parents on disk-shaped layered rock. [Cho et al., 2012] have conducted experiments on three different types of rock to present various deformations and strengths of anisotropic rock. [Fjær and Nes, 2014] have performed uniaxial and triaxial compressive strength tests on Mancos shale to further observe the effect of stress state on failure mechanism. Most of results show that the geometrical and physical properties of weakness layer both have obvious effects on deformation and failure mode of anisotropic material.

The main issue is to capture the generation and propagation of micro-cracks respectively along the weak planes and inside rock matrix and further analyze their impacts on macroscopic responses. In the framework of continuum mechanics, various methods have been developed to describe micro-cracks extension by introducing different enriched shape functions ([Motamedi and Mohammadi, 2012]; [Sosa and Karapurath, 2012]; [Zhao et al., 2016]). However, it is not a simple task to define appropriate criterions and propagation directions of fractures in these methods, even with high order tensors ([Zeng and Yao, 2016]; [Li and Chen, 2016]; [Yun et al., 2017]). In actual, these weakness layer is a series of low strength bonds between mineral grains in anisotropic cohesive materials. The physical processes of deformation and failure are inherently related to bonds breaking or contact interfaces cracking and grain crushing. Therefore, replacing a continuum medium by an equivalent discrete medium, the discrete element methods provide an avenue to explicitly model the initiation and propagation of cracks from micro-scale to macro-scale

without applying complex constitutive law. Without giving an exhaustive list of different approaches ([Gao et al., 2014]; [Yao et al., 2015]; [Yao et al., 2016]; [Alshkane et al., 2017]; [Yang et al., 2017]), the particle flow model is one of the widely used discrete approaches in cohesionless granular materials as well as in cohesive materials, because of its ability to simultaneously consider the combined role of mineral grains and voids ([Cundall and Strack, 1979]; [Potyondy and Cundall, 2004]; [Jiang et al., 2011]; [Shi et al., 2013]; [Yang et al., 2014]; [Mehranpour and Kulatilake, 2016]; [Zhu et al., 2016]; [He et al., 2017]). With different extensions and improvements, this approach has progressively applied to analyze the anisotropic mechanical behaviors in terms of deformation characteristics, strength response, cracks propagation and failure pattern. By introducing smooth joint model to represent continuous weakness planes, [Kwok et al., 2014]; [Park and Min, 2015] have successfully emulated the elastic modulus, Poisson's ratio and strength parameters of transversely isotropic rock. [Chiu et al., 2013] have conducted similar tests on Danba schist with different dip angles and analyzed the anisotropy of joint rock mass using a modified smooth-joint model. [Chu et al., 2013]; [Duan and Kwok, 2015] have directly inserted smooth joint model into bond particles to successfully mimic failure developing process of anisotropic material under different loading conditions. [Wang et al., 2016] have performed two dimensional discrete element modeling of strength variation in jointed rock mass under uniaxial compression. In other respects, [Park and Min, 2015]; [Zhou et al., 2017b]; [Mehranpour and Kulatilake, 2017] have also introduced the smooth joint model in applications of underground engineerings and hydraulic fractures.

However, in most previous studies, by directly using the same bond model and smooth joint model in the Particle Flow Code, regardless of the actual loading conditions, large number of two dimensional compression tests on anisotropic rock have been conducted to describe the anisotropy of deformation and failure. Only a few limited research has been presented in which the failure criterion of shear strength in bond models were taken into account. There are so far limited three dimensional numerical investigations on anisotropic materials considering discrete weakness layer. Further, the effect of the intermediate principal stresses on deformation and failure of anisotropic materials has still necessarily to be studied. Thus, to partially solve the shortcoming of previous studies, a new failure criterion with non-linear shear strength will be first induced in both bond model and smooth joint model for a large range of confining pressures. A generation procedure that describes micro-structure using smooth joint model in anisotropic sample will be then proposed. Moreover, these corresponding elastic and strength parameters related to deformation and failure will also be developed. After systematical calibration

and verification, this modified three dimensional DEM will be applied to investigate the deformation and failure behavior of a typical anisotropic sedimentary rock: the Tournemire shale. In addition, the effect of intermediate principal stresses will also be predicted and discussed.

2 Methodology

In anisotropic cohesive materials, the macroscopic deformation and failure are essentially controlled by the local behavior of inter-granular interface. These existing weakness layers can be considered as a series of lower strength cohesive interfaces that have discrete distributions with same directions. Thus, in this study, two different bond models are introduced and implemented in the standard 3D Particles Flow Code to describe this anisotropic feature: (1) a new bond model applied to model rock matrix response, and (2) a modified smooth join model used for grabbing weakness layer behavior in anisotropic materials.

2.1 Contact stiffness behavior

The state of local stresses at contact controls deformation and failure of bond between particles. Thus two main contact stiffness models, respectively as the linear and Hertz model in PFC3D ([Itasca, 1999]; [Potyondy and Cundall, 2004]; [Manuals, 2008], are adopted to describe elastic and non-elastic behaviors of bonds, relying on the mechanical properties of the studied entities. Therefore, in this research, the linear model is applied to represent the elastic mechanical responses of cohesive materials. Its calculation process is illustrated as the following equations:

$$F_n = k_n u_n \tag{II .1}$$

$$\Delta F_s = -k_s \Delta u_s \tag{II .2}$$

where F_n, k_n and u_n are, respectively, the normal force, normal stiffness and displacement at the contact; ΔF_s, k_s and Δu_s denote, respectively, the shear force, shear stiffness and relative displacements. Note that the normal stiffness, k_n, is a secant modulus that relates to the total displacement and force. The shear stiffness, k_s , on the other hand, is a tangent modulus that relates to the incremental displacement and force.

2.2 Failure criterion for new bond model

According to failure criterion of bond model at contact, the failure status of interfaces can be determined by comparing the calculated local stresses and bond strength. In our previous work, to solve the shortcoming of these familiar bond models in PFC3D, i.e. contact bond model (CBM) and parallel bond model (PBM), that the effect of normal stress on shear strength cannot be correctly described for a large range of normal stress, a new bond model with a nonlinear failure criterion is proposed by [Zhang et al., 2018b], and has been successively applied in describing strength nonlinear properties and micro-cracks propagation in isotropic materials under different confining pressures and loading paths. Here, in order to further apply this bond model to describe nonlinear behavior of matrix in anisotropic materials, a brief introduction will be given as follows.

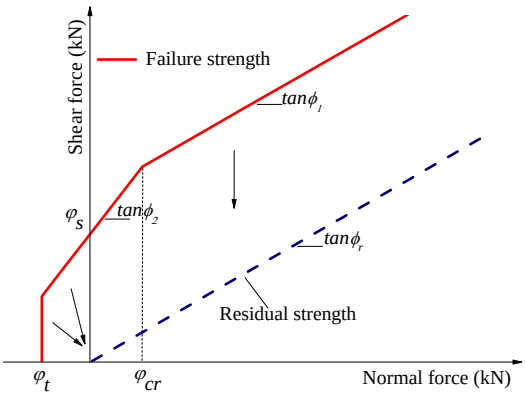

Figure II .1: Peak and residual strength envelope of different bond models in anisotropic material

Two debonding processes should be taken into account in failure analysis of interfaces, i.e. the tensile failure and shear sliding. Such as illustrated in Fig. II .1, in the new bond model with bi-linear failure criterion, the tensile failure occurs when the normal contact force $F_{t,f}$ exceeds the normal strength φ_t. For the shear sliding, the shear strength of interfaces is here approximated by a bi-linear function of normal contact force. When the normal contact force is less than the transition threshold φ_{cr}, the shear strength is defined by the cohesion φ_s and frictional angle ϕ_1. When the normal force is higher than φ_{cr}, a second frictional angle ϕ_2 is introduced with $\phi_2 < \phi_1$ to define the shear strength. The failure criterion for contact interface is then expressed in the following form:

$$F_{t,f} = \varphi_t, \text{tensilefailure} \tag{II .3}$$

$$F_{s,f} = \begin{cases} 0 & ,F_n < \varphi_t \\ \varphi_s + F_n \tan\phi_1 & ,\varphi_t \leq F_n \leq \varphi_{cr} \\ \varphi_s + \varphi_{cr}(\tan\phi_1 - \tan\phi_2) + F_n \tan\phi_2 & ,F_n \geq \varphi_{cr} \end{cases} \text{, shearfailure} \quad \text{(II .4)}$$

Once bonding interface between particles broken, the tensile strength is completely vanished. Due to existing roughness interface at contacts, free slip of particles is constricted, the shear strength reduces to a residual value that is a function of the normal stress and the coefficient of friction acting on the contact surface. For the sake of simplify, the residual strength envelop is shown in Fig. II .1 and the following criterion is formulated:

$$F_{s,r} = \begin{cases} 0 & ,F_n \leq 0 \\ F_n \tan\phi_r & ,F_n > 0 \end{cases} \quad \text{(II .5)}$$

Science slip process mainly affects on residual strength, the residual frictional coefficient $\tan\phi_r$, is set to be a minimum value in the following analysis.

2.3 Smooth joint model

A typical smooth-joint contact between particles in three-dimensional scale is illustrated in Fig. II .2. it was firstly proposed to solve the problem of joints in fractured rock masses. It can model the behavior of a smooth joint by assigning a series of new bonding models with a specified movement orientations to all contacts between particles that lie on opposite side of the joint, regardless of original contact orientations of those adjacent particles. Once bond broken between particles occurs, the particle pairs situating on the opposite site of a joint can past each other with a limited overlap and slide along the pre-defined orientation θ in Fig. II .2 (b), rather than be forced to roll around one another like behaviors in other contact bond models as shown in Fig. II .2 (a).

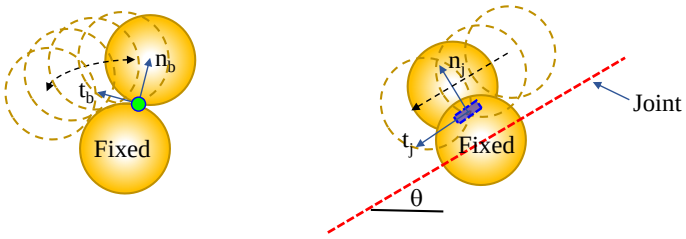

(a) Bond model (b) Smooth joint model

Figure II .2: Comparisons of different mechanical behaviors between two bond models

When there is a smooth joint model inserted between particles, its mechanical property can be inherited from original bond model or can be overwritten by directly assigning property calibrated according the experimental data and field conditions. Different with other two original bond models, such as contact bond model and parallel bond model, the shear strength in failure criterion of smooth joint is not directly assigned to be an equal consistent value, but is described by a linear Mohr-Coulomb type criterion that is defined by the frictional angle and cohesion. However, in this study, for avoiding the shortcoming of this failure type in describing the relationship between normal stress and shear strength, its failure criterion of shear strength is also improved to be the same behavior like aforementioned new bond model such as illustrated in Function (II .3), (II .4) and (II .5). Thus, with an appropriate micro parameters for two bond models, the inherent anisotropy induced by weakness layers distributing along the specified direction in intact rock mass, can be described by inserting the modified smooth joint model into the bonded particle assembly such as shown in Fig. II .3.

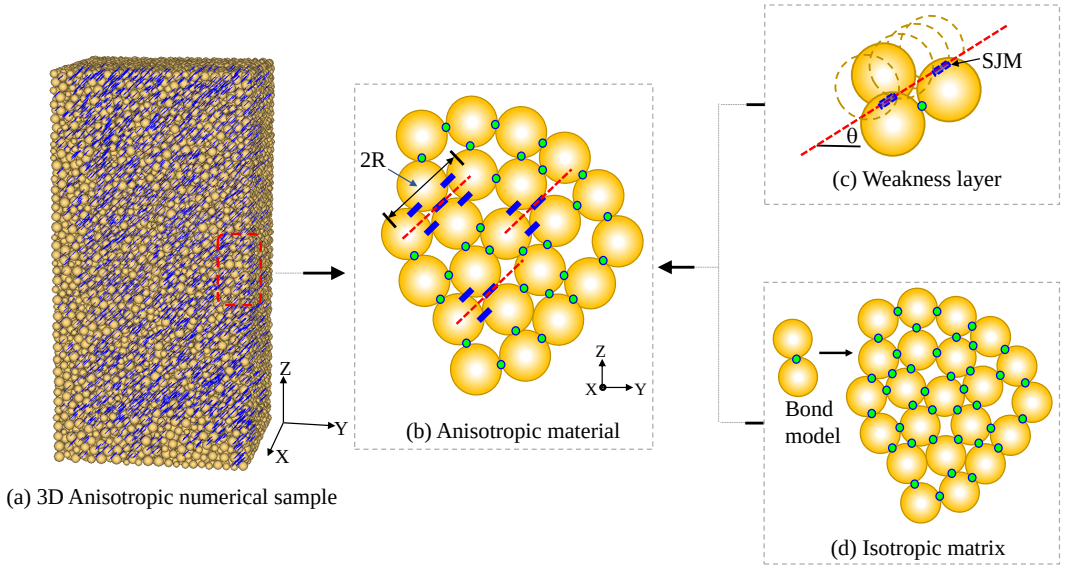

Figure II .3: Illustration of inherent anisotropic numerical sample

3 Generation and verification of anisotropic samples

The spatial geometrical feature for different bonds distribution as well as physical parameters, are both important in describing anisotropy. Therefore, in this section, the detail procedure for generating inherently anisotropic samples are first discussed. Furthermore, those physical parameters related to deformation and failure process, such as local elastic properties and failure criteria of bond models, are also importantly re-defined and evaluated.

3.1 Generation of anisotropic microstructure

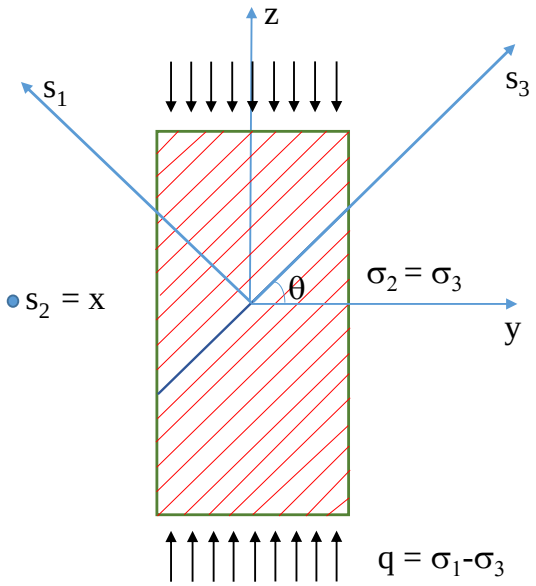

Figure II .4: Definition of weakness layer orientation

The real microstructure of anisotropic materials such as shale is very complex, it is generally not possible to completely reproduce all details of the microstructure. In the present study, the real material sample is replaced by a numerical sample which is an assembly of spherical grains of different diameters, such as Fig. II .3. For generating anisotropic numerical sample, new bond model is first introduced at contacts between particles to mimic isotropic of rock matrix. Then, by inserting smooth joint model at the specified contacts, these samples can be used to describe anisotropic response in terms of strength and failure that is generally induced by microstructure in anisotropic materials, such as bedding planes or weakness layers. In this generation process of anisotropic samples, the key point is capture the formation mechanism of anisotropy in isotropic numerical sample. This procedure mainly includes two steps: (1) seeking the satisfied position of contact as the standard point (O), (2) using smooth joint model to replace relevant bond model in the pre-defined spatial zone (R).

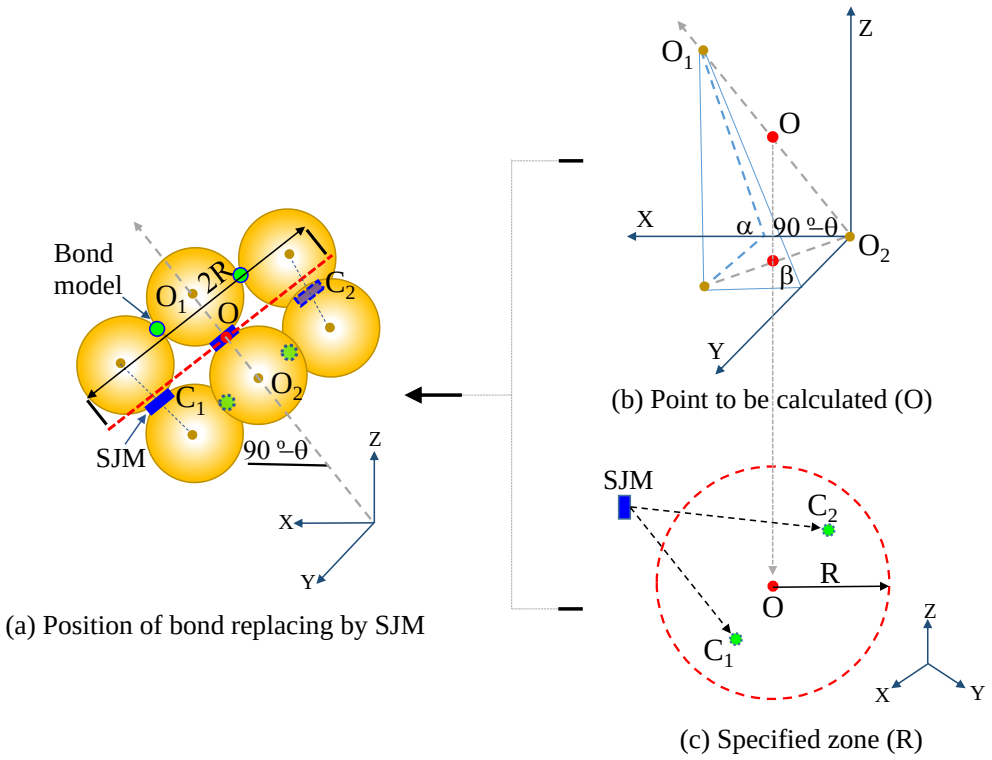

Figure II .5: Determination position of bond model replacing by smooth joint model

As shown in Fig. II .4, according to the definition of orientation θ of anisotropic materials between loading direction and weakness layer commonly used in experiments, the orientation of smooth joint model can be also defined to be θ, with respect to the x-y plane of the overall frame. Due to the coordinate of bond at contact being a spatial value with three dimensional scales, it is difficult to directly distinguish that bond orientation is satisfied or not. However, this problem can be solved by judging the centerline direction of its adjacent particles such as illustrated in Fig. II .5 (a). Assuming that the orientation of satisfied bond takes as θ in Fig. II .5 (b), the centerline direction of two contact particles $(O_1 - O_2)$ is equal to $90 - \theta$ against x-y plane. This spatial orientation $90 - \theta$ can be further divided into two angle, respectively as α in y-z plane and β in x-z plane. If two angles of α and β both meet the specified values, then the satisfied position of bond can be determined as O. After that, regarding point O as a standard position and bond orientation θ as the direction of the pre-defined spatial zone, if the intersection between the connecting line of adjacent sphere centers and the qualified bond contact plane is located in the pre-defined spatial zone R, such as C_1 and C_2 in Fig. II .5 (a) and (b), new bond models at contacts are replaced with the smooth joint models, otherwise not.

3.2 Determination of the specified zone (R)

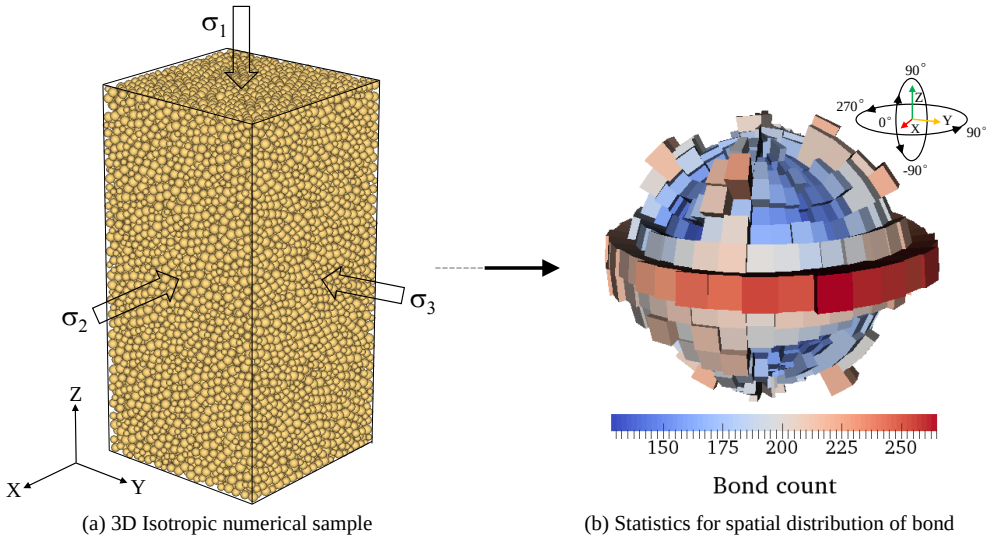

(a) 3D Isotropic numerical sample

(b) Statistics for spatial distribution of bond

Figure II .6: 3D isotropic numerical sample and its bonds spatial distribution statistics

Due to orientation of smooth joint model as well as its amount both closely related to anisotropy for the generated numerical samples, a representative isotropic sample Fig. II .6 (a) with 20000 particles is adopted to conduct statistics analysis for bond spatial distribution. Fig. II .6 (b) clearly shows that the number of bond in horizontal direction is significantly large than in vertical direction. It further means, using the same specified zone R, the amount of bonds replaced by smooth joint model will also deceases with the increase of spatial angle θ. Thus, in order to solve this problem and obtain similar amount distribution for smooth joint model in any kind of anisotropic numerical samples, the specified zone R is defined to be a function of angle θ as follows:

$$\begin{cases} R = (1 + f_R(\theta))\, R_0 \\ f_R(\theta) = r_R \left|\cos(\pi/2 - \theta)\right| \end{cases} \tag{II .6}$$

Where, θ denotes the orientation of weakness layer, R_0 defines the initial range of bond model to be replaced, in this study, it is taken as two-three times of average radius of particles. $f_R(\theta)$ is a introduced function to avoid the effect of uneven distribution of bond in initial isotropic sample.

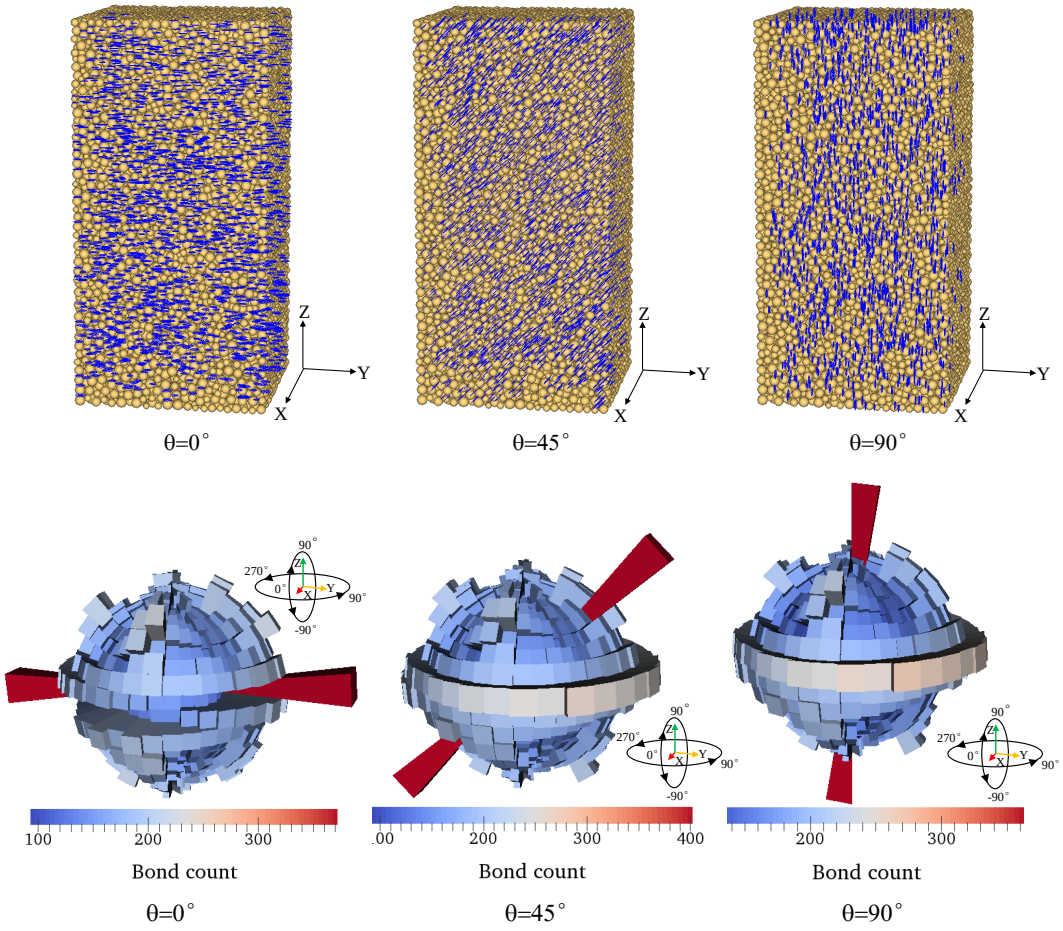

Figure II .7: Three representative numerical samples and corresponding spatial distribution statistics for bonds

Adopting the aforementioned method to replace the qualified bond models with the smooth joint model in the isotropic sample as blue ones. Seven anisotropic numerical specimens with the size of 40.0 * 40.0 * 80.0 mm^3 have been generated by varying orientation from 0° to 90° with 15° as a gap, average radius of particles are taken as 1.0 mm, the pre-defined spatial zone R_0 used for controlling smooth joint model distribution are set as 1 mm and the variable r_R takes as 0.3. There are three representatives presented as shown in Fig. II .7(a). Correspondingly, different types of bond models distribution are counted according to their direction and presented in Fig. II .7(b). The number of smooth joint model in each anisotropic samples is nearly about 400. The results further manifest that the aforementioned method for generating anisotropic samples can well describe the microstructure in anisotropic materials.

3.3 Definition of elastic parameters

As mentioned above in section 2, at the local level, the elastic property for isotropic material is actually controlled by deformation of bond at contact which is characterized by the normal and shear stiffness coefficients k_n and k_s. Different with stiffness parameters taking same values in isotropic material simulations, for modeling anisotropic materials, these elastic parameters are redefined as the following relations:

$$\begin{cases} k_n = (1 + r_k \cdot f(\phi,\theta)) \cdot k_{n0}, k_s = (1 + r_k \cdot f(\phi,\theta)) \cdot k_{s0} \\ k_{n0} = 2E_c \cdot (R_1 + R_2), k_{s0} = k_r \cdot k_{n0} \\ f(\phi,\theta) = a/\left(b + (1-b)\, e^{-c\delta}\right) - a, \delta = \arctan|\tan(\phi - \theta)| \end{cases} \text{, elasticparameters} \quad \text{(II .7)}$$

Where, E_c is contact elastic modulus having the same order of magnitude as that of the macroscopic Young's modulus E. R_1 and R_2, respectively, denote the radiuses of the neighbouring particles, k_r is the ratio between k_n and k_s, which is related the Poisson's ratio υ and generally taken as 1.0-3.0. k_{n0} and k_{s0} are the initial stiffness coefficients for interface in normal and shear direction respectively.

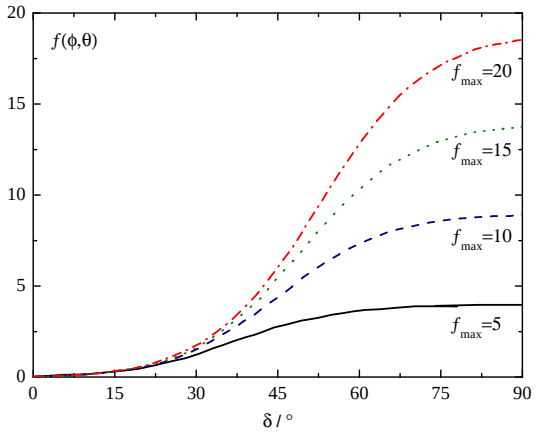

Figure II .8: Illustration of the function $f(\phi,\theta)$, $\delta = \arctan|\tan(\phi - \theta)|$

The $f(\phi,\theta)$ is a introduced function that presents a "S" type to define the ratio between the stiffness of bond in the direction of ϕ and in the pre-defined orientation of θ ([Yao et al., 2016]). Such as shown in Fig. II .8, setting variables a and c both equal to be 0.1, The values of $f_{\max}$ have significant increase trends with the decrease of variable b. And for one consistent value of b, the values of $f(\phi,\theta)$ have also obvious increase trends with the increase of relative angles δ. It fuhrer indicates that, in micro-scales, the introduced

function $f(\phi,\theta)$ can well consider the effect of different relative angles δ between ϕ and θ on deformation property.

3.4 Definition of strength parameters

Correspondingly, there are five physical parameters involved in failure criterion of interface, such as normal strength φ_t, shear strength φ_s, two frictional coefficients $\tan\phi_1$, $\tan\phi_2$, and the transition threshold of the normal force φ_{cr}, should be redefined to describe the strength anisotropy in numerical sample caused by the smooth joint model with same specified sliding direction θ. According to the previous study, two main failure parameters as normal and shear strength (φ_t, φ_s) that have significant effect on peak strength responses. Thus, their new definitions are expressed to be functions of the bond orientation ϕ with respect to the smooth joint model direction θ as follows:

$$\begin{cases} \varphi_t = (1 + r_s \cdot f(\phi,\theta)) \cdot \varphi_{t0}, \varphi_s = (1 + r_s \cdot f(\phi,\theta)) \cdot \varphi_{s0} \\ f(\phi,\theta) = a \big/ \left(b + (1-b)\, e^{-c\delta}\right) - a, \delta = \arctan\left|\tan(\phi - \theta)\right| \end{cases}, \text{failureparameters} \quad \text{(II .8)}$$

Where, φ_{t0} and φ_{s0} are the initial strength for bond, respectively, in normal and shear direction. Similarly to the definition of stiffness parameters, the function of $f(\phi,\theta)$ is employed again for describing the effect of weakness layer inclination on macroscopic strength behavior.

Table II .1: Input parameters for $f(\phi,\theta)$ used in three-dimensional DEM simulations

Parameters used in $f(\phi,\theta)$	**Elastic parameters**	**Strength parameters**
Variables a, c	0.1, 0.1	0.1, 0.1
Variables b, $f_{\max}$	$1.23 * 10^{-2}$, 9.0	$1.23 * 10^{-2}$, 9.0
Variable r_k	1.0	–
Variable r_s	–	0.15

4 Three-dimensional simulation of conventional triaxial compression test

In order to further validate the above method in application of describing anisotropy, three-dimensional studies of conventional triaxial compression tests are also performed.

Numerical results are compared with experimental data obtained on shale.

4.1 Experimental test

The experimental tests were performed on a typical anisotropic sedimentary rock, i.e. Tournemire shale, by [Niandou et al., 1997], in Laboratory of Mechanics of Lille, France. This type material was drilled from an experimental tunnel in the Massif Central and has been largely applied in engineering, such as the geological disposal of radioactive waste and unconventional gas exploration. Due to existing a set of weakness layer in this material, these experimental results show that, both elastic properties and mechanical strength clearly exhibit a strong inherent anisotropy and depend on the loading orientation. Thus, in this study, the experimental data will be used for the verification of the proposed method.

4.2 Calibration of model's parameters

For conducting simulations against anisotropy behaviors of Tournemire shale, the first step is generating a isotropic sample. Such as Fig. II .7 , the numerical sample is a cuboid of 40.0 mm wide and 80.0 mm high. It is constituted about 20,000 particles with uniform distribution. The largest radius of particle is 1.2 mm, and the smallest one is 0.8 mm, other geometric parameters can be found in Table 1 and Table 2. In order to emerge micro-structure of anisotropic material on this isotropic sample, such as weakness layers, the above algorithm used to inset smooth joint model has also been performed. In this procedure, angles α and β respectively takes as $\pm 5^{\circ}$ and $\pm 4^{\circ}$, and the critical zone R_0 is assigned as 2.0 mm. After this process complete, there are still two groups parameters of interfaces need to be identified from experimental data, respectively as elastic and strength parameters.

In calibration on anisotropic elastic modulus, the main process includes the following steps: Firstly, setting strength parameters as maximum value in both bond model and smooth joint model for eliminating the effect of failure on elastic response, the coefficient k_r related to Poisson ratio υ is initially set a common value of 2.0. The value of $f_{\max}$ in function $f(\phi, \theta)$ firstly takes as 5.0. When the orientation of weakness layer in anisotropic sample is equal to be 0°, the initial stiffness, k_{n0}^{0}, k_{s0}^{0}, k_{n}^{0} and k_{s}^{0} are first directly obtained according to contact elastic modulus E_{C}^{0}, which is depended on Young's modulus E^{0}. As the inclination angle of weakness layer is equal to 90° , the corresponding stiffness k_{n}^{90}, k_{s}^{90} can be calculated by comparing elastic modulus E_{C}^{90} and E^{90}, then the value of $f_{\max}$ can be also checked. Thus, the first calibration process on elastic ends. After several

adjustments, the final elastic parameters of two bond models can be obtained.

As for identifying strength parameters, there are about 11 variables in two contact models need to be completed. Thus, two representative anisotropic samples with weakness layer orientation of 0° and 45° are used to respectively calibrate strength parameters of new bond model and smooth joint model. Similarly to match elastic parameters, The initial value of $f_{\max}$ in function $f(\phi, \theta)$ also takes as 5.0. When the weakness layer inclination is 0°, its effect on strength is slightly. For the sake of reducing the number of independent parameters, strength parameters in two bond models are initially set same values and two frictional coefficients $\tan\phi_1$ and $\tan\phi_2$ in each models are also set as the same initial values. Then, by reducing the normal and shear bond strengths φ_t, φ_s, the peak strength between numerical results and experimental data can be approximately matched. When the inclination of weak plane is 45°, keeping strength parameters of new bond model unchanged, the aforementioned procures can be also used to calibrate strength parameters in smooth joint model. It should be noticed that the aforementioned calibration process of strength is carried out under one confining pressure. Frictional coefficients $\tan\phi_1$ and $\tan\phi_2$, and the transition threshold φ_{cr} are need to be further adjusted for other confining pressures. Then, the first identification on strength is finished under the assumption of $f_{\max}$ as 5,0. Afterwards, using limited times to check, these strength parameters in two bond models can be matched, finally.

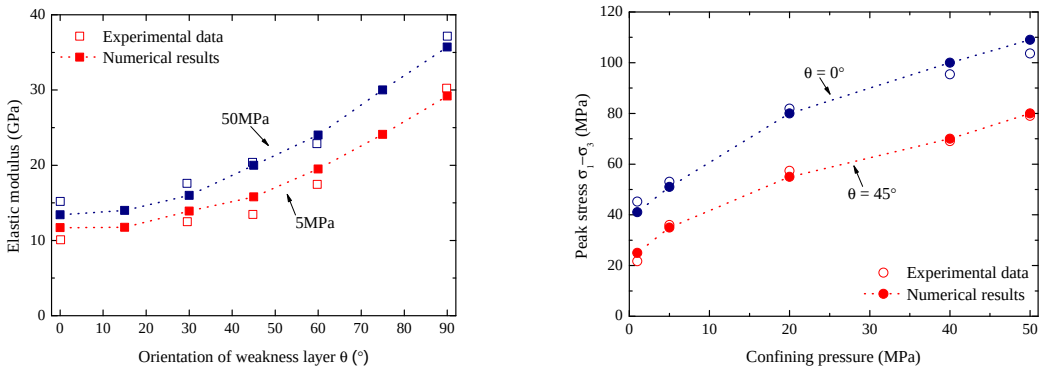

(a) Elastic modulus (b) Peak stress

Figure II .9: Comparison of elastic and strength responses between numerical results (dotted lines) experiment data (solid points)

Thus, by adopting the numerical optimal procedure mentioned above, the final numerical results predicted for elastic modulus and strength envelops are respectively illustrated in Fig. II .9(a) and II .9(b). There is a good agreement between numerical results and

experimental data.

Table II .2: Geometrical, physical and mechanical parameters for a new bond model and the modified smooth joint model used in three-dimensional DEM simulations

3D Sample			
Width of sample (mm)	W		40.0
Height of sample (mm)	H		80.0
Total grain number in sample			20916
Average radius (mm)	$\overline{r}$		1.0
Initial void ratio			0.2
Initial judgement range (mm)	R_0		2.0
Coefficient r_R in function $f_R(\theta)$	r_R		0.5
Mechanical parameters		**New bond model**	**Smooth joint model(SMJ)**
Normal contact stiffness for test (N/m)	k_{n0}	$5.6 * 10^8$	$8.0 * 10^8$
Shear contact stiffness for test (N/m)	k_{s0}	$2.8 * 10^8$	$4.0 * 10^8$
Inter-particle coefficient of friction	$tan\phi_1$	1.9	1.3
Inter-particle coefficient of friction	$tan\phi_2$	0.36	0.6
Normal bond strength (N)	φ_{t0}	$2.5 * 10^4$	$0.42 * 10^4$
Shear bond strength (N)	φ_{s0}	$8.0 * 10^4$	$0.73 * 10^4$
The critical normal stress (N)	φ_{ncr}	$2.0 * 10^5$	$1.5 * 10^5$
Inter-particle coefficient of friction	$\tan\phi_r$	0.05	0.05

Note: These parameters for SMJ is conversion values calculated according to average radius $\overline{r}$.

4.3 Strength analysis and comparison with experiment

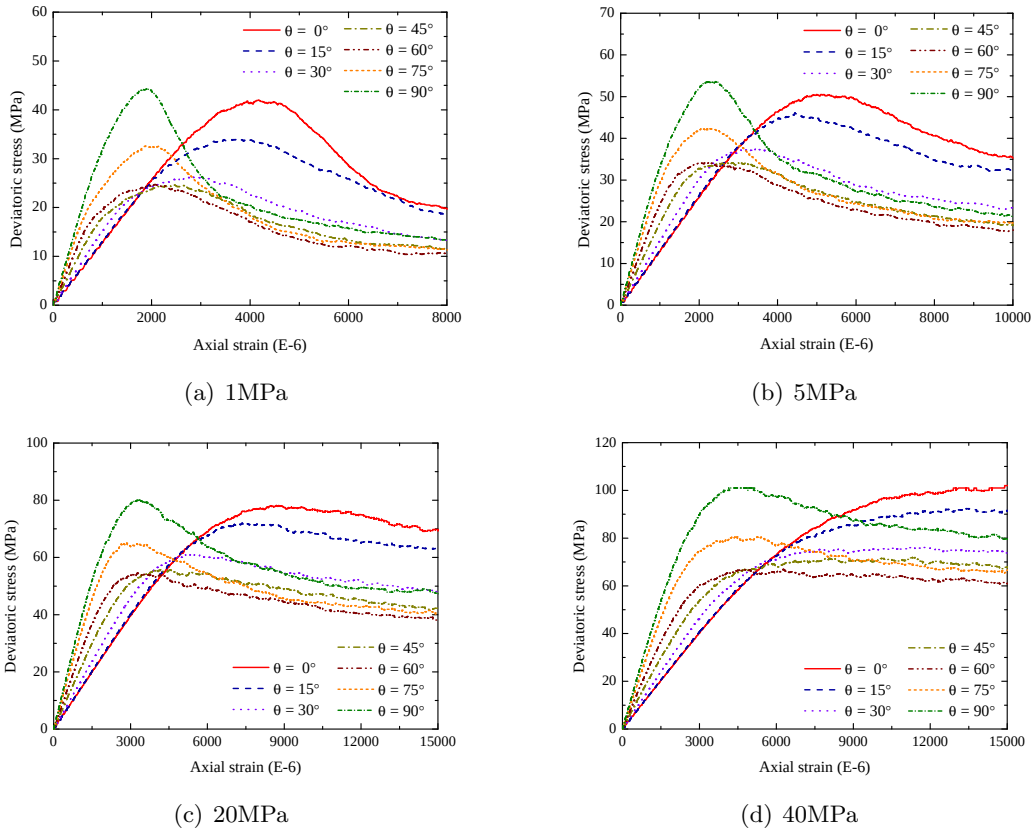

(a) 1MPa (b) 5MPa

(c) 20MPa (d) 40MPa

Figure II .10: Stress-strain curves of specimens with different weakness layer orientations under various confining pressures

Using these model's parameters for new bond model and smooth joint model defined and given in Table 1 and Table 2, a series of conventional triaxial compression tests on Tournemire shale are conducted with different confining pressures, such as 1MPa, 5MPa, 20MPa, 40MPa and 50MPa. In order to facilitate numerical result analysis, four representative stress-strain curves of samples with different weakness layer are listed in Fig. II .10, an obvious anisotropy in both deformation and strength is presented, clearly. It can be seen that, similar to most rock-like materials, the peak strength as well as residual strength both become larger with the increase of confining pressure. Differently, for the same confining pressure, both of them are also influenced by the loading orientation. And then, for a quantitative comparison, the numerical values of peak deviatoric vs experimental data are further given and has a good agreement such as shown in Fig. II .11. One can notes that, the peak stress of shale clearly depends on both the loading orientation

θ and confining pressure. There are two maximum values obtained either at 0° or 90°, which seem equal to each other. And the minimum values commonly occurs between 30° and 60° for all confining pressure.

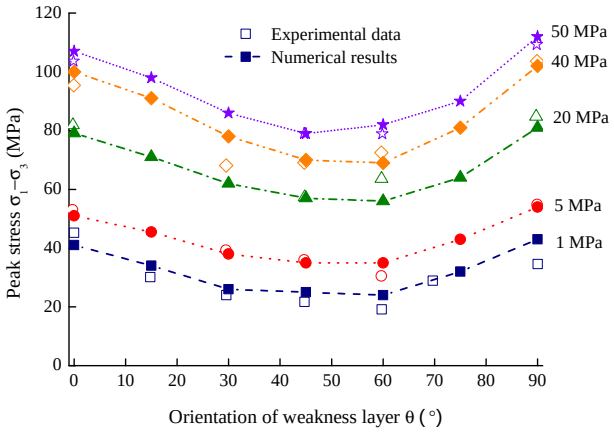

Figure II .11: Peak deviatoric stress versus orientation of weakness layer for tournemire shale under compression with various confining pressures

In general, for anisotropic materials, there are two familiar parameters as follows, to define the anisotropy degree of strength:

$$K_1 = \frac{(\sigma_1 - \sigma_3)_{\parallel}}{(\sigma_1 - \sigma_3)_{\perp}} \tag{II .9}$$

$$K_2 = \frac{(\sigma_1 - \sigma_3)_{\max}}{(\sigma_1 - \sigma_3)_{\min}} \tag{II .10}$$

Where, K_1 means the ratio between the failure stresses in two principal directions, respectively, parallel and perpendicular to the bedding planes, and K_2 denotes the ratio between the maximum and minimum strength.

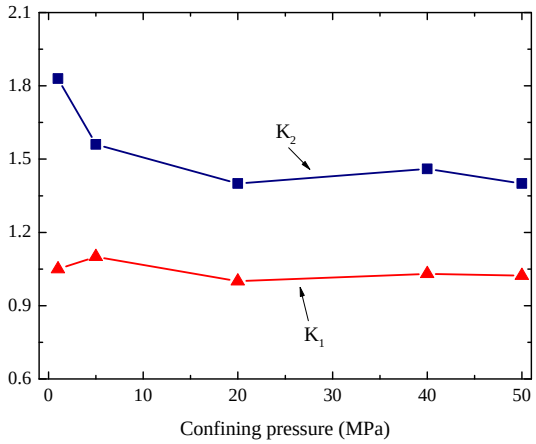

Figure II .12: Variation of anisotropy degree of mechanical strength versus confining pressures

The values of two parameters obtained form simulation for Tournemire shale are illustrated in Fig. II .12. It can be seen that, K_1 is closely to 1.0, indicating that the strength anisotropy between the two principal direction is very small. The value of K_2 has a trend that gradually decreases from 1.96 to 1.47 with the increase of confining pressure from 1Mpa to 50 Mpa, which implies the strength anisotropy will be weakened under high confining pressure. The simulation results are also similar to most experimental data obtained from other anisotropic rocks ([Duveau et al., 1998]; [Niandou et al., 1997]; [Yao et al., 2016]. Thus, according to these comparsion results between numerical results and experimental data, the method that uses smooth joint model to simulate mechanical behavior of weakness layer behavior, has a good performance in predicting the mechanical strength of anisotropic materials.

5 Failure process in anisotropic cohesive granular materials

At local level, the deformation and failure process in such materials is inherently controlled by the breakage of bonded contact interface between grains. Using the proposed method, the transition from diffused micro-cracks to localized fractures in anisotropic materials under different confining pressure is here investigated in terms of statistical analysis for micro-cracks spatial distribution.

5.1 Spatial distribution of micro-cracks

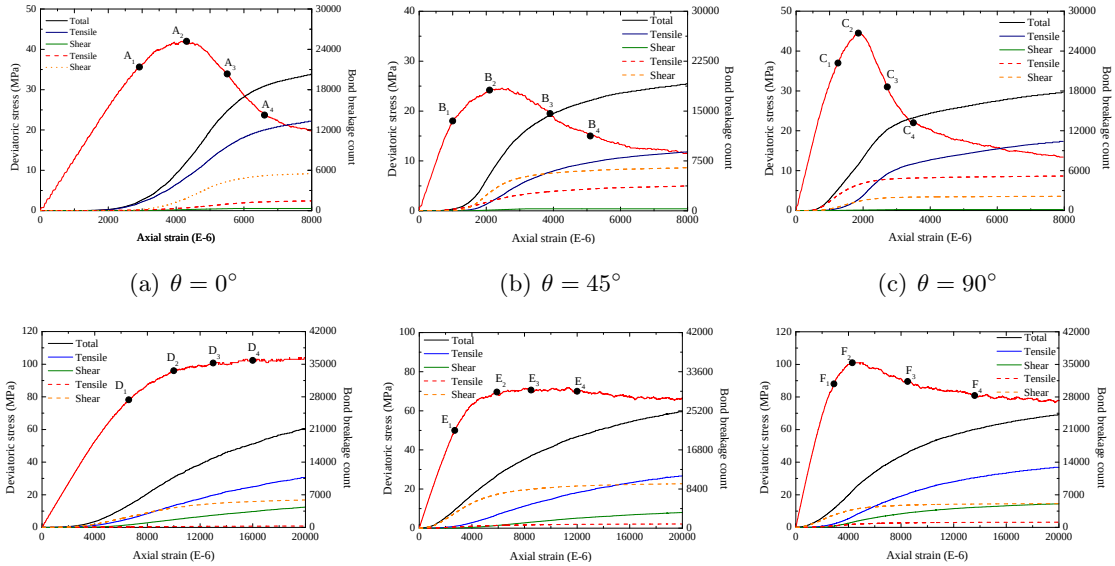

(a) $\theta = 0°$ (b) $\theta = 45°$ (c) $\theta = 90°$

(d) $\theta = 0°$ (e) $\theta = 45°$ (f) $\theta = 90°$

Figure II .13: Illustrations for different micro-cracks evolution in samples under confining pressures of 1MPa and 40MPa (black: total number, red, yellow: tensile and shear failure in weakness layer, blue, green: tensile and shear failure in matrix)

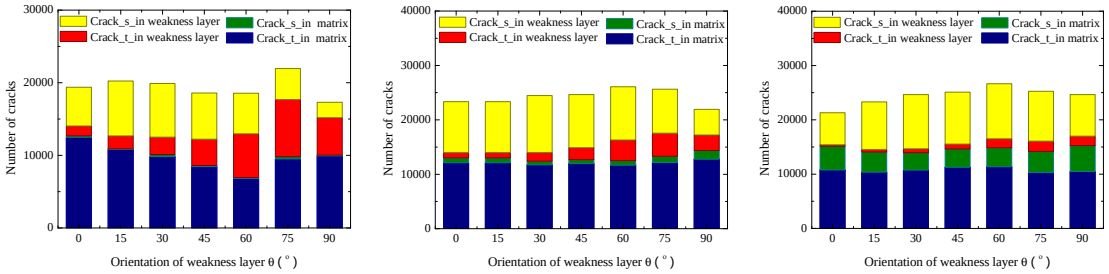

(a) $1MPa$ (b) $20MPa$ (c) $40MPa$

Figure II .14: Micro cracks evolution for different bond models after failure in specimens with various orientations under different confining pressures

Fig. II .13 clearly shows the change of amount of different micro-cracks changes with weakness layer inclination θ under different confining pressures as 1MPa, 40MPa. Such as shown in Fig. II .14, when confining pressure is low, since the ratio of failure bonds of smooth joint model in total number of micro-cracks is higher, especially for $\theta \geq 30°$, it seems that the failure of anisotropic sample is mainly depended on micro-cracks developing

in weakness layer. While confining pressure increases larger, the ratio decreases gradually and sample failure becomes be caused by micro-cracks developing in both weakness layer and shale matrix.

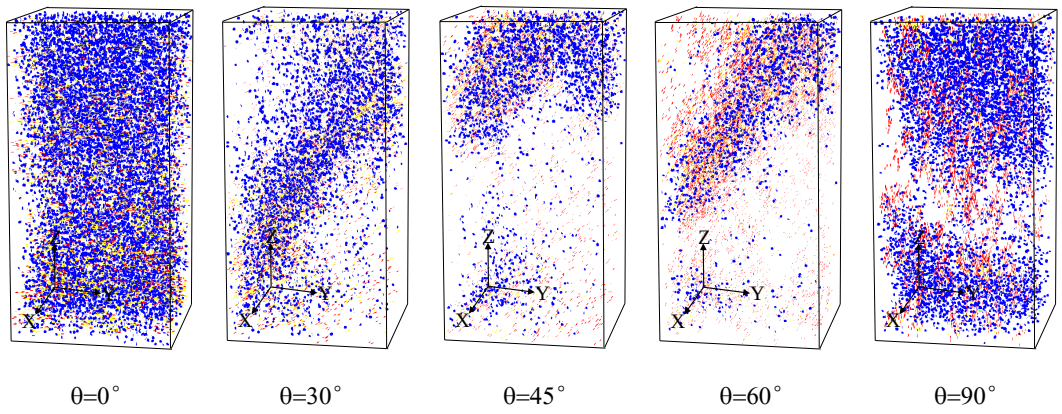

(a) $1MPa$

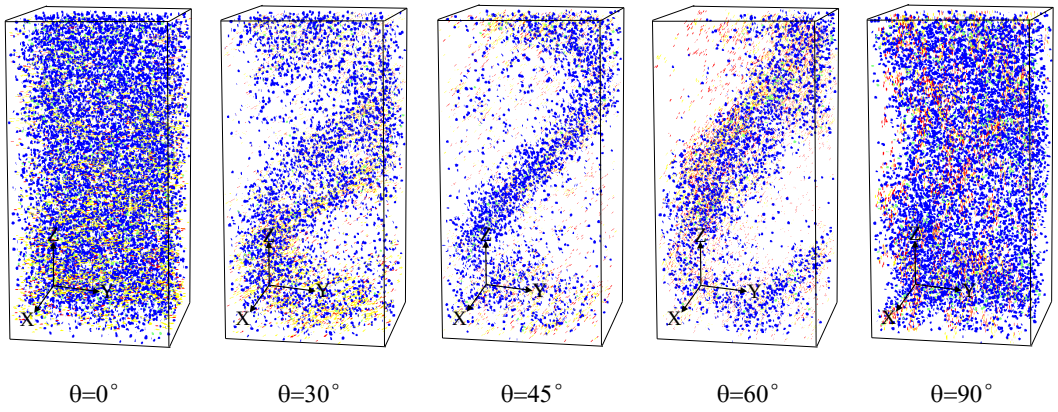

(b) $20MPa$

Figure II .15: Spatial distribution of micro cracks for different bond models after failure in specimens with various orientations

In addition, Fig. II .14 and Fig. II .15 further show that, for loading orientations nearly perpendicular to the weakness layer $\theta = 0°$, the failure is mainly caused by shear sliding in smooth joint model and tensile splitting in new bond model under low confining pressure of 1MPa, and becomes be induced by shear sliding in both two bond models when confining pressure becomes large. The loading orientation is in the range of $15° \leq \theta \leq 60°$, the failure occurs mainly controlled by the shear sliding and tensile splitting in smooth joint model for low confining pressure, and determined by shear sliding in both two bond models under large confining pressure. Then, as loading orientation nearly parallel to the

weakness layer orientation $\theta = 90°$, the reason that leads to anisotropic sample failure, is changed from tensile splitting to shear sliding in both two bond models with the increase of confining pressure.

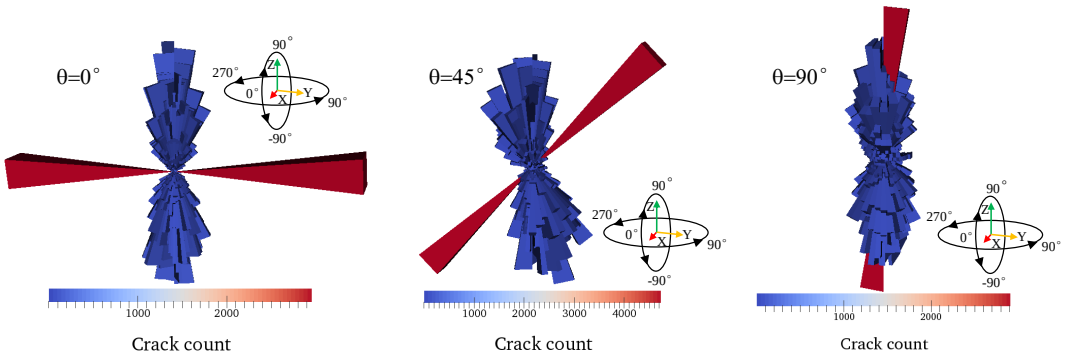

(a) 1MPa

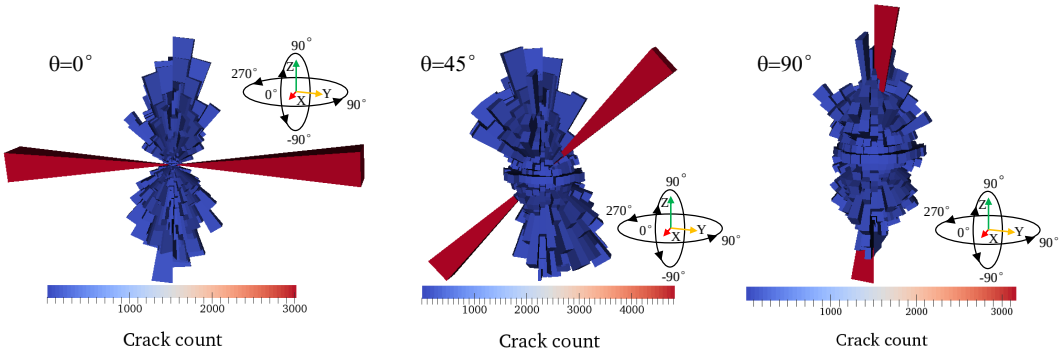

(b) 40MPa

Figure II .16: Statistics for spatial angle distribution of micro-cracks after failure in specimens with various orientations

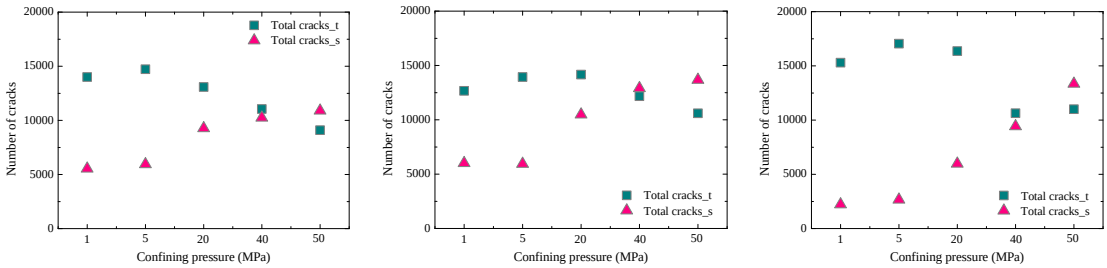

(a) $\theta = 0^\circ$ (b) $\theta = 45^\circ$ (c) $\theta = 90^\circ$

Figure II .17: Total of micro-cracks evolution after failure in samples with various orientations under compression with different confining pressures (red: tensile failure, green: shear failure)

Moreover, for further investigating the relationship between orientations of failure bonds and local failure inclination, the statistics analysis against spatial distribution of failure bonds have been performed. Such as Fig. II .16, one can note that, when confining pressure is low as 1MPa, these failure bonds induced by tensile splitting generally has a large orientation angle and a relatively concentrated distribution, it often leads to local failure band presenting steeper. While the confining pressure increases to 40MPa, the number of failure bonds with low orientation induced by shear siding significantly increases, and thus resulting in a large range local failure band, and with a low inclination angle. This phenomenon can be also interpreted by the change of total amount of micro-cracks. Fig. II .17 clearly presents that, no matter the orientation angle θ in anisotropic sample is large or small, the number of failure bonds both changes from be mainly controlled by tensile splitting under low confining pressure, to be occupied by shear sliding for the high confining pressures.

5.2 Displacement description

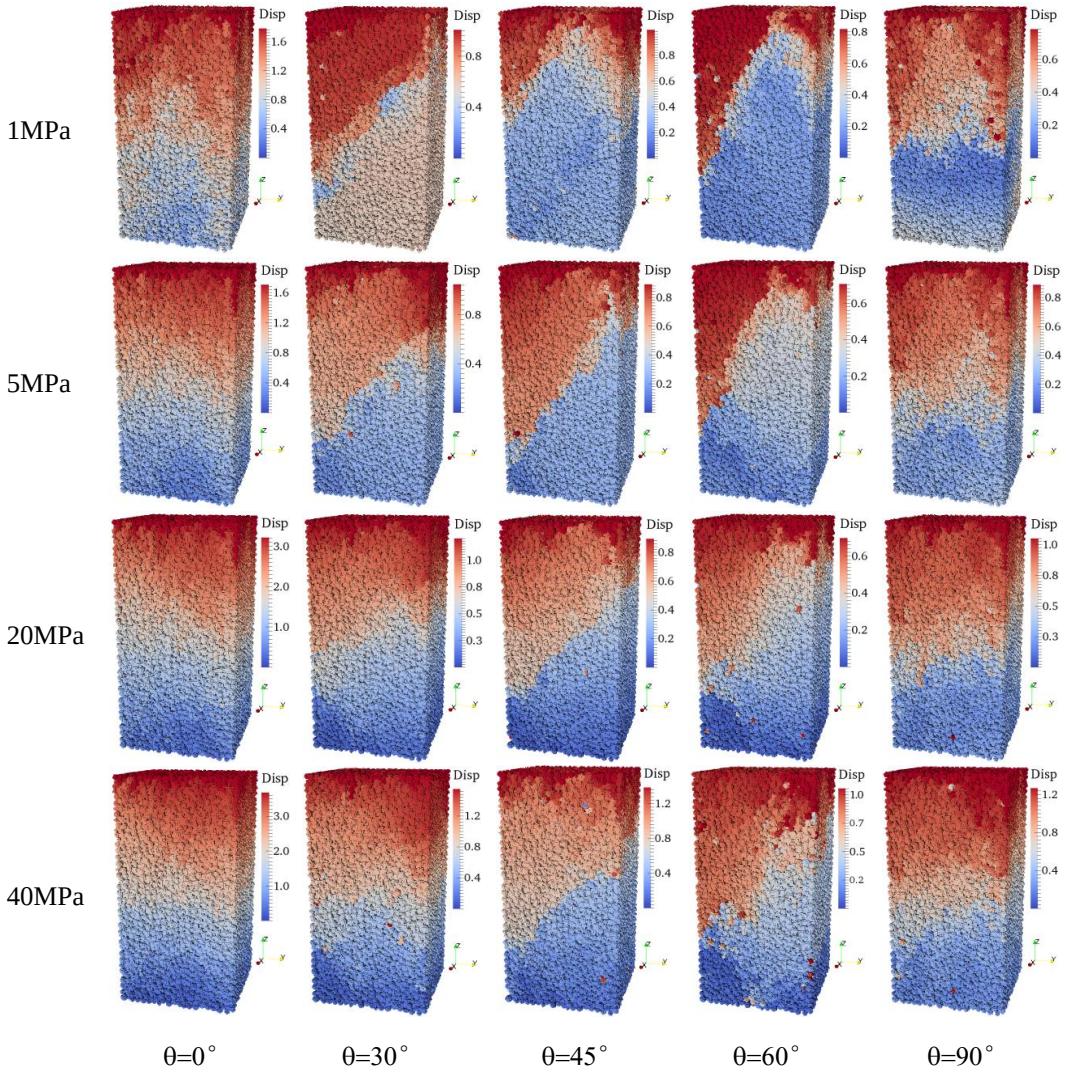

Figure II .18: Displacement fields after failure in samples with various orientations under compression with different confining pressure

On the other hand, the displacement distribution after failure inside the three dimensional is also measured and shown as Fig. II .18. One can note that, the displacement distribution is also affected by confining pressures and weakness layer orientation. Under low confining pressure as 1MPa, there exists an obvious inclined narrow band has a larger inclination angle in specimen with an important displacement gradient on the boundary between this band and outside zones, especially for the orientation between 30° and 60°. However, with the increase of confining pressures, the inclination angle with the axial load

axis increases and the displacement gradient becomes indistinct. And finally, a large and quasi horizontal zone is formed in the central part of specimen, such as confining pressures of 40MPa. However, the distribution of displacement for specimen after failure can only describe the overall behavior of the failure part, and not reflect the localized fractures. Thus, the failure coefficient is proposed and defined as the following equation:

$$F_{coe} = \frac{|D_{i+1} - D_i|}{|(D_{i+1} - D_i)_{\max}|} \tag{II .11}$$

Where $(D_{i+1} - D_i)$ denotes the variation of displacement between adjacent particles, and $(D_{i+1} - D_i)_{\max}$ is the biggest values. The failure coefficient distributing in specimen is presented as Fig. II .19. One can obtain that, the localized fractures has the similar propagation mechanism with the failure evolution of micro-cracks such as Fig. II .15. For the orientation $\theta = 0°$, the distribution of localized fractures exists in weakness layer and shale matrix, regardless of low or high confining pressures. When it is in the range 30° and 60°, under low confining pressure, the fractures bands are mainly distributed parallel to the weakness layer orientation. While confining pressures is higher, they exist in both of them. Finally, as loading orientation is equal to 90°, the perpendicular localized fractures mainly developing in bedding plane can be found under low confining pressures, but they become inclined fractures when confining pressures increases.

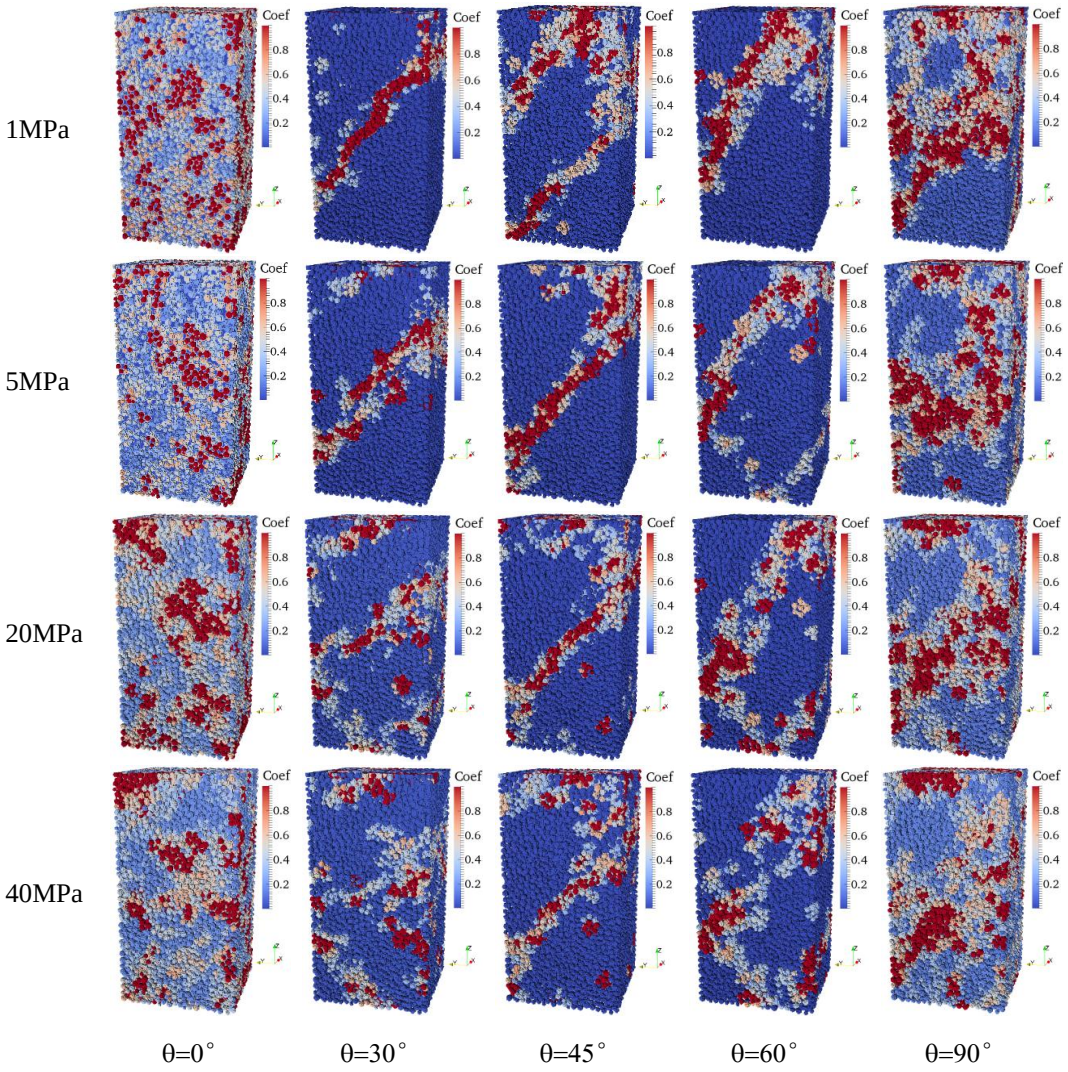

Figure II .19: Localized fractures coefficients of samples with various orientations under compression with different confining pressure

6 Further investigation for effect of intermediate principal stresses on anisotropy

In the anisotropy analysis considered above, two principal stresses are identical ($\sigma_2 = \sigma_3$). Based on this kind of experimental data, most mechanical properties and failure model investigated for anisotropic materials involve the major and minor principal stresses only, the role of intermediate principal stresses is generally neglected. However, in general loading conditions, three principal stresses are different and independent. Therefore, the effect of the intermediate principal stresses on failure and deformation of anisotropic materials

is needed to further investigate.

6.1 Effect of strength

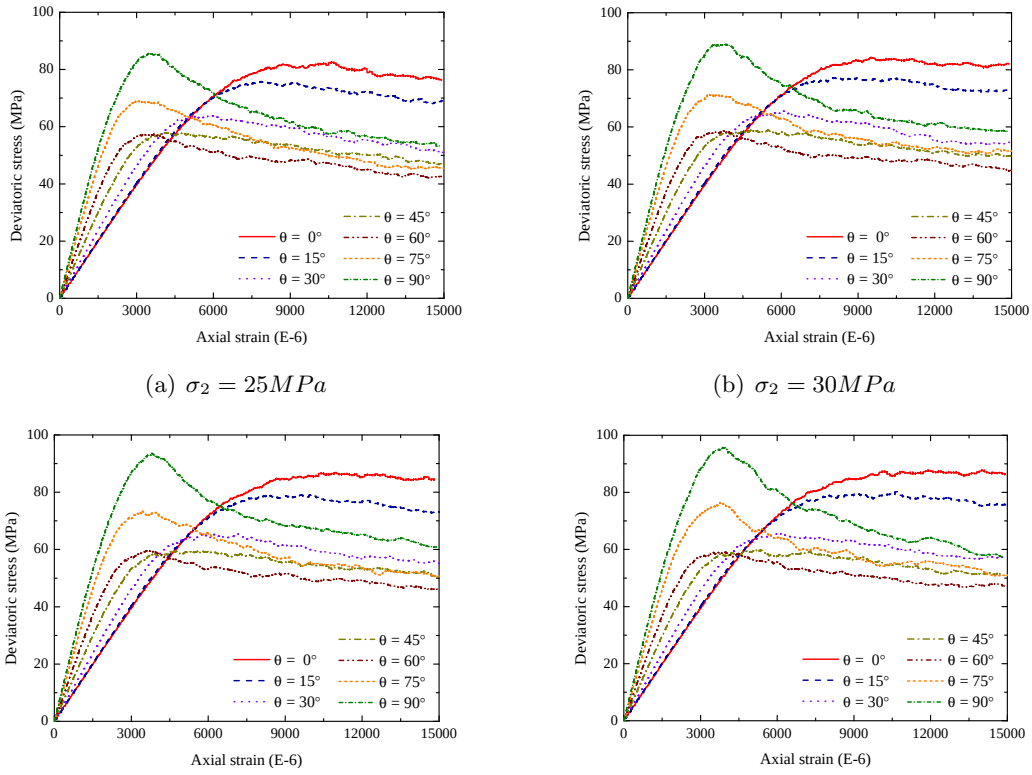

(a) $\sigma_2 = 25MPa$ (b) $\sigma_2 = 30MPa$

(c) $\sigma_2 = 35MPa$ (d) $\sigma_2 = 40MPa$

Figure II .20: Stress-strain curves of samples with different weakness layer orientations under different intermediate principal stresses σ_2 ($\sigma_3 = 20MPa$)

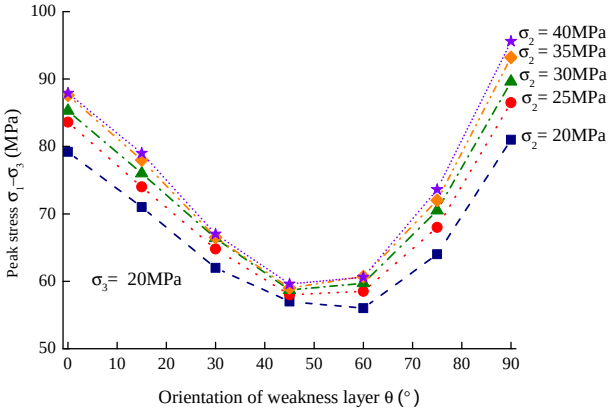

Figure II .21: Peak deviatoric stress versus orientation of weakness layer for tournemire shale under different intermediate stresses

For this purpose, by adopting the same parameters as those given in Table 1 and Table 2, we have performed a series of numerical tests. The minor principal stress σ_3 is kept to be constant and equal to 20MPa. Different values of the intermediate principal stress σ_2 are considered ranging from 20MPa to 40MPa . For a selected set of two principal stresses, the axial strain is prescribed in order to generate the variation of axial stress which is the major principal stress. Such as Fig. II .20, the differential stress $(\sigma_2 - \sigma_3)$ versus axial strain (ε_1) curves are firstly presented for four different values of the intermediate principal stress (σ_2). One can observe that, those peak strengths both increase with the increase of intermediate principal stress, regardless of the loading orientation in anisotropic materials. In order to distinct distinguish the increase amplitude of peak strength for anisotropic samples with different weakness layer, the peak values are also presented in Fig. II .21. It can be obtained that, the increase of peak strength induced by the same increment of intermediate principal stress has a gradual decrease trend in all of the anisotropic specimens. Compared with the loading orientation in the range of $15° \leq \theta \leq 75°$, the peak strength increment is more obvious when the orientation is equal to $0°$ or $90°$. It further implies that the increase of intermediate stress σ_2 will lead to more obvious anisotropic features of strength. This phenomenon is also verified with the statistics values of K1 and K2, such as shown in Fig. II .22.

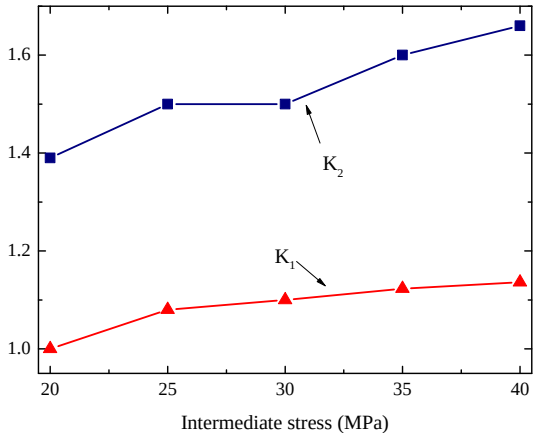

Figure II .22: Variation of anisotropy degree of mechanical strength versus intermediate stresses

6.2 Effect of failure mechanism

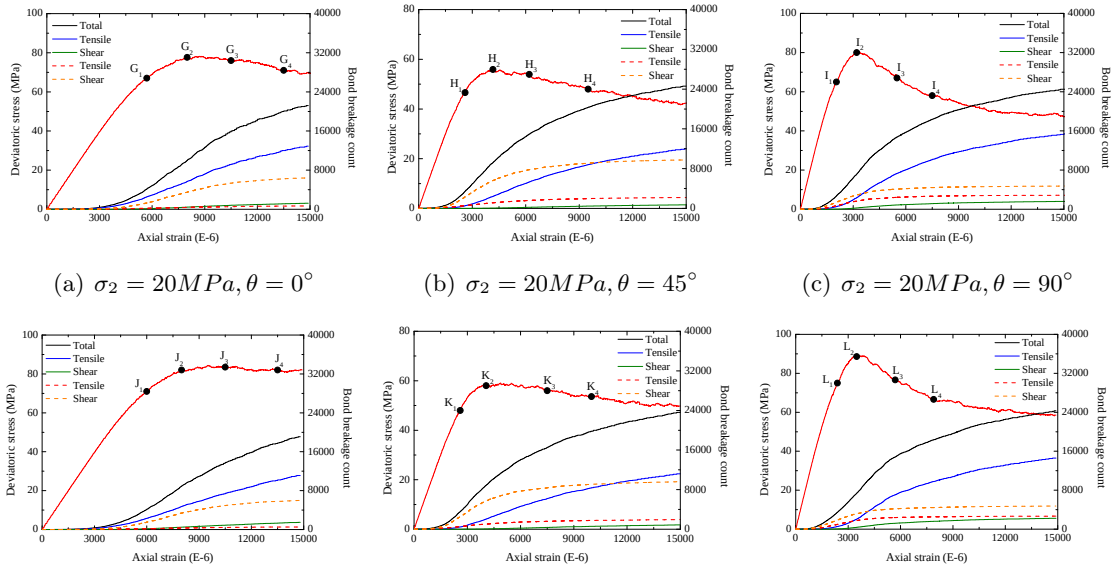

(a) $\sigma_2 = 20MPa, \theta = 0°$ (b) $\sigma_2 = 20MPa, \theta = 45°$ (c) $\sigma_2 = 20MPa, \theta = 90°$

(d) $\sigma_2 = 40MPa, \theta = 0°$ (e) $\sigma_2 = 40MPa, \theta = 45°$ (f) $\sigma_2 = 40MPa, \theta = 90°$

Figure II .23: Illustrations for different micro-cracks evolution in samples under intermediate stresses σ_2 of 20MPa and 40MPa (black: total number, red, yellow: tensile and shear failure in weakness layer, blue, green: tensile and shear failure in matrix)

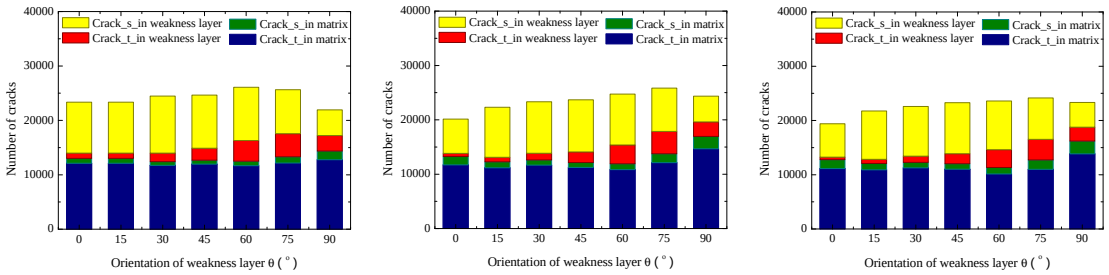

(a) $\sigma_2 = 20MPa$ (b) $\sigma_2 = 30MPa$ (c) $\sigma_2 = 40MPa$

Figure II .24: Micro-crack evolutions for different bond models after failure in samples with various orientations under compression with different intermediate stresses σ_2

In order to explore the effect of different intermediate principal stress σ_2 on failure process of anisotropic samples, the evolution of tensile and shear micro-cracks in both weakness layer and shale matrix are presented in Fig. II .23, when σ_2 are respectively equal to 20MPa and 40MPa. Fig. II .24 shows that, while the total amount of micro-cracks remains similar, the ratio of different micro-cracks has also slightly changed with the increase of difference of two lateral stresses $(\sigma_2 - \sigma_3)$, especially for weakness layer orientation θ equal to 0° and 90°. The repartition distribution of micro-cracks between tensile splitting and shear sliding is clearly presented in Fig. II .25 and shows a slight decease trend of micro-cracks caused by tensile failure. This phenomenon can be further explained from statistics analysis for micro-cracks spatial distribution such as shown in Fig. II .26, these exists a significantly trend that, the number of micro-cracks with low inclination angle induced by shear sliding increase with the increase of intermediate (σ_2). However, this effect will gradually be sable when the difference between two lateral stresses $(\sigma_2 - \sigma_3)$ is large enough, such as shown in Fig. II .27.

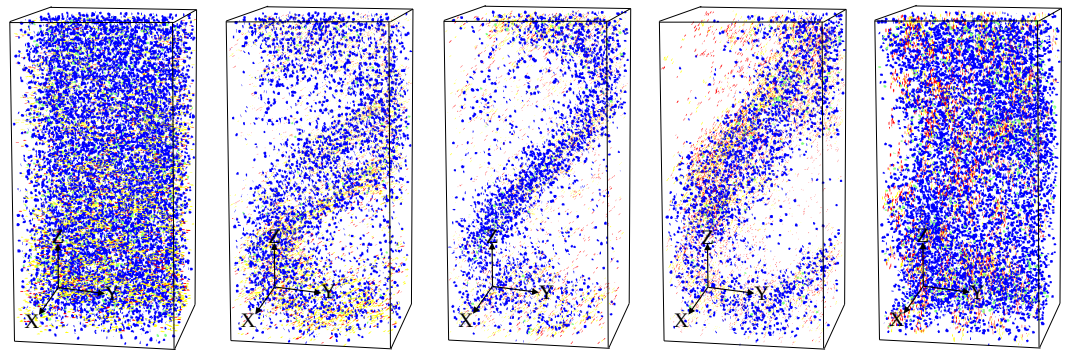

(a) $\sigma_2 = 20MPa$

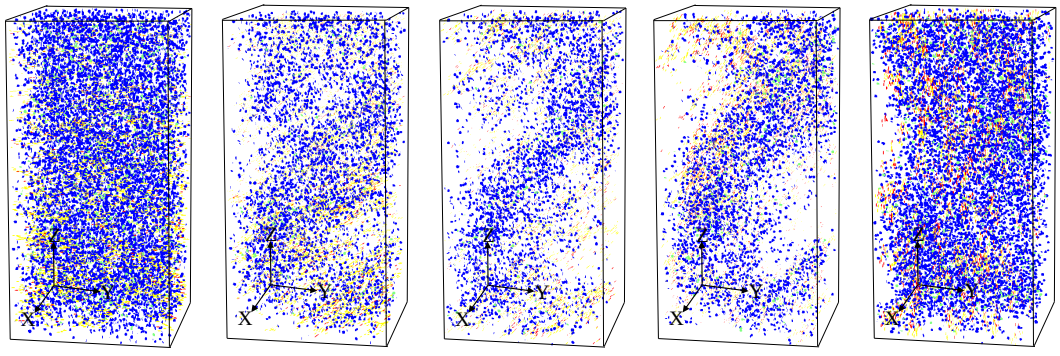

(b) $\sigma_2 = 40MPa$

Figure II .25: Spatial distribution of micro cracks for different bond models after failure in specimens with various orientations

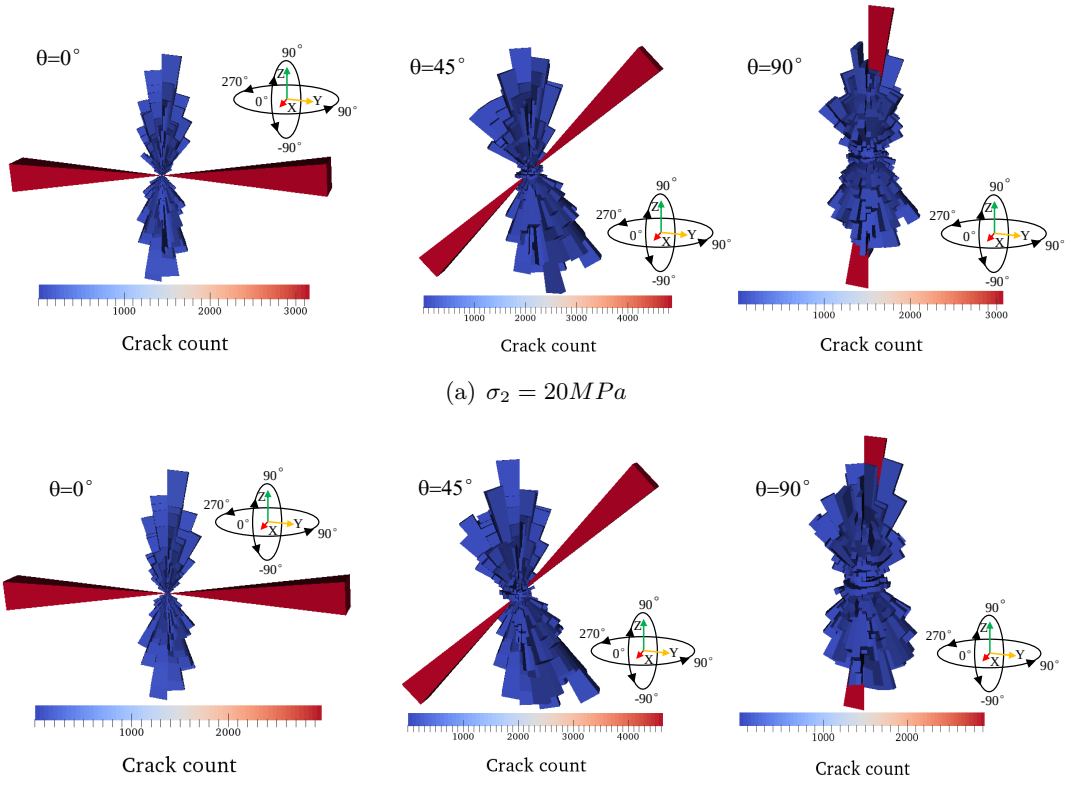

(a) $\sigma_2 = 20MPa$

(b) $\sigma_2 = 40MPa$

Figure II .26: Statistics for spatial angle distribution of micro-cracks after failure in samples with various orientations

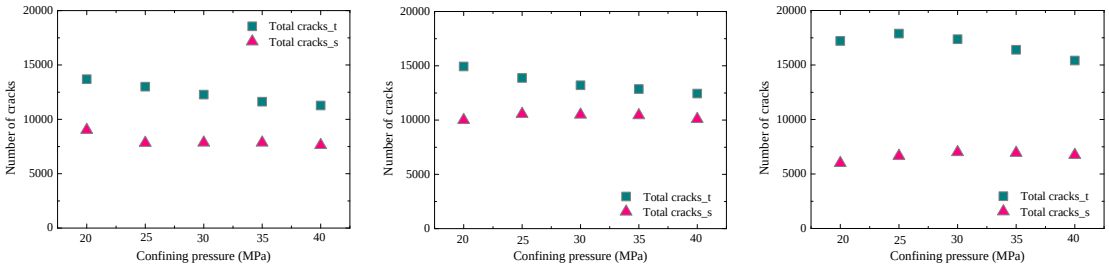

(a) $\theta = 0°$ (b) $\theta = 45°$ (c) $\theta = 90°$

Figure II .27: Total of micro-cracks evolution after failure in samples with various orientations under compression with intermediate stresses σ_2 (red: tensile failure, green: shear failure)

Moreover, the displacement of anisotropic samples after failure have also analyzed such as Fig. II .28. It seems that, the increase of difference of two lateral stresses $(\sigma_2 - \sigma_3)$,

has slightly effect on the failure band distribution and inclination when the orientation of weakness layer is in range $30° \leq \theta \leq 60°$. In other cases, especially for orientation equal to $0°$ and $90°$, there is an obvious failure band gradually formed in anisotropic sample with increase of intermediate principal stresses σ_2.

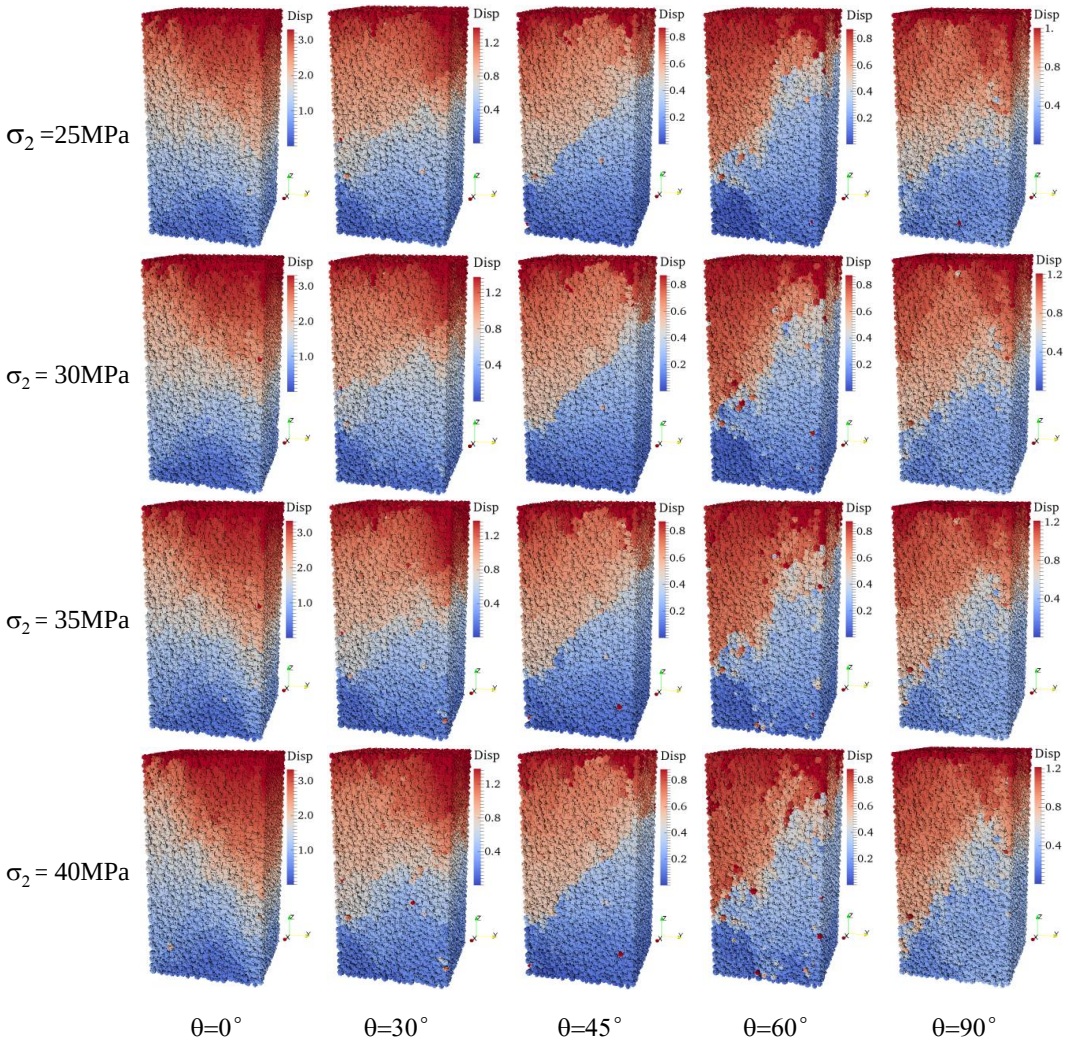

Figure II .28: Displacement fields in specimens with various orientations under compression with different intermediate stress σ_2

7 Conclusion

In this paper, mechanical strength and deformation of inherent anisotropic materials have been investigated using the three-dimensional DEM with two contact bond models: a new bond model and smooth joint model. For this purpose, a algorithm that introduces

smooth joint model into anisotropic samples have been first proposed to capture the specific micro-structure of anisotropic material. Science the macro deformation and failure behavior is controlled by local elastic stiffness and strength failure criteria, these corresponding parameters in two contact bond models have also been developed depending on the interface orientation, respectively. Then, a detailed calibration and verification procedure of the developed parameters have also been conducted. Furthermore, the proposed procedure has been applied to modelling the mechanical behavior of a typical anisotropic rock, there is a good agreement between numerical results and experimental data for both elastic properties and mechanical strength. The numerical results have further shown that, the inherent properties of weakness layer as well as confining pressure both have significantly influenced on macro anisotropic mechanical behaviors of anisotropic materials. Its failure process is controlled by the weakness layer properties for low confining pressure, but depended on the combination role of weakness layer and rock matrix properties under high confining pressure. In addition, the influence of the intermediate principal stress on the strength and deformation has been investigated. It is found that, with the intermediate stress increase, the increase magnitude of macro strength will decrease and its failure model has a clear transition to a shear failure. However, the macro strength and deformation of anisotropic cohesive materials is also strongly influenced by interstitial fluid, thus the hydro mechanical coupling by considering fluid flow through interface and discrete fracture should be still investigated in the future studies.

Chapter III

Analysis for fluid-driven fracture propagation in hard rock using the discrete element method

Contents

1 Introduction

Hydraulic fracturing is a common issue that extensively exist in the petroleum and gas industry. It is generally defined as the process that a fracture is initiated and propagated due to hydraulic loading applied by fluid inside the fracture. In order to have deep sight on hydraulic fracture propagation and to improve the productivity of oil and gas, a great number of researchers tried to solve this challenges by adopting their familiar methods, such as analytical methods, laboratory experiments or numerical simulations.

In analytical studies, researchers endeavour to capture the physics of hydraulic fracture by applying mathematical models derived according to physical laws. Because of complexity of the problem, especially for porous heterogeneous formation in a dynamic condition, these models is either hard to derive or too complex to apply. Thus, large number of simplification solutions are obtained by considering rock matrix as homogenous elastic medium in a static scenario. For instance, [Thiercelin et al., 2007], [Thiercelin et al., 2007] have proposed a semi-analytical model based on the theory of dislocations to predict the reactivation of a natural fault due to the presence of an approaching hydraulic fracture. [Gu et al., 2010] have extended the Renshaw and Pollard criterion for orthogonal intersections to a fracture crossing frictional interfaces at non-orthogonal angles. However, the initiation and propagation of hydraulic fracture is a dynamic process that changes the state of stress within the rock as the fracture propagates.

Therefore, experiments are thought to be a better method, which can consider the effect of different parameters on the interaction mechanism of hydraulic fracture under real situation ([Zhou et al., 2008]; [Gu et al., 2010], [Gu et al., 2012]; [Sarmadivaleh and Rasouli, 2015]; [Chen et al., 2015]; [Yushi et al., 2016a]; [Fatahi et al., 2017]; [Ma et al., 2017b]; [He et al., 2018]). However, these small-scale experiments are not only expensive but also extremely tedious and time consuming. It is hardly ensure the obtained results suitably applied in field operations due to itself scale, especially for routine industry application. These draws further put constraint on the number of sensitively analysis that can be conducted and subsequent conclusion that can be drawn.

In the aforementioned methods, most of them are mainly focused on the result analysis of failure sample, neglecting hydraulic fracturing process. However, even in the basic form of hydraulic fracture, there are at least three processes should be taken into account, respectively as, mechanical deformation induced by the fluid pressure, the flow of fluid in the fracture and fracture propagation. The main issue is to capture the physical developing processes of hydraulic fracture at microscopic scale, For this purpose and with the fast progress of computing technology, large number of numerical simulation methods have

been modified and applied. For instance and without giving an exhaustive list of reported studies, the Finite Element Method (FEM), the Boundary Element Method (BEM) as well as the Extended Finite Element Method (EFEM) was first adopted to simulate hydraulic fracture in complex structure ([Munjiza et al., 1995]; [DU et al., 2008]; [Olson et al., 2008]; [Olson et al., 2009]; [Zhang et al., 2010]; [Dahi-Taleghani et al., 2011], [Dahi Taleghani et al., 2013]; [Zeng and Yao, 2016], [Zeng et al., 2018]). In the framework of continuum mechanics, these methods provide efficient numerical tools for modeling hydraulic fracture growth. However, considering fracture propagation mainly controlled by the stress singularity at fracture tip, it is actually not an easy task to define appropriate criteria to determine the onset condition and propagation direction of fracture.

Different with these continuum methods, various discrete elements methods that replace a continuum medium by an equivalent discrete medium have made a great progress during the last decades. Without giving an exhaustive list of different approaches, two main families of discrete media have been generally adopted, a set of polygon blocks for polycrystal structure and an assembly of spherical grains for granular morphology. Both two approaches have capable of handling coupled hydraulic-mechanical processes through a defined fracture network. However, unlike in the first DEM method, such as UDEC, 3DUC and Rigid Block Spring Method ([Nasehi and Mortazavi, 2013]; [Hamidi and Mortazavi, 2014]; [Yushi et al., 2016b], [Zou et al., 2016]; [Ma et al., 2017a]; [Nagel et al., 2013]), fluid movement is restricted to fracture flow model that fluid flow into the joint occurs when a joint is broken. The second DEM method like PFC2D allows not only fluid flow through fractures, but also fluid leak-off into the rock matrix. The fluid flowing is more similar to a natural process that depends on whether a fluid pressure difference exists between neighboring pores. Therefore, in a certain degree, it has been successfully used to simulate hydraulic fracture process ([Al-Busaidi et al., 2005]; [Shimizu et al., 2011]; [Zhou et al., 2017a]; [Zhang et al., 2017]). However, in the most of studies, the simple fluid flowing are mainly focused on, rather than analyze the effects between fluid flow and hydraulic fracture. And because of existing defects for the original code in PFC2D, these researches generally only presented failure results without giving the variation of injection bole pressure as well as fluid pressure distribution, which is also important to investigate hydraulic fracture initiation and propagation ([Reinicke et al., 2010]; [Eshiet et al., 2013]; [Wang et al., 2014]; [Fatahi et al., 2017]; [Zhao and Paul Young, 2011]; [Wang et al., 2017]).

Therefore, in this study, for solving the drawback in original algorithm that the channel connecting two adjacent reservoirs vanishes when the contact between two particles

broken occurs, we first proposed a modified fluid-mechanical algorithm based on PFC2D for simulating hydraulic fracture. Then, with a calibration procedure, a specific hydraulic fracturing process is studied on and the method applicability is also validated by comparing analytical solution of the breakdown pressure and numerical results. Finally, a series of investigations on different confining pressure, fluid viscosity and injection rate are further analyzed using the modified method.

2 Simulation methodology

In fluid coupling analysis of cohesive materials, the macroscopic strength, deformation as well as failure propagation are essentially controlled by the local behavior of intergranular interfaces. By introducing bonds between circular particles, the PFC2D based on discrete element method can be applied to analysis these mechanical behaviors under the case of fluid coupling, in which these materials are modelled as a composite of individual particles that can move and rotate with respect to each other. Thorough details of fundamental DEM algorithm have been presented in large number of literatures ([Cundall, 2004]; [Potyondy and Cundall, 2004]; [Cundall, 2008]), only a brief introduction will be given here.

2.1 Formulation of mechanics of bonded particles

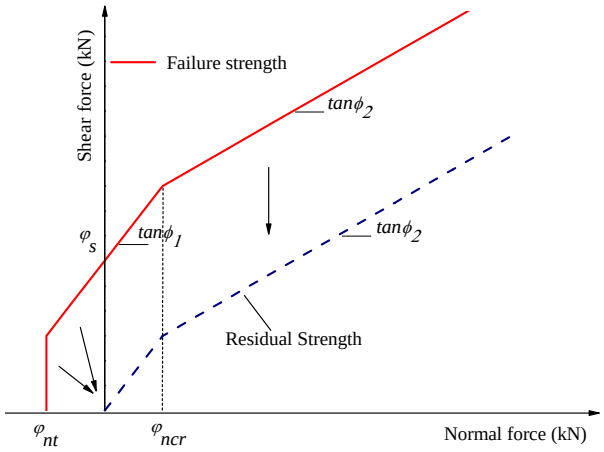

Figure III .1: Peak and residual strength envelopes of bonded contact model

Two types of bond models of interface, i.e. the contact bond model (CBM) and parallel bond model (PBM), are generally adopted for analyzing cohesive materials in PFC. Due to the shortcoming of these criterions that the effect of normal stress on the shear strength

cannot be correctly described for a large range of normal stress. Therefore, a new proposed bond model with bi-liner failure criterion as illustrated in Fig. III .1 will be adopted in this reach. Here, we just give a brief introduction, more detailed explanations can be found in our other research ([Zhang et al., 2018b]). For this bond model, in calculation of local contact force at contacts, the normal force F_n and the increments of tangential force ΔF_s can be calculated from the relative motion of bonded particles, and given as follows:

$$F_n = k_n u_n \tag{III .1}$$

$$\Delta F_s = -k_s \Delta u_s \tag{III .2}$$

where, k_n and u_n are respectively the normal stiffness and displacement at the contact ; k_s and Δu_s, respectively, denote the shear stiffness and relative displacements in each time step Δt. Note that the normal stiffness, k_n, is a secant modulus that relates to the total displacement and force. The shear stiffness, k_s, on the other hand, is a tangent modulus that relates to the incremental displacement and force.

2.2 Fluid-mechanical coupling theory

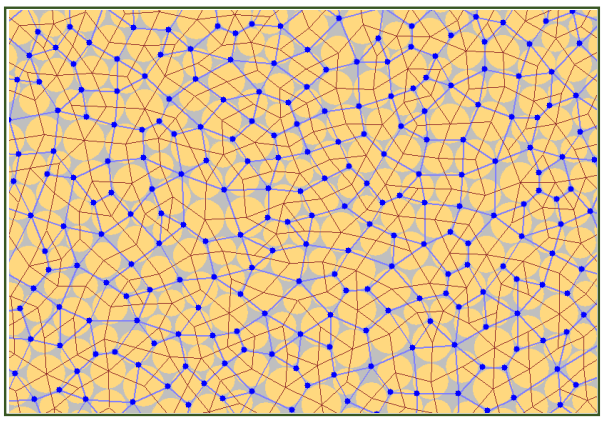

Figure III .2: Fluid network: solid particles (yellow circles), flow channels (blue lines), domains (red polygons) and domain's centers (blue points).

The coupling mechanism of the stress filed and the seepage field in a jointed rock analyzed with PFC2D was firstly proposed by [Cundall, 2004], then developed by many other authors (without giving an exhaustive list). The original concept of this method is based on the network flow model, which is mainly composed with two components: the flow channel (pipe) and domains (reservoirs). Such as Fig. III .2 and Fig. III .3(a)

shows, each contact between particles is first regarded as a flow channel, whose length is equal to summation of the two particle radii at the contact. Afterwards, the red lines connecting the centers of all particles at contacts create a series of enclosed domains, their centers (Fig. III .2, blue points) are stored as reservoirs. each reservoir are contacted by the corresponding pipes (Fig. III .2, blue lines). Therefore, each domain is completely surrounded by flow channels and has a certain volume associated with it.

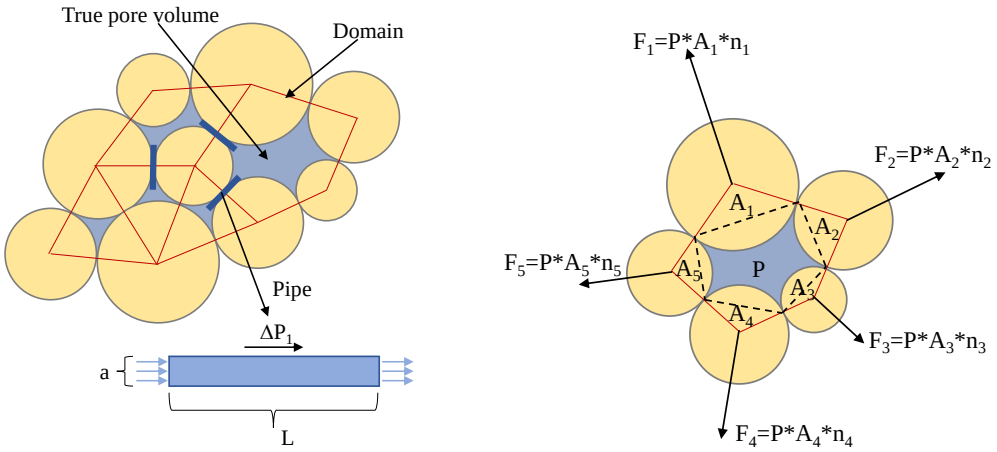

(a) Domains and flow path (b) Mechanical coupling

Figure III .3: Hydraulic coupling mechanism in a bond assembly of particles

As shown in Fig. III .2 and Fig. III .3(a), differential pressure between two neighboring domains generally induces the fluid flow in its corresponding channel, each channel is assumed to be a set of parallel plates with a certain aperture as e, and the flow in the channel is modelled as laminar. Therefore, the fluid flow can be calculated using the Poiseuille Equation, and the volumetric laminar-flow rate q is given as the following equation:

$$q = \frac{e^3 \Delta p}{12 \mu L_p} \tag{III .3}$$

Where e is the hydraulic aperture, L_p is the length of the flow channel, Δp is the fluid pressure difference between the two neighboring reservoir domains, and μ is the fluid dynamic viscosity. The out-of-plane thickness is assumed to be of unit length.

Resulting from flow rate q of channel changing in each time step Δt, the increments of fluid pressure Δp of corresponding domain will also response and can be calculated by application of the continuity equation Eq.(III .4), respectively from the bulk modulus of fluid K_f, the volume of the domain V_d, the sum of the flow volume for one time step

$\sum q\Delta t$, and the volume change of the domain ΔV_d.

$$\Delta p = \frac{K_f}{V_d}(\sum q\Delta t - \Delta V_d) \tag{III .4}$$

At each time step, the mechanical computation updated induce the geometry change of the system that each domain gathers the fluid pressure of the surrounding channels and then acts on the surfaces of the surrounding particles as equivalent body force, such as shown in Fig. III .3(b).

Furthermore, the new updated contact force will be used for verification of bond state between particles. If the bond is not failure, it will produces new aperture values for channel and then determines renew volume value for domain. Otherwise, once bond failure, fluid flow occurs instantaneous, and fluid pressure in the adjacent domains will recalculate. In order to simplify this process, the updated fluid pressure of two domains is regard as equal to their average value, which have been generally accepted in other studies ([Hazzard et al., 2002]; [Al-Busaidi et al., 2005]; [Zhao and Paul Young, 2011]). Its corresponding calculation is given as the following Eq.(III .5).

$$p'_f = \frac{p_{f1} + p_{f2}}{2} \tag{III .5}$$

2.3 Crack-growth theory in fluid coupling process

In failure analysis of interfaces, there are two debonding processes that should be taken into account, i.e. the tensile failure and shear sliding, which is determined by comparing the calculated local contact force and bond strength at a contact. For tensile cracking, the failure condition is generally dependent on the normal contact force. While the frictional sliding process is otherwise more complex, depending on both normal stress and tangential shear stress([Zhang et al., 2018b]).

Therefore, such as the bi-linear failure criterion illustrated in Fig. III .1. the tensile failure occurs when the normal contact force $F_{t,f}$ exceeds the normal strength φ_{nt}. For the shear sliding, the shear strength of interfaces is here approximated by a bi-linear function of normal contact force. When the normal contact force is less than the transition threshold φ_{ncr}, the shear strength is defined by the cohesion φ_s and frictional angle ϕ_1. When the normal force is higher than φ_{ncr}, a second frictional angle ϕ_2 is introduced with $\phi_2 < \phi_1$ to define the shear strength. The failure criterion for contact interface is then expressed in the following form:

$$F_{t,f} = \varphi_{nt}, \text{tensilefailure} \tag{III .6}$$

$$F_{s,f} = \begin{cases} 0 & ,F_n < \varphi_{nt} \\ \varphi_s + F_n \tan\phi_1 & ,\varphi_{nt} \leq F_n \leq \varphi_{ncr} \\ \varphi_s + \varphi_{ncr}(\tan\phi_1 - \tan\phi_2) + F_n \tan\phi_2 & ,F_n \geq \varphi_{ncr} \end{cases} \text{, shearfailure} \tag{III .7}$$

When the contact surface is broken, the tensile strength immediately drops zero. However, due to the frictional force along rough interfaces, the shear strength reduces to a residual value that is a function of the normal stress and the coefficient of friction acting on the contact surface. The residual strength envelop is shown in Fig. III .1 and the following criterion is formulated:

$$F_{s,r} = \begin{cases} 0 & ,F_n \leq 0 \\ F_n \tan\phi_1 & ,0 < F_n \leq \varphi_{ncr} \\ \varphi_{ncr}(\tan\phi_1 - \tan\phi_2) + F_n \tan\phi_2 & ,F_n > \varphi_{ncr} \end{cases} \tag{III .8}$$

3 Simulation and validation

The generation process of hydraulic fracturing sample as well as calibration of bonded model are presented in this section. Furthermore, the detailed description and validation for the generated rock sample have also been conducted to investigate the micro cracks propagation in numerical sample under different confining pressure conditions.

3.1 Determination of micro-mechanical parameters

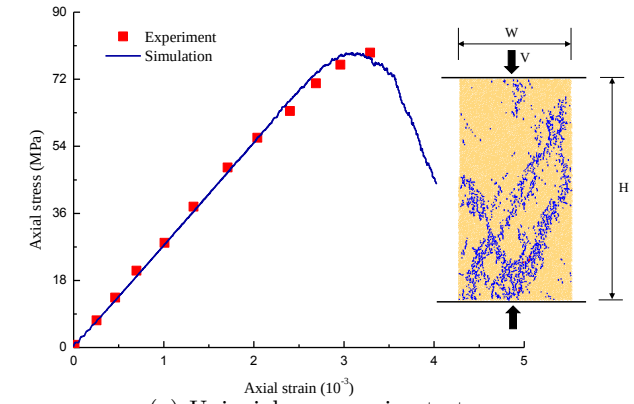

(a) Uniaxial compression test

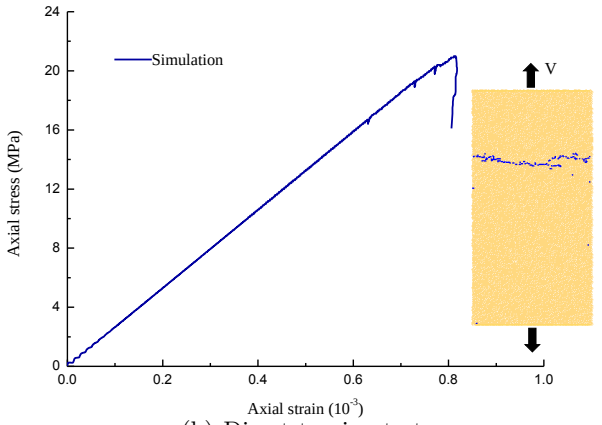

(b) Direct tension test

Figure III .4: Mechanical parameter calibration results and corresponding failure sample (blue lines indicate tensile cracks)

The proper selection of meso-mechanical parameters is the fundamental task for simulation using PFC ([Shi et al., 2013]; [Zhang et al., 2018a]). Based on the correlation between the macro-mechanical property of the particle assembly and the meso-mechanical parameters of a particle such as Eq.(III .9) and Eq.(III .10), these values for particles can be determined by conducting a series of numerical simulations of physical mechanics. Therefore, as shown in Fig. III .4(a) and Fig. III .4(b), the uniaxial compression test and direct tension test were respectively conducted on a sample of 150mm in width and 300mm in height to determine two types of mico-scopic parameters: the deformability and strength. The number of particles in sample is about 10000 with average radii R of 1.33mm following a normal distribution. The porosity of sample is 0.15. And the ratio of

the largest radius to the smallest radius is 1.66.

$$k_n = 4E_cR, k_s = k_r k_n \tag{III .9}$$

$$\varphi_{nt} = 4\sigma_c R^2, \varphi_s = 4\tau_c R^2 \tag{III .10}$$

In the uniaxial compression test, the above and below walls of sample were moved slowly at a small velocity to simulate experimental loading, and the axial stresses of the walls and the axial and lateral strains were monitored at the same time. Hardly to conduct the direct tension test of indoor test due to the rock mass structural characterizes, it can be also realized by applying the loading on the above and below row of particles of sample in the simulations. Then, by adopting a numerical optimal procedure, a set of model's parameters is given in Table 1, and the corresponding simulation results of sample is shown in Fig. III .4.

Table III .1: Mechanical parameters for bond model used in hydraulic fracture simulations of experimental tests

Mechanical parameters for new bond model			
Normal contact stiffness for test (N/m)	k_n		$7.6 * 10^8$
Shear contact stiffness for test (N/m)	k_s		$5.1 * 10^8$
Inter-particle coefficient of friction	$tan\phi_1$		1.5
Inter-particle coefficient of friction	$tan\phi_2$		0.5
Normal bond strength (N)	φ_{nt}		$6.7 * 10^4$
Shear bond strength (N)	φ_s		$2.1 * 10^5$
The critical normal stress (N)	φ_{ncr}		$4.2 * 10^5$
Calibration results		**Experiment**	**Simulation**
UCS of rock model (MPa) (m^2)	σ_c	79	78.6
Tensile strength (MPa)	σ_t	-	20.3
Young's modulus (GPa)	E	27	26.8
Poisson's ratio	μ	0.2	0.21

3.2 Rock sample model and loading condition

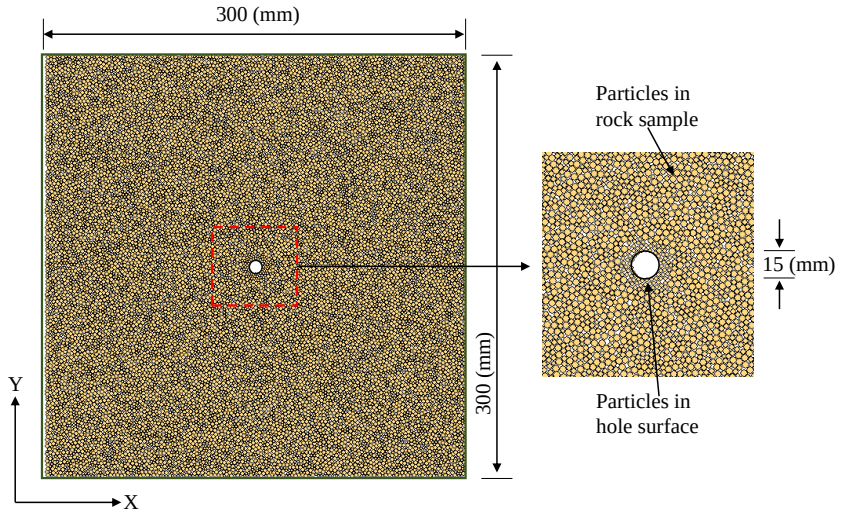

Figure III .5: Geometrical description for rock sample

As shown in Fig. III .5, the sample used in hydraulic fracturing simulation is generated according to the experimental test, which is performed in Australia by [Sarmadivaleh and Rasouli, 2015]. It is 300mm in width and 300mm in height with 20000 particles, for avoiding particle size distribution effect ([Zhang et al., 2018b]), the size of particles filling in hydraulic fracturing sample has the same distribution as in uniaxial compression test and direct tension test. In order to create a smoothed surface simulating for viscous fluid injection, a hole with a diameter of 15mm is also created at the center of sample by the smallest particle radii of 1mm illustrated in Fig. III .5. This approach can effectively avoid particle size change effect on mechanical property of injection hole. The sample is surrounded by four walls that can move to apply the constant confining pressure with σ_1 in the x-direction and σ_3 in the y-direction. Between the walls (green ones) and domain region (blue square), there exists some particles (yellow ones) not covered by fluid flow domains, which can be regarded as an impermeable rubber housing such as shown in Fig. III .6.

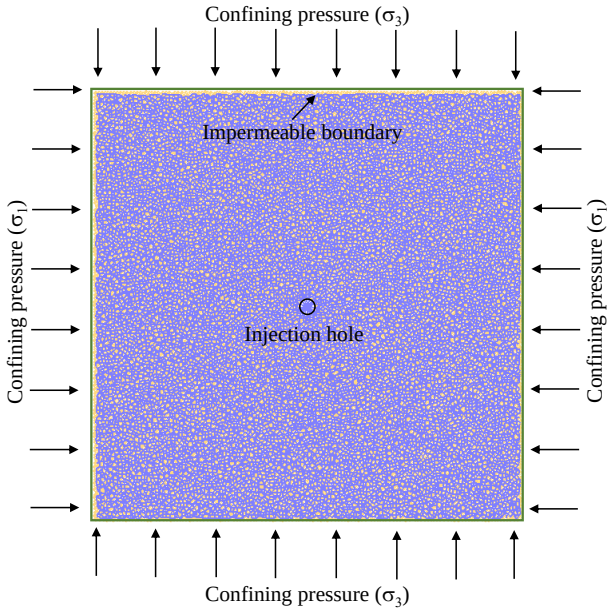

Figure III .6: Fluid flow domain, impermeable boundary and loading condition

In the calibration of fluid network of hydraulic fracturing sample, the critical issue is to determinate the channel aperture connecting these reservoirs. Accounting for the existence of a limiting residual aperture that is always observed in laboratory rock samples, in this present work, a initial aperture is firstly assumed at the contact for the just touching particles, it allows fluid to flow even without normal contact force. While contact force between particles exists, a function of the hydraulic aperture of the flow channel against normal force is given as the following equation ([Al-Busaidi et al., 2005]; [Zhou et al., 2017a]):

$$e = e_{res} + (e_{ini} - e_{res}) \exp(-\alpha \sigma_n) \tag{III .11}$$

Where, e_{ini} and e_{res} denote the initial and residual aperture of channel respectively, α is the model parameter taking 0.15 in this research, σ_n is the effective normal force at the contact. When it trends to infinity, the aperture decreases asymptotically to e_{res}.

Due to the fluid flow rate q calculation aforementioned in Eq.(III .3) of section 2.2 focused on one microscopic flow channel between particles, the permeability of the entire rock sample cannot be directly used for the fluid flow of numerical sample, which is expressed by an assembly of many flow channels. This problem can be solved by setting reasonable values for initial and residual apertures e_{res} and e_{ini} in hydraulic fracturing sample. Generally, these values can be determined by two methods: calculating with the permeability k of the real rock specimen or directly simulating the permeability test corresponding to the characteristics of an actual sample. In this research, we take the first

direct calculation method to identify these values by the Eq.(III .12).

$$k = \frac{1}{12V} \sum_{pipes} Le^3 \tag{III .12}$$

Where V is the volume of the reservoir rock, L is the length of the channel or pipe.

Table III .2: Geometrical and physical parameters for network used in hydraulic fracture simulations of experimental tests

2D Sample (see Fig. III .5)			
Width of sample (m)	W		$3.0 * 10^{-1}$
Height of sample (m)	H		$3.0 * 10^{-1}$
Injection bore diameter (m)	H		$1.5 * 10^{-2}$
Total grain number in sample			20000
Lower bound of particle radius (m)	R_{min}		$1.0 * 10^{-3}$
Ratio of particle radius	$R_{\max}/R_{\min}$		1.66
Initial void ratio	R_{min}		0.20
Physical parameters for fluid network			
Initial hydraulic aperture (m)	e_{ini}		$1.5 * 10^{-6}$
Residual hydraulic aperture (m)	e_{res}		$0.5 * 10^{-6}$
Bulk modulus of the fracturing fluid (GPa)	K_f		2.0
Calibration results		**Experiment**	**Simulation**
Permeability (m^2)	k	$1 * 10^{-17}$	$1 * 10^{-17}$

3.3 Description for hydraulic fracturing process

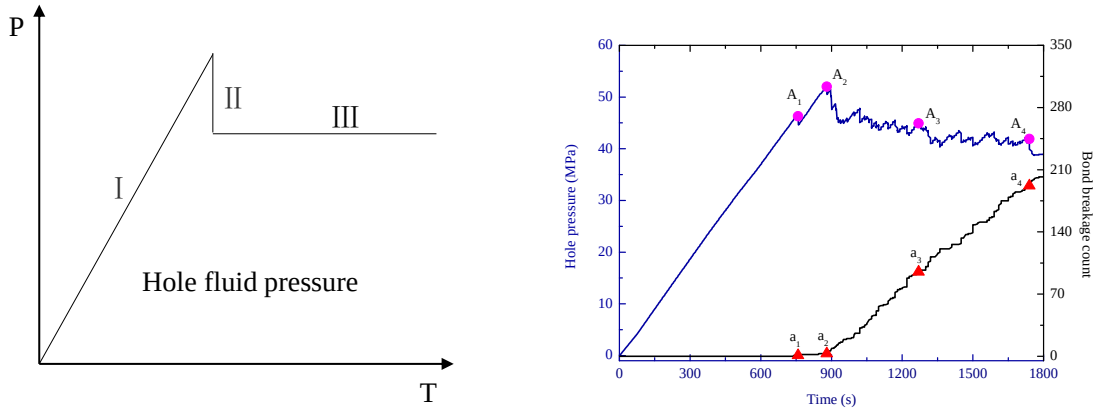

(a) Common fluid pressure response

(b) Simulation result

Figure III .7: Comparison of fluid pressure response between common result and simulation value

By adopting a numerical optimal procedure, a set of model's parameters is defined and given in Table 1 and 2, respectively. Taking injection rate and fluid viscosity as $1.0 * 10^{-5} m^3/s$ and $1.0 * 10^{-3} Pa/s$, the simulation of hydraulic fracturing process has been first performed on generated sample with those parameters under the same confining pressure, such as σ_1 =20MPa and σ_3 =20MPa. Then, numerical results were further compared with general analytical fluid pressure response presented in Fig. III .7. A similar changing tendency is obtained that, with the increase of injection fluid, the curve of fluid pressure of injection hole has three obvious change stage: (1) pressure increasing to largest value stage (I in Fig. III .7(a), $o - \alpha_1 - \alpha_2$ in Fig. III .7(b)), (2) after breakdown, pressure decreasing stage (II in Fig. III .7(a), α_2 in Fig III .7(b)) and (3) pressure fluctuation stage (III in Fig. III .7(a), $\alpha_3 - \alpha_4$ in Fig. III .7(b)). Unfortunately, due to the technical limit of experimental device, the failure process of hydraulic fracturing sample can not be vivid presented in the laboratory tests and further limits the study of failure mechanism. However, according to the numerical results obtained, one can see a clear failure development in hydraulic fracturing sample, such as micro-cracks propagation, pressure field and the forming mechanism of micro-cracks.

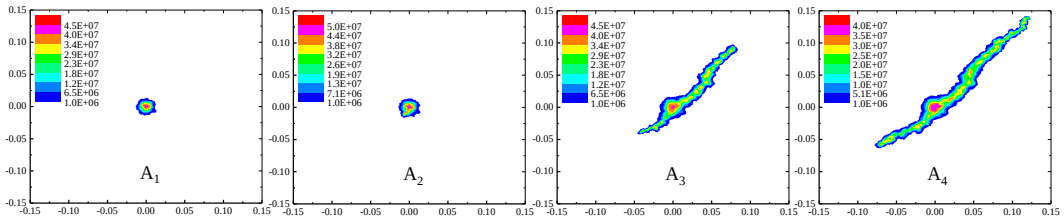

(a) Crack propagation

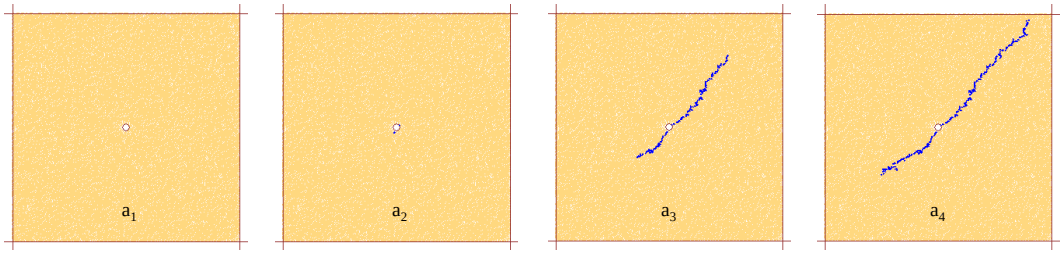

(b) Pressure field

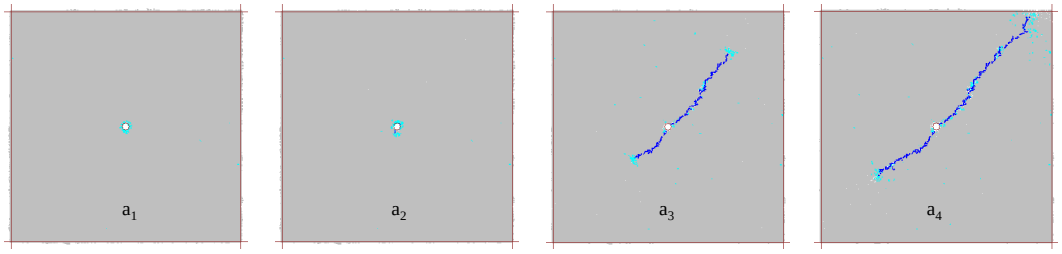

(c) Contact force distribution

Figure III .8: Pressure field, crack propagation and corresponding contact force distribution for failure sample under same confining pressure ($\sigma_1 : \sigma_3 = 20 : 20$)

Thus, it can be seem from numerical results that, with the increase of fluid pressure, a single micro-crack is first developed surrounding the injection hole as shown in Fig. III .8(a) and leads to fluid pressure decrease slightly presented as α_1 in Fig. III .7(b). However, since single non-through micro-crack that has limited capacity for fluid migration can not cause the significant change of fluid pressure, the fluid pressure is still increase. Because of continuous increment, new micro-cracks will form and further develop to be a through hydraulic fracture as shown in Fig. III .8(a). Then, the value of fluid pressure decrease significantly at a_2 point in Fig. III .7(b). After that, with hydraulic failure propagating in sample as shown in Fig. III .8(a), the fluid pressure of injection hole has a fluctuate tendency $\alpha_3 - \alpha_4$ in Fig. III .7(b)). This analysis can be also verified and sustained by the distribution of fluid pressure and contact force, respectively in Fig. III .8(b)) and Fig. III .8(c)). Especially for contact force distribution, there is an obvious tensile force

concentration distributing at both ends of the hydraulic fracture, which further interpreters that the formation mechanism of micro-cracks in hydraulic fracturing sample is often caused by tensile force.

3.4 Validation of hydraulic fracturing model

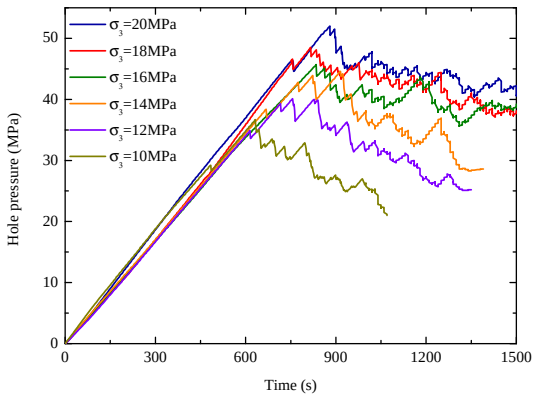

Figure III .9: Different fluid pressure responses of injection hole under different confining pressure: σ_1 keeping 20 MPa and σ_3 ranging from 20MPa to 10 MPa

In order to further validate the reliability of hydraulic fracturing simulation using the new proposed bond model, a series of simulations on samples with same parameters have also been preformed with different confining pressure, such as σ_1 keeping 20MPa in x-direction and σ_3 changing from 20MPa to 10MPa in y-direction. It can be obtained form the numerical results in Fig. III .9 that, with the increase of differential pressure, the breakdown pressure as well as the duration of cracks propagation for the same sample both have a gradually decrease tendency, which is also found in many experimental studies. The breakdown pressure have further compared to the theoretical values calculated according to Eq.(III .13), which is proposed from the classical Kirsch equations for stress concentration around a circular elastic hole, by ([Haimson and Cornet, 2003]; [Fairhurst, 2003]; [Wang et al., 2014]).

$$\mathrm{p_b} = \sigma_t - \sigma_1 + 3\sigma_3 - p_0 \tag{III .13}$$

As shown in Fig. III .10, there is an acceptable error between the simulation results and idealized analytical value, which is less than 0.15 when the confining pressure σ_3 changes from 20MPa to 10MPa in y-direction.

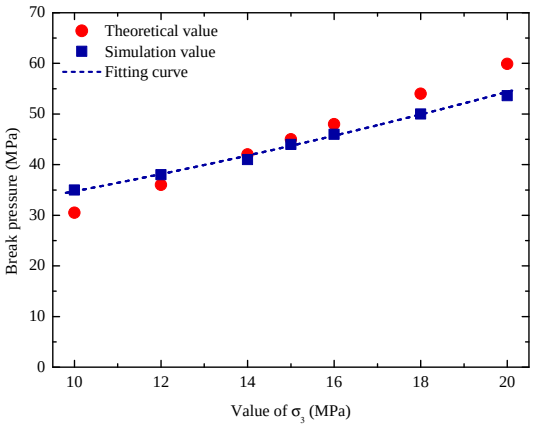

Figure III .10: Breakdown pressure comparisons between numerical results and theoretical calculations obtained according to Eq.(III .13)

4 Numerical results and discussions

The performance of hydraulic fracturing is not only related to mechanical properties of rock sample, but also influenced by the differential confining pressure, the injection flow rate, and the viscosity of the fluid. Thus, by adopting the suitability hydraulic fracturing model verified in section 3.4, a comprehensive series of numerical simulations respecting fluid injection into rock sample have been conducted to investigate these factors effect on hydraulic fracture, such as propagation direction, developing quantity and the influencing space.

4.1 The influence of confining pressure

Using the verified hydraulic fracture model, with rock mechanical parameters and fluid network parameters unchanged, the differential pressure effect on hydraulic fracture is first investigated by keeping σ_1=20MPa in x-direction and changing σ_3 from 20MPa to 10MPa in y-direction. Since this effects have been partly discussed in section 3.4, especially for fluid breakdown pressure. Therefore, in this section, we focus on the developing process of hydraulic crack as well as fluid pressure distribution surrounding fractures.

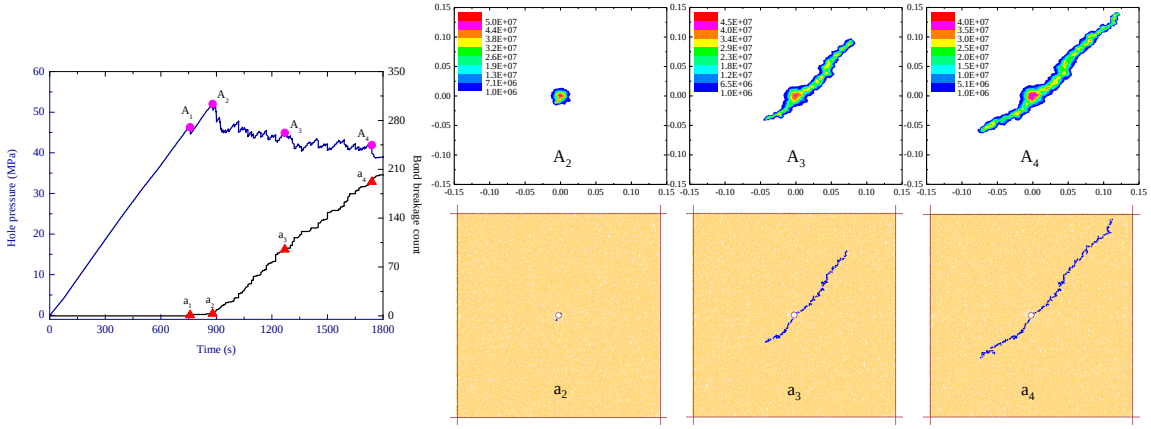

(a) $\sigma_1 : \sigma_3 = 20 : 20$

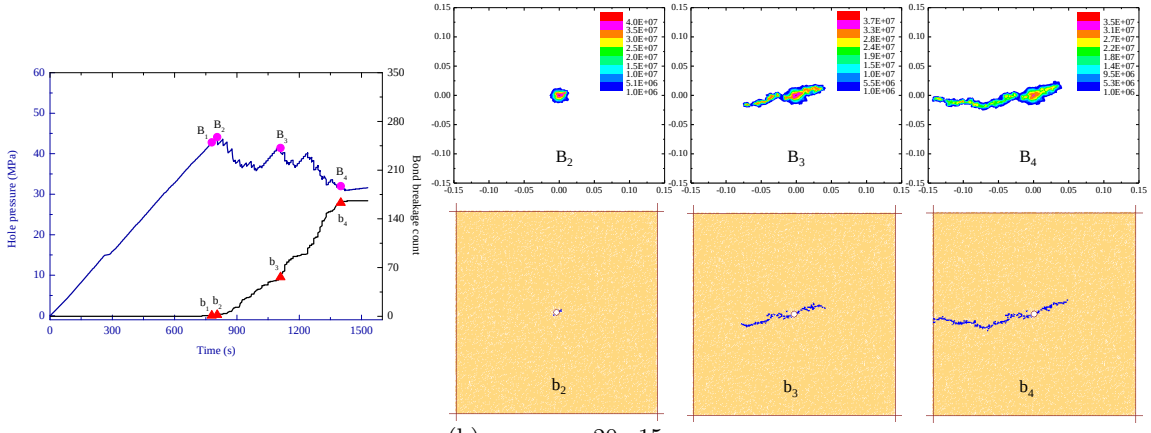

(b) $\sigma_1 : \sigma_3 = 20 : 15$

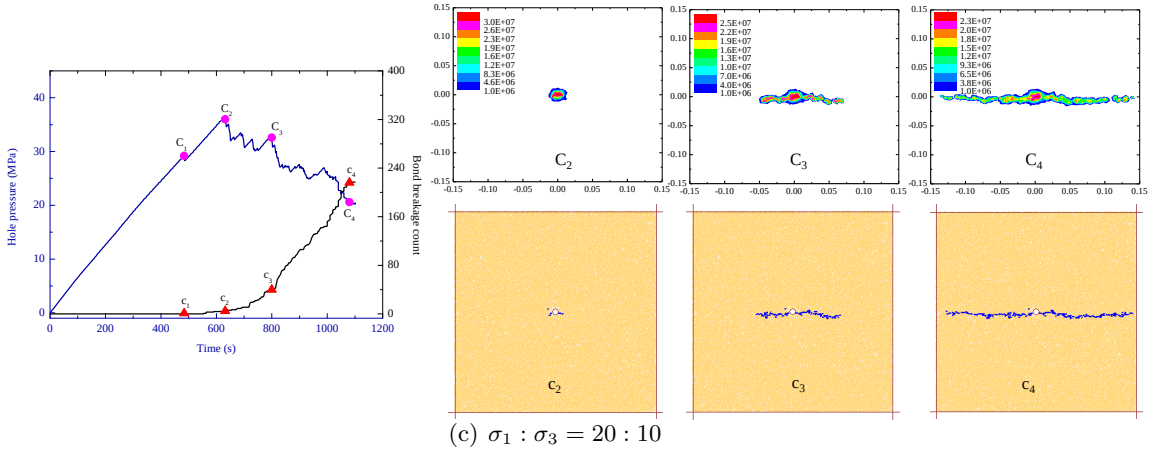

(c) $\sigma_1 : \sigma_3 = 20 : 10$

Figure III .11: Pressure histories of injection hole, fluid field and crack propagation in hydraulic fracturing with an injection rate of $1.0 * 10^{-3}\ m^3/s$ under different confining pressure

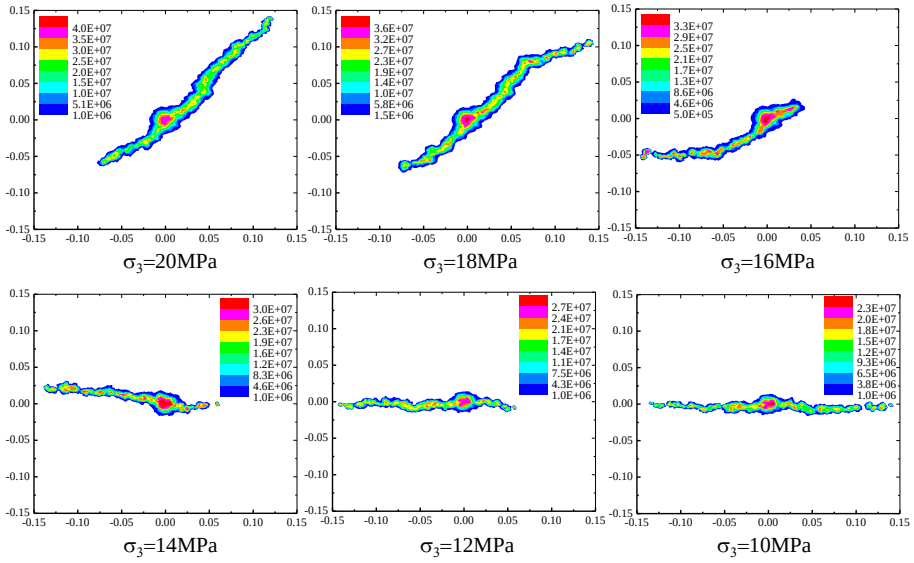

(a) pressure field

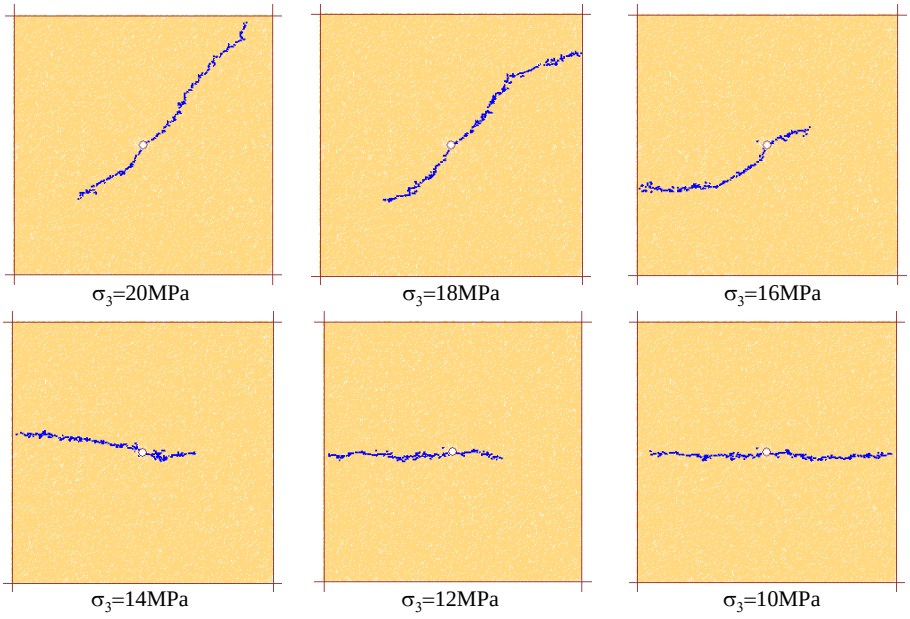

(b) Crack propagation

Figure III .12: Description of pressure field and crack propagation changing with different confining pressure

Such as shown in Fig. III .11(a), three representative hydraulic fracturing simulations are presented with the stress ratios $\sigma_1 : \sigma_3$ of 20 : 20, 20 : 15 and 20 : 10. The results show that, the breakdown pressure decrease with the increase of differential pressure, respectively as 53.2MPa, 43.1MPa and 34.9MPa. The injection duration time, no matter

before breakdown pressure or during the crack propagation stage, has the same change tendency.

Generally, for the hydraulic fracture development, the major fracture will firstly form and develop in a preferred direction, which is depended on the combination action of stress state and initial model formation. Due to most of micro-cracks induced by tensile failure, when differential pressure is main factor such as confining pressure $\sigma_1 : \sigma_3 = 20 : 15$ and $\sigma_1 : \sigma_3 = 20 : 10$, tensile stress distinct concentration leads the micro-crack to initially form and develop along the direction of maximum confining pressure, clearly illustrated in Fig. III .11(b) and Fig. III .11(c). Comparatively, under hydraulic pressure condition, the formation and propagation is depended on the defect surrounding injection hole of sample.

The fluid pressure distributions also provide supplement for the crack development mechanism. The fluid pressure in the injecting hole and the available space can drive crack growth. At the same time, due to crack development and deformation of reservoir, the pore-pressure also changes. Fig. III .12(a) and Fig. III .12(b) show that the distribution of fractures is corresponding to the pore pressure field. It should be worthy noted that, the crack development in this research is random and non-symmetric process that is completely controlled by the stress state, different to some studies that the cracks developed symmetrically. There is also an interesting phenomena can be found that, with the increase of differential pressure, the direction of crack propagation as well as fluid pressure distribution both gradually change close to the horizontal orientation, which is the direction of maximum principal stress σ_1. This change tendency can be further provided interpretation that, large differential pressure favor on hydraulic fracture development direction, which is often observed in laboratory tests ([Zhou et al., 2008]; [Sarmadivaleh and Rasouli, 2015]).

4.2 The influence of fluid viscosity

Under the conditions that the injection rate keeps unchanged as $1.0 * 10^{-5}\mathrm{m}^3/s$, the confining pressure in x-direction and y-direction are both equal to be 20MPa, a series of hydraulic fracturing simulations have been preformed using the injection fluid with different viscosities $1.0 * 10^{-4}Pa/s$, $3.0 * 10^{-4}Pa/s$ and $3.0 * 10^{-3}Pa/s$ to investigate the effect of injecting fluid viscosity on fracture process, such as breakdown pressure, crack propagation and pressure distribution.

It is shown in Fig. III .13 that, the breakdown pressure increase with the increase of fluid viscosity,respectively, as 47MPa, 49MPa and 56MPa. Similarly, the duration time

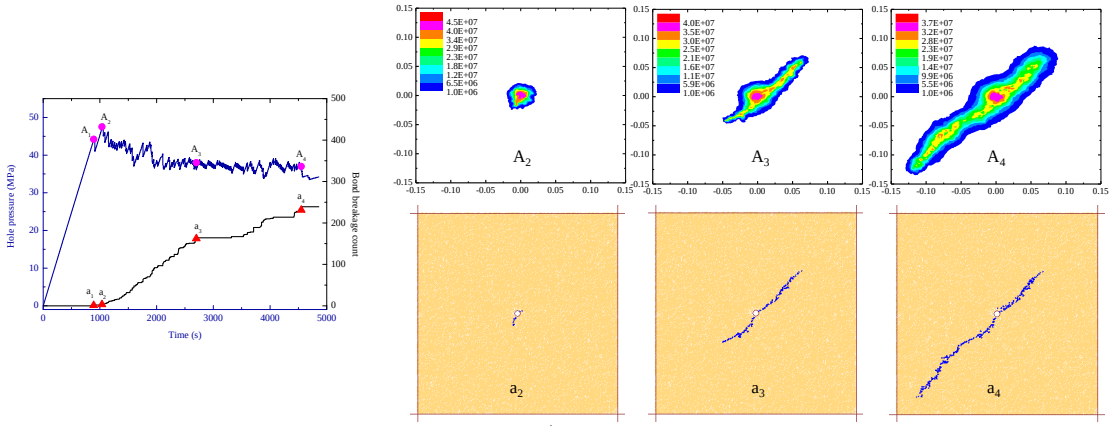

(a) $1.0 * 10^{-4}\ Pa \cdot s$

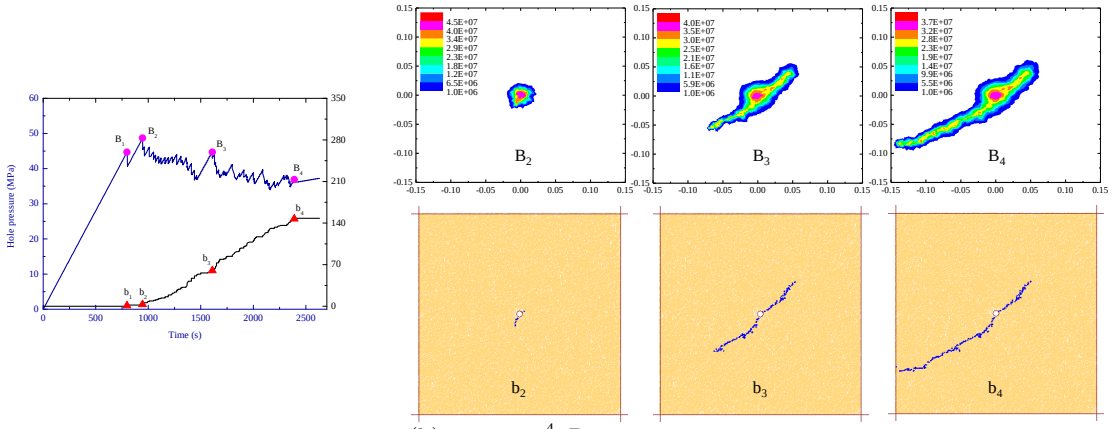

(b) $3.0 * 10^{-4}\ Pa \cdot s$

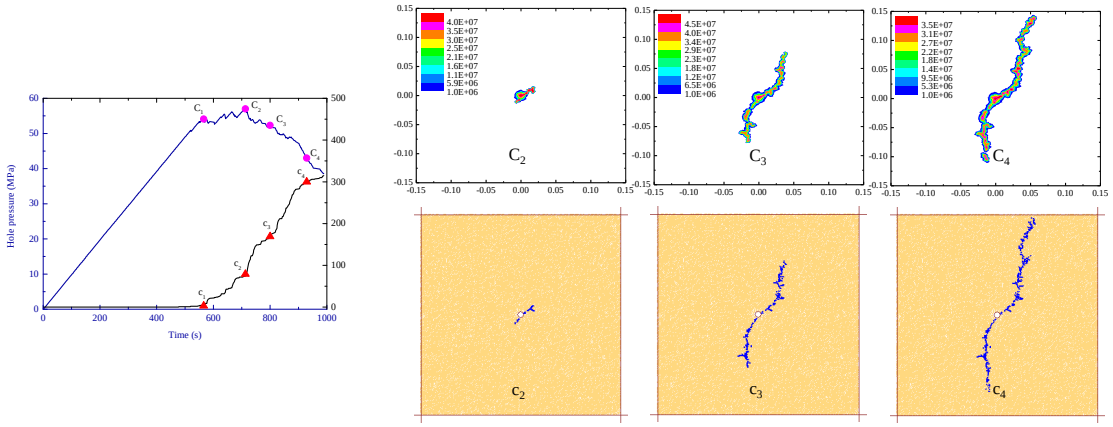

(c) $3.0 * 10^{-3}\ Pa \cdot s$

Figure III .13: Pressure histories of injection hole, fluid field and crack propagation in hydraulic fracturing with the injection rate of $1.0 * 10^{-5}\ m^3/s$ under different fluid viscosities

of injection fluid before breakdown pressure, as well as from crack initiation to sample failure, are also presented increase tendency. This phenomenon can be explained from the analysis of fluid pressure distribution that, because of high viscosity fluid having low fluid infiltration, after the main fracture developing, there still exists large differential press between fracture and the intact rock, which further induces many potential derivative pathways around the main fracture, such as shown in Fig. III .13(c). Compared with concentrated distribution of high viscosity fluid, low viscosity fluid has more advantage on penetrating ability that is contributed to infiltrate these defects originally existing in rock material. The fluid pressure has an obvious gradient distribution for the low viscosity fluid, no matter around the injection hole or on both sides of the hydraulic fracture. This infiltration effect that leads to larger mining surfaces, has also been considered in oil extraction with low viscosity fluid, such as CO2, which can obviously improve the reduction.

4.3 The influence of fluid injection rate

The fluid injection rate is always considered to be an important role in hydraulic fracture. Therefore, in this section, the investigation of injection rate effect on hydraulic fracturing characteristics has also conducted by changing the injection rates applied on sample from $2.0 * 10^{-6}\mathrm{m}^3/s$, $5.0 * 10^{-5}\mathrm{m}^3/s$, to $2.5 * 10^{-4}\mathrm{m}^3/s$. Other parameters remain consistent, such as the fluid viscosity equal to $1.0 * 10^{-3}$ Pa/s, the confining pressure both kept 20MPa in x-direction and y-direction.

The simulation results in Fig. III .14 shows that, with the increase of three injection rates, the breakdown pressure have significant increments respectively as 46MPa, 55MPa and 60MPa. Different with change of duration of injection time, which are both decrease either in stage before breakdown pressure or in stage from crack initiation to sample failure. The reason is that, when the injection rate is high, the differential stress existing in adjacent reservoirs has not enough time to adjust and thus leads to generate more cracks, which indirectly resulting in higher breakdown pressure and less injection time. In Fig. III .14(a), the fluid pressure distribution that the influencing space of low injection rate is distinctly bigger than high one, can be also provide support for this failure mechanism. Moreover, due to this action, such as shown in Fig. III .14(c), either the length or quantity of hydraulic fracture will correspondingly increase with the increase of injection rate. Thus, compared with one main fracture for low injection rate, there are three main ones generated under higher injection rates. The tendency is consistent with observations found in experimental studies.

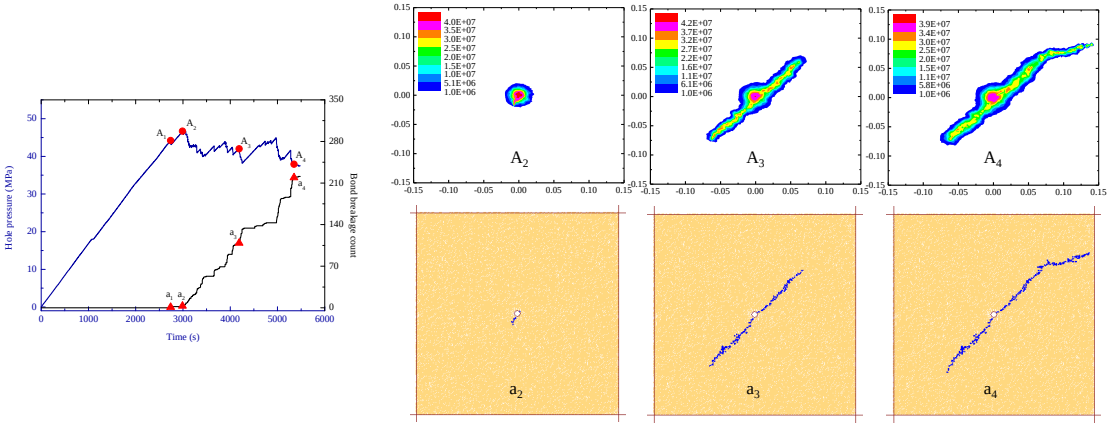

(a) $2.0 * 10^{-6}\ m^3/s$

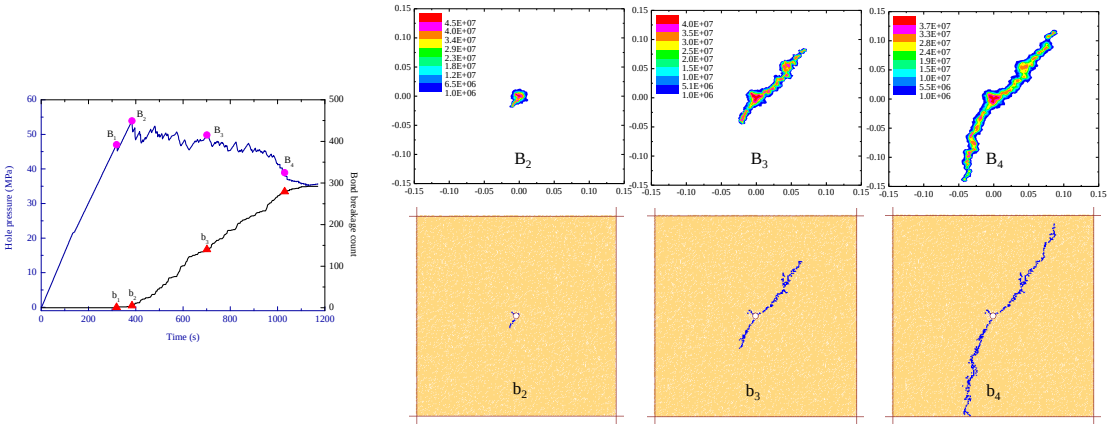

(b) $5.0 * 10^{-5}\ m^3/s$

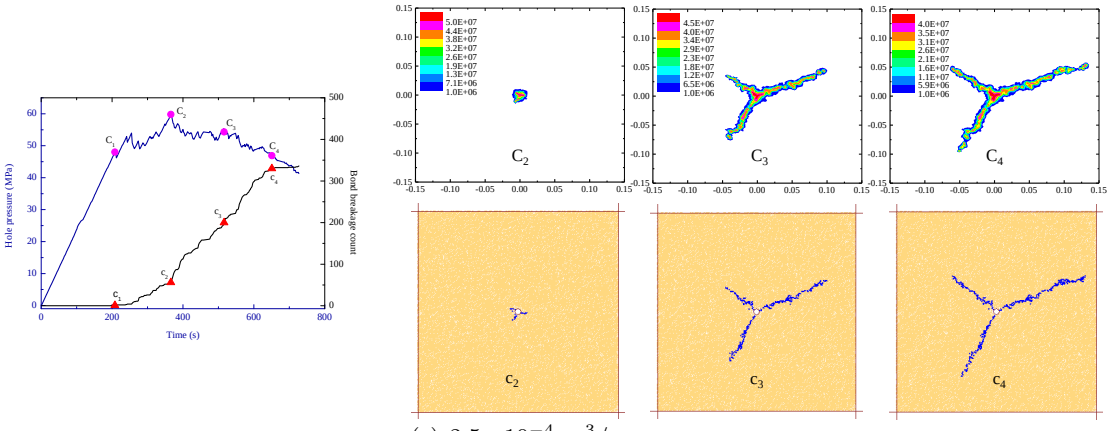

(c) $2.5 * 10^{-4}\ m^3/s$

Figure III .14: Pressure histories of injection hole, fluid field and crack propagation in hydraulic fracturing with a fluid viscosity of $1.0 * 10^{-3}\ Pa \cdot s$ under different injection rates

5 Conclusions

By using the modified fluid mechanically coupled method, a series of investigations against the confining pressure, fluid viscosity and fluid injection rate were performed to investigate their effects on the pore-pressure field and hydraulic fractures formation mechanism. The simulations have good agreements with previous laboratory studies, and the relative results are as follows:

1. The hydraulic fracture sample generated with new proposed bond model is first calibrated and then verified, the results show that the formation and propagation of microcracks in hydraulic fracture sample is mainly induced by tensile force exceeding bond strength.

2. The direction of hydraulic fracture is mainly controlled by pressure state. Its orientation will change with the increase of differential pressure, and is finally parallel to the direction of maximum compression principle stress when the differential pressure is large enough.

3. Fluid with low viscosity can more easily penetrate through the interconnected domains from the fracture into rock, that leads to breakdown pressure decrease and fluid infiltration surface increase. This action provide supplement to be better explain that low viscosity fluid is generally adopted in the production of oil and gas. While the geometry of the fractures is found to be not very sensitive to the fluid viscosity.

4. For the high injection rate, fluid pressure existing in adjacent reservoirs of failure and intact parts can not adjust opportunely, the breakdown pressure becomes large. Moreover, this effect easily resulting in local stress concentration and further causes complex geometry of fracture.

Thus, the dynamic development process of hydraulic fracturing in isotropic rock sample was successfully studied, overcoming disadvantage that the incitation and propagation of cracks can not directly be observed in experiments. However, in actual case, rock material with many flaw has obvious anisotropic characteristics, the hydraulic fracturing process in anisotropy material should be further studied in the following work.

Chapter IV

Three-dimensional Reconstruction of Block Shape Irregularity and its Effects on Block Impacts Using an Energy-Based Approach

Contents

Rock Mechanics and Rock Engineering (2018) 51:1173–1191
https://doi.org/10.1007/s00603-017-1385-x

ORIGINAL PAPER

Three-dimensional Reconstruction of Block Shape Irregularity and its Effects on Block Impacts Using an Energy-Based Approach

Yulong Zhang[1,2] · Zaobao Liu[2] · Chong Shi[1,3] · Jianfu Shao[1,2]

Received: 29 March 2017 / Accepted: 12 December 2017 / Published online: 27 December 2017

Abstract
This study is devoted to three-dimensional modeling of small falling rocks in block impact analysis in energy view using the particle flow method. The restitution coefficient of rockfall collision is introduced from the energy consumption mechanism to describe rockfall-impacting properties. Three-dimensional reconstruction of falling block is conducted with the help of spherical harmonic functions that have satisfactory mathematical properties such as orthogonality and rotation invariance. Numerical modeling of the block impact to the bedrock is analyzed with both the sphere-simplified model and the 3D reconstructed model. Comparisons of the obtained results suggest that the 3D reconstructed model is advantageous in considering the combination effects of rockfall velocity and rotations during colliding process. Verification of the modeling is carried out with the results obtained from other experiments. In addition, the effects of rockfall morphology, surface characteristics, velocity, and volume, colliding damping and relative angle are investigated. A three-dimensional reconstruction modulus of falling blocks is to be developed and incorporated into the rockfall simulation tools in order to extend the modeling results at block scale to slope scale.

Keywords Particle flow method · Energy analysis · Restitution coefficient · Rockfall modeling · Random 3D reconstruction

List of symbols

α_n, α_s	Normal and tangential viscous damping coefficient
ϕ	Internal friction angle between particles
θ, φ	Polar angle and azimuthal angle
ω_i, $\Delta\varpi_i$	Rotational velocity and computed rotation increment of the ith particle
$\overline{\sigma}$, $\overline{\tau}$	Normal and shear strengths of parallel bond
E, E_c, $\overline{E_c}$	Young's modulus of material, particle–particle contact modulus and parallel-bond modulus
E_k, E_s, E_f	Kinetic energy, strain energy and dissipated energy of particles
E_b, E_{b0}	Body work, initial body work
F, F_n, ΔF_s	Contact force, normal force, tangential force in incremental form
F_i	External force
$\lvert F_i^n\rvert$, $\lvert F_i^s\rvert$	Normal and shear components of the contact force for the ith particles
I_i, M_i	Rotational inertia, external moment
N_P, N_s	Total number of particles and contacts
R_n^E, R_t^E	Rockfall normal and tangential restitution coefficient in energy view
$\boldsymbol{S}(\theta, \varphi)$	A set of surface vertex
S, V	The surface and volume of a specified block
ΔU_i	Computed displacement increment for the ith particle
W_0	Initial gravity potential energy
$Y_n^m(\theta, \varphi)\,\boldsymbol{a}_n^m$	Spherical harmonics function and corresponding spherical harmonics coefficient
k_n, k_s	Normal and tangential contact stiffness of particles
k_n^w, k_s^w	Normal and tangential contact stiffness of boundary

✉ Zaobao Liu
zaobao.liu@polytech-lille.fr

✉ Jianfu Shao
jian-fu.shao@polytech-lille.fr

[1] Key Laboratory of Ministry of Education for Geomechanics and Embankment Engineering, Nanjing, Jiangsu 210098, China

[2] Laboratory of Mechanics of Lille, University of Lille, 59650 Villeneuve d'Ascq, France

[3] Geotechnical Research Institute, Hohai University, Nanjing, Jiangsu 210098, China

$\overline{k_n}$, $\overline{k_s}$	Normal and shear stiffness of parallel bond
u	Relative displacement between particles or between particle and boundary
u_n, Δu_s	Normal displacement, tangential displacement in incremental form
g, v_i	The gravitational acceleration, translational velocity
m, n, m_i	Order and degree of the associated Legendre function, the ith particle mass,
$P_n^m(x)$, $p_n(x)$	Associated Legendre functions and the nth order Legendre polynomial
$\boldsymbol{r}(\theta, \varphi)$	Position vector of any surface element of a specified block
r_1, r_2, $\bar{r}$	Radius of two contacting particles, average radius of two contact particles
x, y, z	Three coordinate components in x, y and z directions

1 Introduction

Rockfall refers to the phenomenon of bedrock fragments rapidly moving downward from a cliff face. It is the natural downward motion of a detached block or series of blocks with a small volume involving free falling, bouncing, rolling and sliding. The dominated motions of rockfall vary with the block volumes and slope conditions. For boulders moving downward on a soil surface, rolling and sliding are the dominated motions (de Almeida and Kullberg 2011; Wei et al. 2014); for small blocks moving downward on a hard bedrock slope, free falling, bouncing and rolling are the dominated motions (Asteriou et al. 2012; Zhang et al. 2011; Chau et al. 2002). In this study, we focus on modeling the later, i.e., small blocks moving downward on a hard bedrock slope.

During the rockfall process, there is always colliding between the falling block and the slope. The colliding mechanism of rockfall is complicated and influenced by many factors such as falling block morphology, surface characteristics, incident angle, block volume, block strength and other bedrock properties (Azzoni et al. 1995; Bourrier et al. 2009; Giani et al. 2004; Ansari et al. 2012; de Almeida and Kullberg 2011). To study this problem, the restitution coefficient has been proposed to describe and evaluate the process of rockfall collision.

On this point, various definitions of the restitution coefficient of rockfall have been proposed, but there is no consensus on which definition is the best for rockfall analysis. The most commonly used definition is the ratio of the rebounding velocity to the incident velocity in both the normal and tangential directions of impact surface. This definition has been widely used due to its easiness in accounting for a basic phenomenological description of the rock impacts (Giacomini et al. 2012; Asteriou et al. 2012). For instance, the restitution coefficients are calculated by directly monitoring the velocities of rockfall before and after impact with the high-speed camera in laboratory and their values are found to play a vital role in predicting the trajectories of the rockfall (Ansari et al. 2015). In addition, the restitution coefficients are directly calculated by the ratio of the incident and rebound velocities of falling rocks that are simplified as a cube in the numerical simulation by ANSYS/LS-DYNA (Zhang et al. 2011). Moreover, it is found that the factors such as the impact rocks volume and incident velocity can have an influence on the restitution coefficient.

However, the above definition cannot consider the rotation of falling rocks after impact. It has been modified in order to consider all the three components of the incident and outgoing velocities, respectively, the normal, tangential and rotational ones (Bourrier et al. 2009; Woltjer et al. 2008). For example, in some stochastic impact models, the modified definition of restitution coefficient is adopted to consider the rotational component by multiplying a weight coefficient to the normal and tangential component. This work further justifies that the restitution coefficients vary with the terrain characteristics and the incident kinematic parameters, such as the rotational velocity and incident angle. Despite of these, it is difficult to determine the weight coefficient that accounts for the rotational velocity for a specific terrain and its calibration needs tremendous statistical analysis of large data sets obtained from a large number of suitable numerical impacts.

Another definition of restitution coefficient that can incorporate the rotation effects is established from the energy transformation during rockfall impacts as the square root of the ratio of outbound and incident energy (Richards 1988; Pfeiffer and Bowen 1989; Evans and Hungr 1993; Chau et al. 2002; An and Tannant 2007). It is an advantage that the definition can describe both the energy loss and rotational effects of the falling rocks during rockfall impacts. For instance, an elastic-inelastic power-function contact model was constructed by discrete element method to account for the kinetic energy loss during impact process (An and Tannant 2007), and the restitution coefficient of rockfall was analyzed from the energy view by energy transformation mechanisms during impacts with the assumption that the falling rocks should be spherical and the rotation effect can be neglected. On the contrary, the rotational motions induced by impacts were found to have important effects on the restitution coefficients and thus cannot be ignored in calculation of the restitution coefficients (Chau et al. 2002). This work further found that a more irregular-shape boulder could lead to a larger range of restitution coefficient in the normal direction, when compared to that of spherical boulders.

In those above-mentioned studies, the falling block is commonly regarded as a sphere or an ellipse for the sake of simplicity. However, it has been observed in many field tests that the spatial morphology can affect the rebounding velocity of falling rocks after impacts (Azzoni et al. 1995; Asteriou et al. 2012; Chau et al. 1999) and thus the restitution coefficients. In the analysis with the spherical simplification, the effects of falling block spatial morphology on rockfall restitution coefficients cannot be described. Therefore, further work is needed in analyzing rockfall restitution coefficients that can consider both the rotation effects and the spatial morphology influence of falling rocks in addition to the commonly considered effects mentioned above.

In recent years, the discrete element method has been developed for three-dimensional analysis of rockfall with a regular-shape assumption of falling rocks, as either brick or sphere (Bourrier et al. 2008a, b, 2009; Thoeni et al. 2014). Due to the difficulty in reconstructing three-dimensional morphology, the morphological randomness and irregularity of impacting rocks have rarely been taken into account in rockfall analysis. However, this simplification leads to a great gap between modeling results and actual rockfall properties, such as overestimating the normal velocity, underestimating or even neglecting the tangential and rotating velocity changes of falling rocks. This gap can be bridged by the method based on the three-dimensional reconstruction of impacting rocks using the spherical harmonics, which can well represent its morphology with a high precision.

The present paper firstly presents a new model for reconstructing the three-dimensional morphology of the falling blocks in the context of particle flow method by using the spherical harmonic functions that have both appropriate orthogonality invariance and rotation invariance. Rockfall restitution coefficient analysis is then conducted in the energy view, especially for considering the rotation and shape effects of the falling rocks. The models are then calibrated against experiments and verified by tests. Moreover, parameter effects, such as the rockfall smoothness, damping, rockfall velocity and volume, and the colliding angle, on the rockfall restitution coefficients have also been investigated.

2 Restitution Coefficient of Rockfall by Energy Approach in Particle Models

2.1 Particle Models

Falling rocks of arbitrary shapes can be approximated by an assembly of spherical particles, and the particles can be either bonded or clumped together. Figure 1 shows two basic types of contact models. Figure 1a shows the contact interactions between particles, and Fig. 1b shows those between the particles and boundaries. In these models, the contact force F and the relative displacement u are projected, respectively, into the normal and tangential directions as shown in Fig. 1. The stiffness parameters (k_n and k_s) are then introduced in the contact laws shown in Figs. 2 and 3 to describe the relationships between the contact forces and the relative displacements. The contact laws can be described by the following mathematical equations (PFC2D 1999; Itasca 1999; Potyondy and Cundall 2004; Cundall and Strack 1979):

$$F_n = k_n u_n \tag{1}$$

$$\Delta F_s = k_s \Delta u_s \tag{2}$$

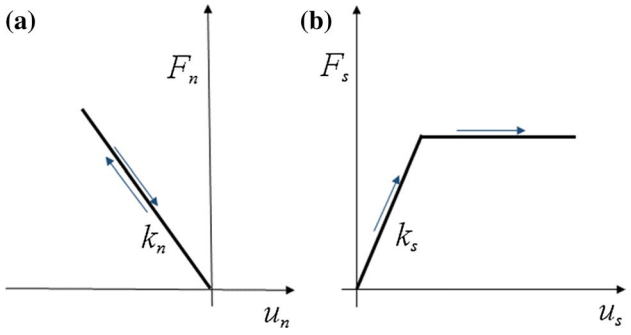

Fig. 2 Illustration of contact law: **a** in normal direction; **b** in tangential direction

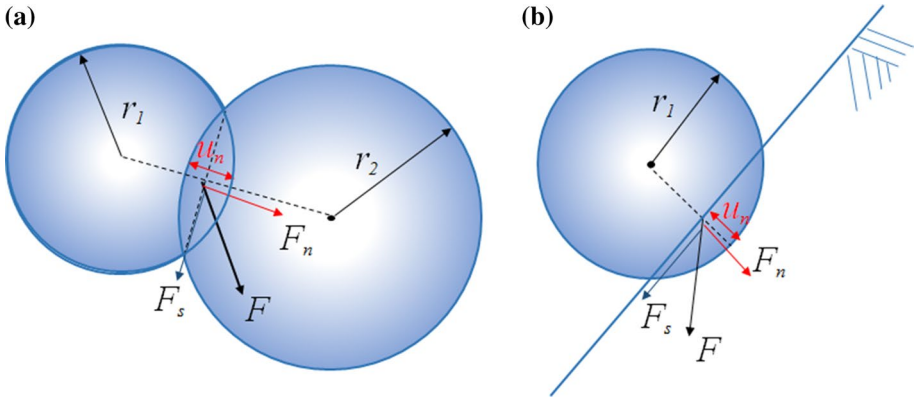

Fig. 1 Descriptive model of overlap and contact force: **a** between two spheres; **b** between a sphere and a slope

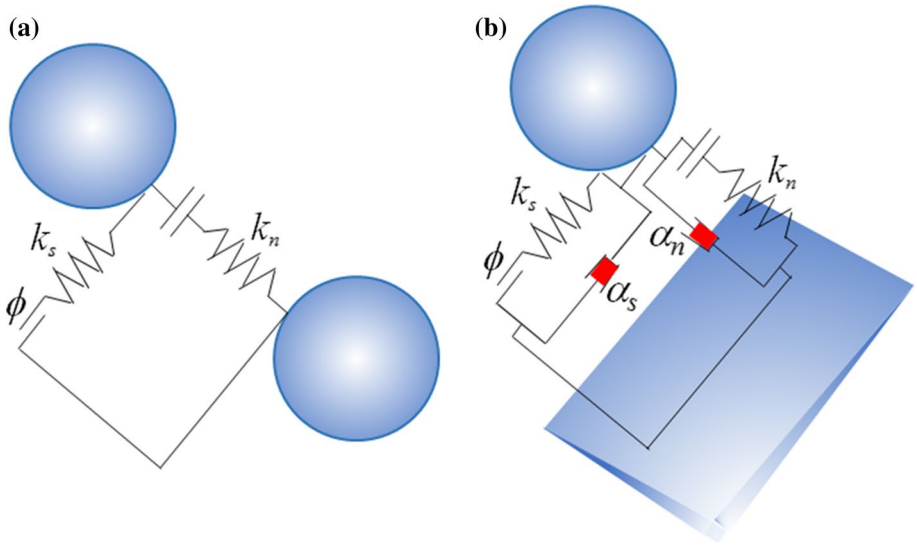

Fig. 3 Energy dissipation model of interaction: **a** between particles; **b** between a particle and a slope

The parameters k_n and k_s are, respectively, the normal and tangential contact stiffness, u_n is the relative normal displacement between two interacting particles, ΔF_s and Δu_s are, respectively, the incremental contact force and relative displacement in the tangential direction. ΔF_s and Δu_s are incrementally updated at each time step. A Coulomb-type slip model with an internal friction angle ϕ is adopted in the tangential direction

$$|F_s| \leq |F_n| \tan \phi \tag{3}$$

The mechanical behavior of bonded particles can be described by the contact laws illustrated in Figs. 2 and 3. Once debonded, the motion of particles is governed by the equations of rigid body dynamics (PFC2D 1999; Itasca 1999).

2.2 Particle Energy During Rockfall Impact

As known, the rockfall process may involve many motions such as free falling, bouncing, rolling, colliding and sliding of rock blocks. From an energy point of view, the motion changes of rockfall are accompanied and accomplished by energy transmissions and dissipations. Thus, several types of particle energy are involved in the rockfall analysis using particle methods (Itasca 1999; PFC2D 1999). Those energy parameters, i.e., the kinetic energy (E_k), strain energy (E_s), body work (E_b) and dissipated energy (E_f), obey the energy balance equation

$$E_k + E_s + E_b + E_f = W_0, \tag{4}$$

where W_0 is the initial gravity potential energy.

The bodywork is the sum of accumulated work done by all body forces in rockfall collision. The body forces include the gravity, externally applied forces and moments. In this way, the bodywork of the particles during the collision can be expressed as

$$E_b = E_{b0} + \sum_{N_p} \left((m_i g + F_i) \Delta U_i + M_i \Delta \varpi_i \right), \tag{5}$$

where E_{b0}, N_P, m_i, g, F_i, M_i, ΔU_i, $\Delta \varpi_i$ are, respectively, the initial body work, the total number of particles, the particle mass, the gravitational acceleration, the external force, the external moment, the displacement increment and the rotational velocity increment of a particle at the current time step. In the present computing, g, F_i and M_i are constants, while F_i and M_i are equal to zero since there are no externally applied forces and moments.

The total kinetic energy of all particles can be calculated in terms of the generalized mass (m_i) and velocity (v_i) of each particle,

$$E_k = \frac{1}{2} \sum_{N_p} (m_i \boldsymbol{V}_i^2 + \mathbf{I}_i \boldsymbol{\omega}_i \cdot \boldsymbol{\omega}_i) \tag{6}$$

where $N_P, m_i, \boldsymbol{I}_i, \boldsymbol{V}_i$ and $\boldsymbol{\omega}_i$ are, respectively, the number of particles, inertial mass, rotational inertia, and translational and rotational velocities of particle i.

With a linear contact-stiffness model, the total strain energy stored at all contacts can be calculated by

$$E_s = \frac{1}{2} \sum_{N_s} \left(|F_i^n|^2 / k_n + |F_i^s|^2 / k_s \right), \tag{7}$$

where N_s is the total number of contacts; $|F_i^n|$ and $|F_i^s|$ are, respectively, the magnitudes of normal and shear components of the contact force.

The dissipated energy is related to the various dissipation mechanisms induced by the variety of properties of

falling blocks and slopes (Pöschel and Schwager 2005; An and Tannant 2007; Thoeni et al. 2014). In this study, we focus on the modeling of small rock blocks bouncing on hard bedrock. The friction-induced dissipation energy is very limited in this case; thus, we introduce the viscous damping to take into account the dissipated energy, respectively, in the normal and tangential directions of a contact surface as shown in Fig. 3

$$F_{\mathrm{n}} = k_{\mathrm{n}} u_{\mathrm{n}} + \alpha_{\mathrm{n}} \frac{\mathrm{d}u_{\mathrm{n}}}{\mathrm{d}t} \tag{8}$$

$$\Delta F_{\mathrm{s}} = k_{\mathrm{s}} \Delta u_{\mathrm{s}} + \alpha_{\mathrm{s}} \frac{\mathrm{d}u_{\mathrm{s}}}{\mathrm{d}t} \tag{9}$$

where α_{n} and α_{s} are, respectively, the viscous damping coefficient in the normal and tangential directions; $\frac{\mathrm{d}u_n}{\mathrm{d}t}$ and $\frac{\mathrm{d}u_s}{\mathrm{d}t}$ are, respectively, the relative normal and tangential velocity in contact.

2.3 Restitution Coefficient of Rockfall in Energy View

The falling projectile can be traced during rockfall impact, and thus the accumulated energy change can be calculated. With consideration that the impacting rocks rising after collision is induced by the normal force, and its rotation is caused by the tangential force, then the restitution coefficient can be defined as (Chau et al. 1999, 2002; An and Tannant 2007):

$$R_{\mathrm{n}}^{\mathrm{E}} = \left(\frac{E_{\mathrm{b2}} + (E_{\mathrm{k2}} - E_{\mathrm{k3}}) + E_{\mathrm{s2}}}{E_{\mathrm{b1}} + E_{\mathrm{k1}} + E_{\mathrm{s1}}} \right)^{0.5} \tag{10}$$

$$R_{\mathrm{t}}^{\mathrm{E}} = \left(\frac{E_{\mathrm{b3}} + E_{\mathrm{k3}} + E_{\mathrm{s3}}}{E_{\mathrm{b1}} + E_{\mathrm{k1}} + E_{\mathrm{s1}}} \right)^{0.5} \tag{11}$$

$R_{\mathrm{n}}^{\mathrm{E}}$ and $R_{\mathrm{t}}^{\mathrm{E}}$ are, respectively, the block normal and tangential restitution coefficients from an energy point of view. The quantity $E_{\mathrm{b1}} + E_{\mathrm{k1}} + E_{\mathrm{s1}}$ represents the total energy before the first collision. E_{k2} is the total kinetic energy in the vertical direction caused by macro-normal force after the first colliding-rebounding process. E_{k3} is the total kinetic energy in the horizontal direction and rotation energy induced by macro-shear force when the block rebounds to its rebound limit. E_{b3} and E_{s3} are, respectively, the body work and kinetic energy at the current point.

The definition of restitution coefficient given in Eqs. (10) and (11) is similar to the commonly used one that is the ratio of rebound velocity to the incident velocity by considering the rotational effect (Bourrier et al. 2008a, 2009). The additional advantage is that the present definition can easily take into account the rotational energy of falling blocks during impacts.

3 Three-dimensional Reconstruction of Falling Rocks

Falling rocks are commonly regarded as a sphere or an ellipse for simplification. However, this simplification can lead to some drawbacks, for example, overestimating the normal velocity, and underestimating or even neglecting the tangential and rotational velocity change of impacting blocks. To overcome such drawbacks, we propose the three-dimensional reconstruction of falling blocks to represent its microscopic morphology at a high precision with the help of the spherical harmonics.

3.1 Spherical Harmonics and Its Descriptors

The spherical coordinates originated at the centroid illustrated in Fig. 4 can describe an arbitrary 3D block with known external contour points (Shi et al. 2016). According to the transformations between Cartesian and spherical coordinate systems, the contour points in Cartesian coordinates can be represented as $\boldsymbol{S}(\theta, \varphi)$ (θ and φ satisfy $0 \le \theta \le \pi$ and $0 \le \varphi \le 2\pi$) as follows:

$$\boldsymbol{S}(\theta, \varphi) = (x(\theta, \varphi), y(\theta, \varphi), z(\theta, \varphi))^T \tag{12}$$

The full coordinates of any points in the block surface can be analyzed by spherical harmonics series as (Shi et al. 2016)

$$\boldsymbol{S}(\theta, \varphi) = \sum_{n=0}^{\infty} \sum_{m=-n}^{n} \boldsymbol{a}_n^m Y_n^m(\theta, \varphi) \tag{13}$$

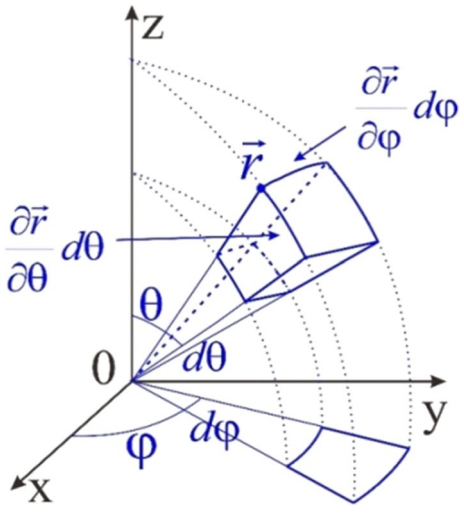

Fig. 4 Hexahedron element in spherical coordinate system

$\boldsymbol{a}_n^m$ is the corresponding spherical harmonics coefficient that needs to be determined, $Y_n^m(\theta, \varphi)$ denotes the spherical harmonics function given by

$$Y_n^m(\theta,\varphi) = \sqrt{\frac{(2n+1)(n-m)!}{4\pi(n+m)!}} P_n^m(\cos\theta) e^{im\varphi} \tag{14}$$

The parameters n and m are the degree and order of $P_n^m(x)$, which is the associated with Legendre functions by:

$$P_n^m(x) = \left(1-x^2\right)^{m/2} \frac{\mathrm{d}^m}{\mathrm{d}x^m} p_n(x) \tag{15}$$

$p_n(x)$is the n order Legendre polynomial expressed by Rodrigues' formula:

$$P_n(x) = \frac{1}{2^n n!} \frac{\mathrm{d}^n}{\mathrm{d}x^n} \left(x^2-1\right)^n \tag{16}$$

Finally, taking the known surface points and corresponding spherical harmonics function values into Eq. (13), the above relation can be extended to a matrix form (Zhou et al. 2015):

$$\begin{pmatrix} y_1^1 & y_1^2 & \cdots & y_1^{(n+1)^2} \\ y_2^1 & y_2^2 & \cdots & y_2^{(n+1)^2} \\ \vdots & \vdots & \ddots & \vdots \\ y_i^1 & y_i^2 & \cdots & y_i^{(n+1)^2} \end{pmatrix} \begin{pmatrix} a_x^1 & a_y^1 & a_z^1 \\ a_x^2 & a_y^2 & a_z^2 \\ \vdots & \vdots & \vdots \\ a_x^{(n+1)^2} & a_y^{(n+1)^2} & a_z^{(n+1)^2} \end{pmatrix} = \begin{pmatrix} x_1 & y_1 & z_1 \\ x_2 & y_2 & z_2 \\ \vdots & \vdots & \vdots \\ x_i & y_i & z_i \end{pmatrix} \tag{17}$$

$\boldsymbol{y} = \left[y_i^1, y_i^2, \ldots, y_i^{(n+1)^2}\right]$ is reshaped by $Y_n^m(\theta, \varphi)$ from a triangle matrix to a row vector with θ_i and φ_i being the ith pair of the spherical coordinates of the particle surface points $\boldsymbol{S}(\theta, \varphi)$. Accordingly, the matrix form of $\boldsymbol{a}_n^m$ is also reshaped to $\boldsymbol{a} = \left[a^1, a^2, \cdots, a^{(n+1)^2}\right]^T$ in a similar way but transposed to a column vector. Generally, the number of parameterized surface points i is bigger than $(n+1)^2$: thus, it is possible to solve these linear equations and determine all of the coefficients $\boldsymbol{a}_n^m$.

The volume and surface area of the reconstructed block can be used to evaluate the microscopic characteristics of falling rock. The volume can express its uniformity while its surface area can represent its texture characteristics. In Fig. 4, the block is divided into several rectangular pyramids. The position vector of any surface element from the block center $\boldsymbol{S}_0^T$ is given by:

$$\boldsymbol{r}(\theta,\varphi) = \boldsymbol{S}(\theta,\varphi)^T - \boldsymbol{S}_0^T \tag{18}$$

By superimposition of each part (Shi et al. 2016), the surface and volume of the block can be calculated, respectively, by

$$S = \int_0^{\pi} \int_0^{2\pi} \left| \frac{\partial \boldsymbol{r}}{\partial \theta} \times \frac{\partial \boldsymbol{r}}{\partial \varphi} \right| \mathrm{d}\theta \mathrm{d}\varphi \tag{19}$$

$$V = \frac{1}{3} \int_0^{\pi} \int_0^{2\pi} \left(\frac{\partial \boldsymbol{r}}{\partial \theta} \times \frac{\partial \boldsymbol{r}}{\partial \varphi} \right) \cdot \boldsymbol{r} \mathrm{d}\theta \mathrm{d}\varphi \tag{20}$$

These two variables are used as the criteria to evaluate the precision of reconstruction of the rock spatial morphology.

3.2 Particle Reconstruction Based on Spherical Harmonics

The first step of rock block 3D reconstruction is to obtain external contours of representative particles. This step can be proceeded with a DAVID-SLS-2 scanner to scan the representative particles, and thus the 3D images can be obtained as shown in Fig. 5a. Then, these images are subjected to segmentation and binary treatment before that a pre-processing is applied to eliminate the noises (e.g., removing unconnected points and lines). In this way, the boundaries and the coordinates of each pixel point of the block can be recognized, and thus the external contours of the rockfall block can be identified. Afterward, by introducing the spherical harmonics and counting the corresponding coefficients

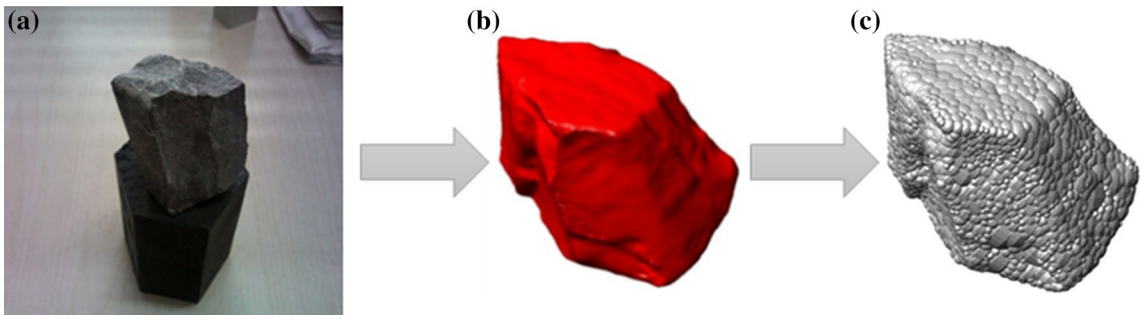

Fig. 5 Steps of clump based on 3D laser scanning: **a** rock samples, **b** scanning samples to reconstruct morphology of samples with particles, **c** filling the contour using ODEC

after standard placement of the rockfall particles, the three-dimensional rockfall model is randomly reconstructed according to the spherical harmonic coefficients (Das et al. 2008; Shi et al. 2015).

Figure 6 shows the reconstruction results of the block particle micromorphology by the spherical harmonics functions with different degrees. The spherical harmonics descriptors of the reconstructed models with different numbers of degree are shown in Fig. 7. It is indicated in Figs. 6 and 7 that the number of degree of the spherical harmonics can greatly improve the reconstructed results.

The reconstructed results can approach perfectly the morphology of the scanned block when the number of degree is greater than 10. The reconstruction precision is mainly dependent on the quality of the scanned falling block if the maximum number of degree of the spherical harmonics is chosen, which is also quantitatively indicated by the spherical harmonic descriptors shown in Fig. 7.

As illustrated in Fig. 8, rock blocks of different spatial morphology can be reconstructed in three dimensions with the proposed method when the degree of the spherical harmonics is taken as 15. Therefore, the three-dimensional reconstructed method can be applied to model rock blocks of arbitrary shapes.

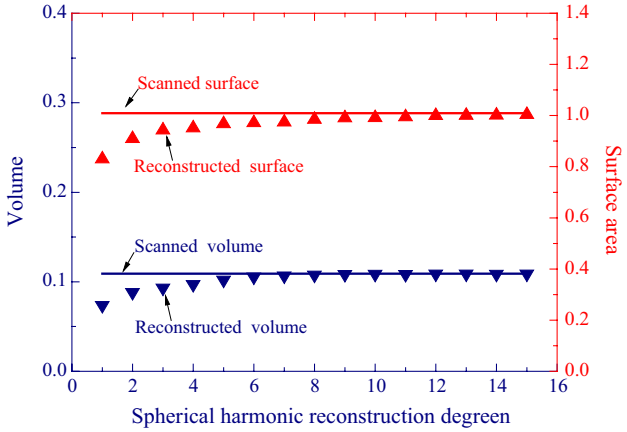

Fig. 7 Spherical harmonics descriptors of reconstructed models

4 Three-dimensional Modeling of Falling Block

4.1 Recall of Rockfall Field Tests

Field rockfall experiments were previously reported in literature (Zhang et al. 2011; Giacomini et al. 2012), and the whole colliding process of rockfall was captured by high-speed video systems. The falling and rebounding process of rockfall can be divided into three phases: (i) rock block free falling phase, (ii) colliding-rebounding phase of rock block during impact with bedrock, (iii) rock block rebounding-rising phase. The rotations of rock blocks occur in the rockfall process especially in the second phase. Thus, the rotational effect should be taken into account although it is neglected in many rockfall simulations where only the normal velocity effects are considered.

Two representative groups of rockfall field tests are recalled and summarized in Table 1 (Zhang et al. 2011) where the block and slope conditions of each test are given with other testing conditions such as the incident velocity, incident angle, rebound velocity and rebound angle. The first group of tests is on rockfall of blocks colliding on a smooth hard bedrock, and the second group is on rockfall of blocks colliding on bedrock with a thin layer of clastic sediments on the surface. In the field tests (Zhang et al. 2011), the falling rocks are small blocks with equivalent length ranging from 0.1 to 0.2 m. The equivalent length here is the edge length of a hypothetical cube that has the same volume as the rock block in question.

In addition, the restitution coefficients calculated by the ratio of rebound and incident velocity are given in Table 1 in both normal and tangential directions. It should be noted that, albeit in a different form, the experimental restitution coefficients in Table 1 are smaller than those reported in literature (Pfeiffer and Bowen 1989; Richards 1988), particularly for the tangential ones. The differences are probably

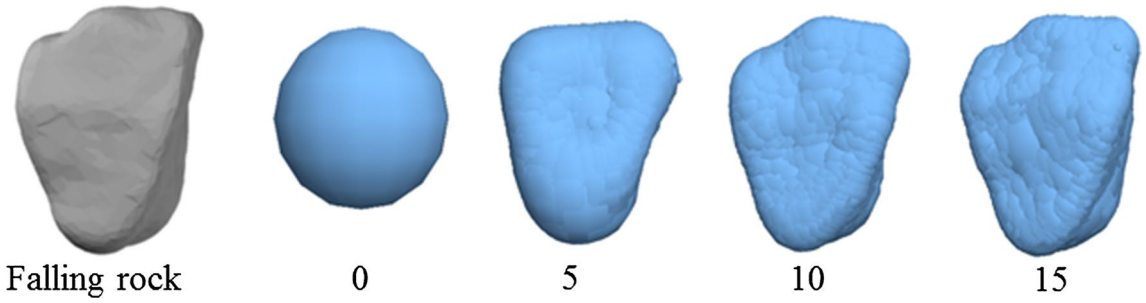

Fig. 6 Reconstructed morphology of falling block with different degrees

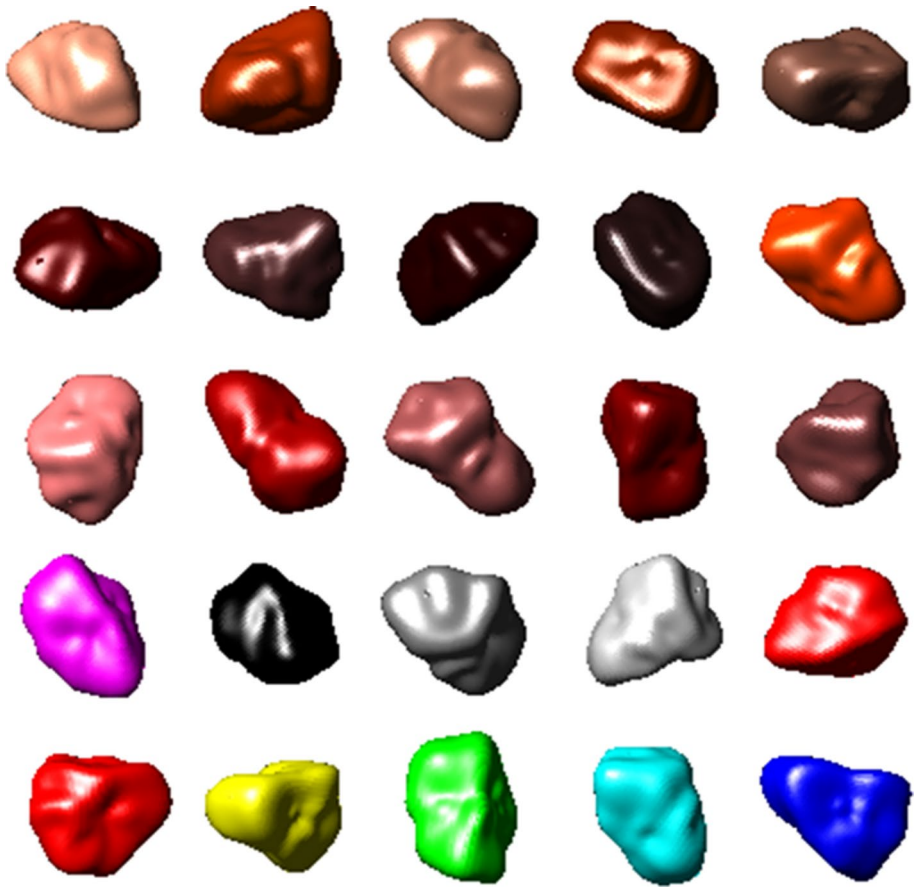

Fig. 8 Different spatial morphologies for different reconstruction of falling rock

Table 1 Conditions and restitution coefficient values of field rockfall test (Zhang et al. 2011)

Slope condition	Test number	Equivalent length	Incident speed	Incident angle	Rebound speed	Rebound angle	Collision restitution coefficient	
		(cm)	(m/s)	(°)	(m/s)	(°)	Normal	Tangential
Smooth bedrock	A06	9.9	9.47	82	5.915	87	0.63	0.21
	A09	10.2	8.16	72	4.658	88	0.6	0.05
	A14	9	4.46	40	1.85	74	0.62	0.15
Clastic accumulation	B13	12.4	9.27	56	4.409	40	0.37	0.65
	B28	14.3	7.61	90	2.892	90	0.38	0
	B31	16	8.57	50	4.6	41	0.46	0.63

The equivalent length represents side of hypothetical cubic rock, which has the same volume with actual rock

related to two reasons. For the first, in the experiment, the restitution coefficients are calculated by the ratio of rebound velocity and incident velocity. The rebound velocity recorded by a high-speed camera is underestimated since the rotations are not sufficiently described. For the second, the experiments are carried out on impacts of small blocks while the work in literature deals with impacts of boulders. Due to the friction-dominated mechanisms in boulders, the rotations in boulder impacts are much more important than those in small block impacts that are dominated by rebound.

Some physical and mechanical properties of the falling block and bedrocks are given in Table 2, which will be used to calibrate the basic particle parameters of the falling rocks. The field test results will be used to validate the analysis of rockfall restitution coefficients by the reconstructed 3D block model with the particle flow method.

Based on the field tests, the following work will focus on modeling of rock blocks of a small volume, such as pebble and rubble. In addition, since the impacted slopes are bedrocks, the present study considers that the impacting motions

Table 2 Physico-mechanical parameters of falling rock and bedrock (Zhang et al. 2011)

Materials		Density (kg/m3)	Elastic modulus (Pa)
Falling rock		2390.0	1.0×10^{10}
Bedrock	Smooth bedrock	2390.0	8.0×10^{9}
	Clastic deposit bedrock	2100.0	6.0×10^{8}

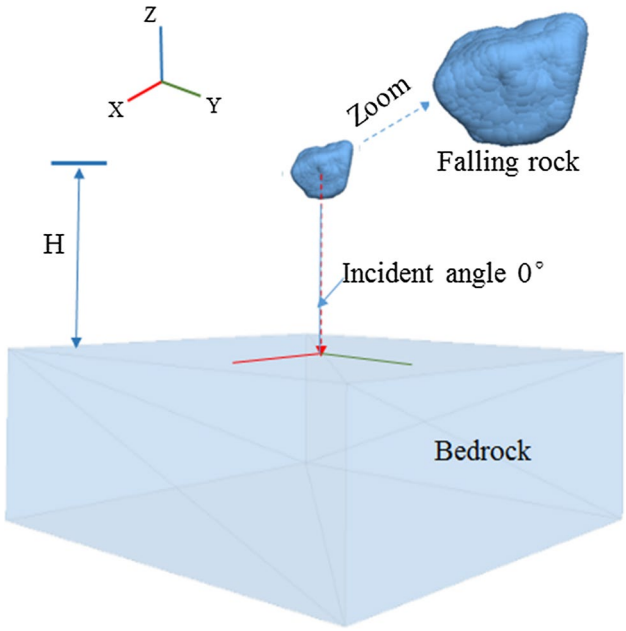

Fig. 9 Three-dimensional reconstruction model of rockfall

of blocks are dominated by free falling, colliding, rotating and rebounding.

4.2 Block Colliding Model

The numerical model of the block collision is established according to the field tests. The model takes a region that has an edge size of ten times of the equivalent length of the rock block as shown in Fig. 9. The impact of block is assumed to take place at the ground center. In the modeling, the falling block is initiated at 1.6 m over the ground with a free falling at an incident angle of 0°. Each colliding process lasts no more than 0.04 s. Thus, the duration of the impact process is taken as 2 s in the simulation that includes a complete colliding process.

The falling block is reconstructed by the particle method introduced previously and thus the rotational effect can be incorporated in the modeling. We assume that the falling block does not break up during impact with the bedrock surface to focus on the energy consumption mechanism. The parallel-bonded contact model (Potyondy and Cundall 2004; Itasca 1999; Deng et al. 2014) is used for the particles in reconstructing the falling block. The bedrock is thought to be a rigid slope in setting the block impact model.

A complete impact process is reconstructed as shown in Fig. 10. The reconstruction process also includes three phases, i.e., the free falling phase before impact in Fig. 10a, the colliding-rebounding phase in Fig. 10b, and the rebounding-rising phase Fig. 10c. As shown in Fig. 10c, the rotation of the rock block after colliding has been well simulated in the modeling before the rebound-rising phase.

4.3 Model Calibration

There are two groups of parameters to be calibrated in the modeling, which are, respectively, the parameters of the falling rocks and impacted bedrock. For simulating the

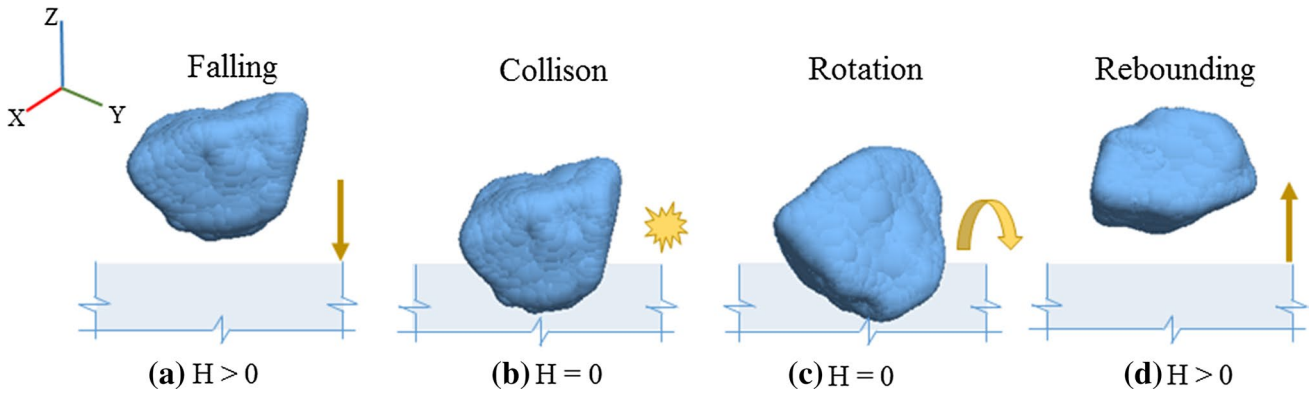

Fig. 10 Rebounding process of reconstructed model of impacting rock: **a** free falling phase, **b** spatial position before colliding, **c** rotating in collision, **d** rebounding phase

unbreakable falling rocks, the parallel-bond contact models are applied between the particles, which have also a couple of parameters (see Table 3).

The stiffness parameters of the falling block and the bond models (Potyondy and Cundall 2004; Itasca 1999) can be calibrated by Eq. (21) from the Young's modulus of the rock material and diameters of the contacting particles

$$\begin{cases} k_{\mathrm{n}} = 2E_{\mathrm{c}}(r_1 + r_2) \\ k_{\mathrm{s}} = \dfrac{k_{\mathrm{n}}}{\left(k_{\mathrm{n}}/k_{\mathrm{s}}\right)} \\ \overline{k_{\mathrm{n}}} = \dfrac{\overline{E_{\mathrm{c}}}}{r_1 + r_2}, \\ \overline{k_{\mathrm{s}}} = \dfrac{\overline{k_{\mathrm{n}}}}{\left(\overline{k_{\mathrm{n}}}/\overline{k_{\mathrm{s}}}\right)} \end{cases} \tag{21}$$

where E_{c} and $\overline{E_{\mathrm{c}}}$ are the Young's modulus of falling block and parallel contacts, which can be obtained from the results of field or laboratory tests as presented in Table 2; $\overline{k_{\mathrm{n}}}$ and $\overline{k_{\mathrm{s}}}$ are, respectively, the normal and tangential stiffness of the parallel-bond models; r_1 and r_2 are the diameters of two contacting particles.

We have firstly carried out numerical triaxial tests on a cylinder sample of 400 mm in diameter and 800 mm in height to calibrate the stiffness parameters in Eq. (21) with the modulus value given in Table 2. The numerical triaxial sample is constituted of 8000 particles whose diameters are randomly generated with largest and smallest values, respectively, of 16 and 10 mm. Its porosity is set as 0.13, and the grain density is taken as 2.75 g/cm^3 so that the specific density is 2.39 g/cm^3. The strength parameters ($\bar{\sigma}$, $\bar{\tau}$ and ϕ) are adjusted with an initial value by the relationships presented in previous work (Jiang et al. 2007, 2011; Shi et al. 2013; Deng et al. 2014). The triaxial test is carried out iteratively to adjust the particle parameters so that the macroscopic elastic moduli are the same as those given in Table 2. The obtained material parameters of the falling rocks and bedrock are finally given in Table 3.

Once the material parameters are calibrated, the test A06 in Table 1 is then used to calibrate the damping in the falling block model. The calibration of the damping is also carried out iteratively by a numerical optimal process with an initial value and a step. The critical condition of iteration is that the generalized restitution coefficients are the same as those in the field test (Thoeni et al. 2014). In this way, the damping values can be calibrated as given in Table 3.

Table 3 Parameters specified in rockfall three-dimensional modeling

Rockfall model	Parameters			Value	Note
Falling rock	Particle properties	Young's modulus (GPa) E_{c}		10.0	
		Density ρ (kg/m^3)		2810.0	
		Stiffness (N/m)	Normal k_{n}	6.0×10^8	
			Tangential k_{s}	2.4×10^8	
		Damping	Normal α_{n}	0.09	Smooth bedrock
			Tangential α_{s}	0.14	
			Normal α_{n}	0.12	Clastic deposit bedrock
			Tangential α_{s}	0.06	
		Friction φ		0.6	
	Bond properties	Young's modulus (GPa) $\overline{E_{\mathrm{c}}}$		10.0	
		Stiffness (N/m^3)	Normal $\overline{k_{\mathrm{n}}}$	3.0×10^{11}	
			Tangential $\overline{k_s}$	1.2×10^{11}	
		Strength (N/m^2)	Normal $\bar{\sigma}$	1.0×10^5	
			Tangential $\bar{\tau}$	0.5×10^5	
		Radius multiplier $\overline{\lambda}$		1.0	
Bedrock	Smooth bedrock	Stiffness (N/m)	Normal k_{n}^w	4.6×10^8	
			Tangential k_{s}^w	1.0×10^8	
	Clastic deposit bedrock	Stiffness (N/m)	Normal k_{n}^w	3.6×10^7	
			Tangential k_{s}^w	2.2×10^7	

4.4 Calibration of Block Morphology and Comparison of Spherical Model and 3D Reconstructed Model

In order to investigate the effect of block morphology, the outcomes of the three-dimensional reconstructed models are compared to those of the commonly used spherical model. For simplification in comparison, no damping is present in the modeling herein. The results of energy and velocity change during impacts obtained by the two models are illustrated in Fig. 11.

It is shown in Fig. 11a that the kinetic energy and the velocity before and after impact of the spherical model reach the maximum value at the point E_{K1} (V_{N1}) and arrive at the minimum value at the point E_{K3} (V_{N3}). Meanwhile, this tendency exhibits no change after multiple collisions as indicated by E_{K1} and E_{K4}. It can be seen in Fig. 11a that kinetic work dominates the energy in this case since the strain energy and body works tend to zero. It is feasible and reasonable to investigate the restitution coefficient based on kinetic energy statistics for the 3D reconstructed method.

It is shown in Fig. 11b that there is no rotational velocity at point V_{N3} by the spherical model due to the sphere

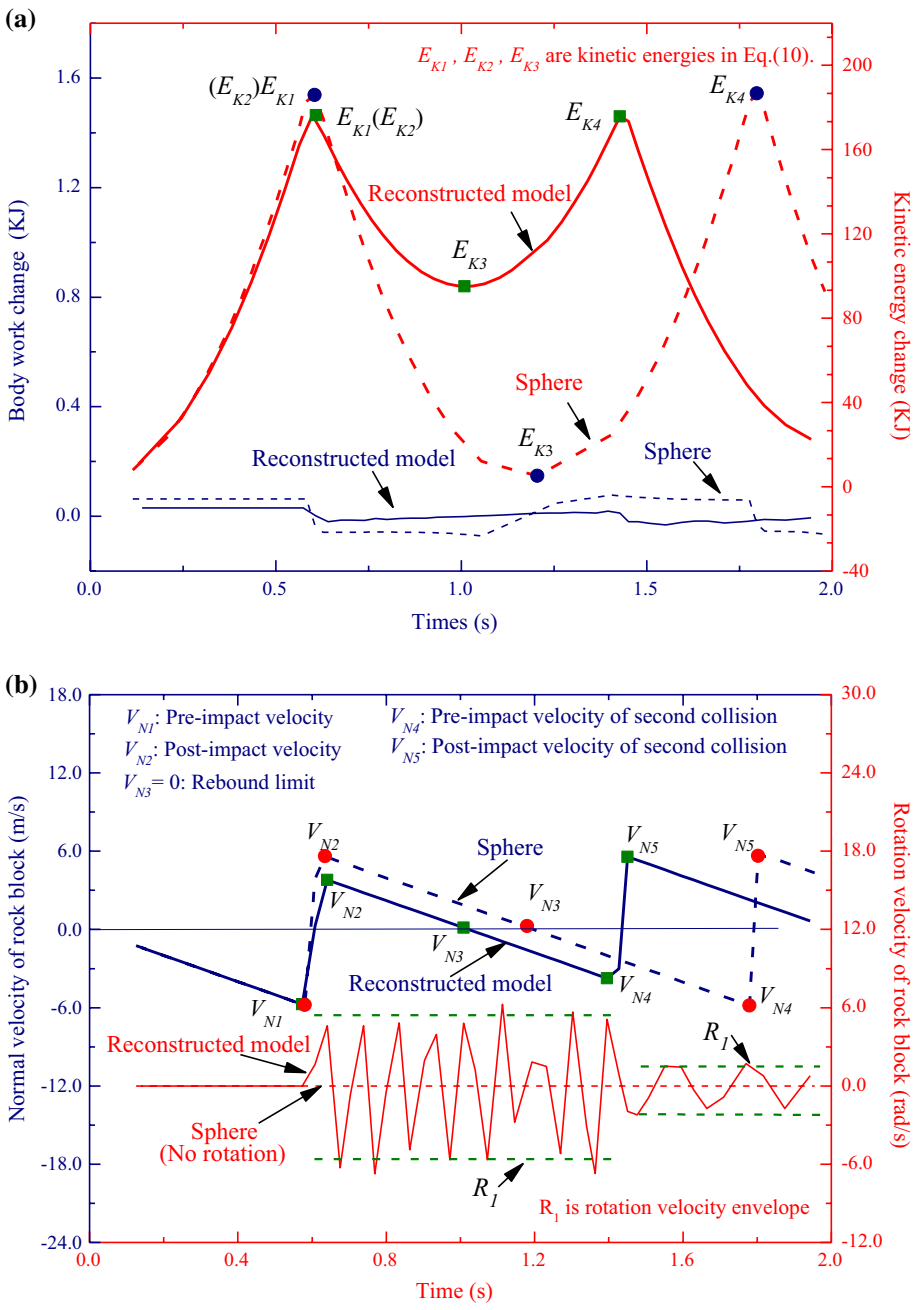

Fig. 11 Outcome comparisons of spherical model and 3D reconstructed model: **a** energy change, **b** velocity change

simplification of rock blocks. Thus, the normal restitution coefficient is calculated to be 1.0 by the spherical model. On the contrary, the rotation has been well simulated in the 3D reconstructed model as indicated in Fig. 11b. At the point of V_{N3}, the falling block reaches its rebound limit at which the normal velocity is zero. In the 3D reconstructed model, the normal velocity is zero, whereas there is still a rotational velocity obtained by the envelope R_1 in Fig. 11b. In consequence, the kinetic energy has thus a value of 110 kJ at the point E_{K3} due to rotational effects as indicated in Fig. 11a. The rotational effects can be further demonstrated in Fig. 11b by the rotational velocity envelope R_1 that gives a more detailed information of rotations in the falling block impact process.

Therefore, the 3D reconstructed model is advantageous to the commonly used spherical model. The 3D reconstructed model can represent the micromorphology of the falling block and thus it can simulate the rotation of falling block during impacts.

4.5 Calibration of Energy Dissipation and Modeling with Energy Dissipation

The above analysis can describe the falling block dynamic properties such as the rotations during the collision process. However, collision is always accompanied with energy dissipation. Thus, it is necessary to model rockfall with energy dissipation. In this paper, the energy dissipation is considered by damping. Figure 12 shows the simulated results of the 3D reconstructed model with different values of damping.

It is shown in Fig. 12a that the total energy of falling block collision without damping changes from the point E_{K1} to E_{K4}. No energy loss occurs during the collision process of falling block without damping. In contrast, the energy for the model with regular damping reduces evidently from the point E_{K1} to E_{K2} and finally to E_{K4} after impact. There is energy loss in each collision, which agrees well with the field block impact tests. The kinetic energy values at the point E_{K3} indicate that the rotational energy takes different percent in the block kinetic energy for the models with different damps.

It is illustrated in Fig. 12b that the velocity change in the model without damping exhibits as the inter-transformation of the normal velocity and the rotational velocity. For instance, the rotational velocity of the model without damping has a great value when the block normal rebounding velocity is small at point V_{N2}. Then, the rotational velocity decreases along the envelope R_1 with increasing normal velocity to point V_{N5}. In addition, the total kinetic energy remains constant in Fig. 12a from the point E_{K1} to E_{K4}.

In contrast, the velocity in the regular damping models shows a progressively decreasing trend from the point V_{N2} to V_{N5}, which is synchronously indicated by the total kinetic energy in Fig. 12a. However, the rotational velocity envelop R_2 in Fig. 12b has no obvious change with the decrease in the rebounding normal velocity in the regular damping model. The decrease of the total kinetic energy of the falling block is due to the damping-induced energy dissipation. Whereas, the rotational velocity (envelop R_2) depends on the interactions between the falling block and the impacted bedrock, and it is influenced mainly by the falling block surface micromorphology. In addition, the rotational velocity is much smaller than the normal velocity as indicated in Fig. 12b. If the reconstructed falling block is regressed to be a sphere, the rotational velocity will further decrease to zero as the case of the spherical models.

Therefore, the 3D reconstructed model can simulate energy dissipation during impact by the damping method. Energy dissipation has evident reduction effect on normal velocity and kinetic energy but has little effect on the rotational velocity and energy.

4.6 Verification of Modeling Results Against Field Tests

The rockfall case A06 is taken as an example to demonstrate in detail the process of the proposed method for block impact simulation. As evidenced above, a precise morphology of falling block in rockfall analysis is essential for analyzing restitution coefficient; thus, spherical harmonic functions are adopted with higher degrees, i.e., $n = 15$. The reconstructed falling block model of the case A06 is shown in Fig. 13. The incident angle of falling rocks is 82° in the test.

The parameters of falling rocks and the bedrocks are specified the same as the model calibration results in Table 3. In order to decrease particles size effect, the falling block is filled by particles of 10.0–16.6 mm in diameter that are generated by the same distribution as that in the cylinder specimen of calibration triaxial test. Meanwhile, the normal and tangential stiffness of the rigid boundary are, respectively, set as 4.6×10^8 Pa and 1.0×10^8 Pa. The normal and tangential damping values are taken, respectively, as 0.09 and 0.14 to simulate the energy dissipations. The falling block simulations are conducted with the parameters given in Table 3, and the results are shown in Fig. 14. Then, the normal and tangential restitution coefficients are calculated by Eqs. (10) and (11) to be, respectively, 0.59 and 0.21 for the rockfall test A06.

In addition to the rockfall case A06, the other tests in Table 1 are also simulated in a similar way with the parameters specified in Table 3. According to the field tests, the bedrock with clastic deposits on surface has different mechanical and physical properties from the smooth ones. As a result, the calibrated parameters of the models are different between the two types of bedrocks as indicated in

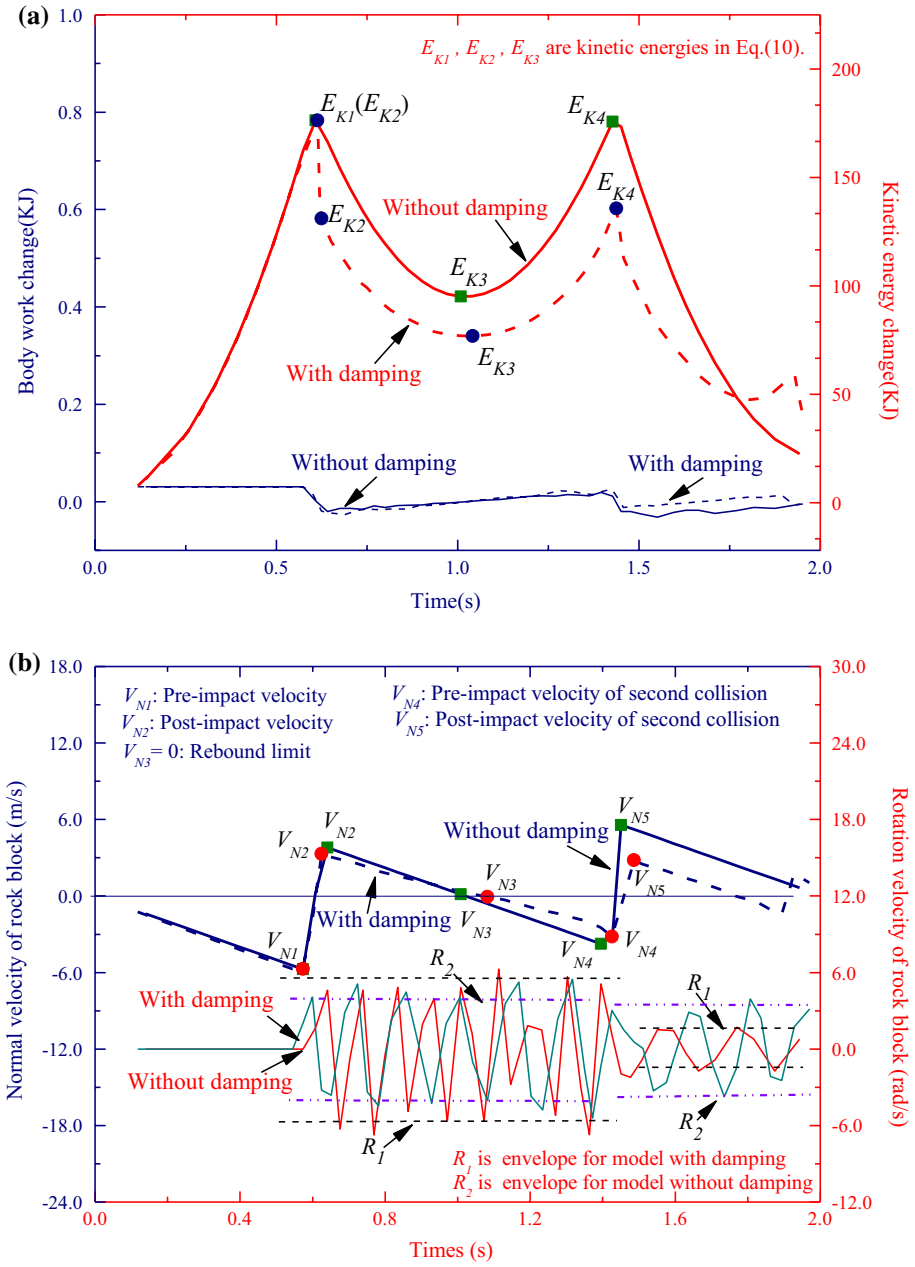

Fig. 12 Energy and velocity obtained by 3D reconstructed models with different damps: **a** Energy change, **b** velocity change

Table 3. The obtained restitution coefficients in both normal and tangential directions are finally shown in Fig. 15. As shown, the normal restitution coefficients agree well with the field tests in Table 1. However, due to the consideration of the rotational effects, the tangential restitution coefficient values are higher than those measured in the field tests.

The results further indicate that the ground type can also induce variations of rockfall restitution coefficients. Such as A06 and B28 of similar incident angle, respectively, 82° and 90° in simulation, but the normal value in the cases of smooth bedrock surface is obviously higher than that in clastic sedimentary rock surface. Thus, the normal values in the cases of smooth bedrock surface are in the range of 0.6–0.7 and the tangential ones are among 0.0–0.3. Accordingly, for the clastic sedimentary rock surface cases, they are, respectively, in the range of 0.4–0.5 and 0.6–0.7. In addition, it is further indicated that the normal restitution coefficient values are greater than the tangential ones for the case of smooth bedrock surface at a given incident angle. For the clastic sedimentary bedrock case, the tangential restitution coefficients are enhanced, while the normal ones are reduced due to the energy dissipation on the impacting surface.

Therefore, the simulated normal restitution coefficients by the three-dimensional reconstruction method agree well with those of the field tests. There are some differences in the tangential restitution coefficients between the simulated

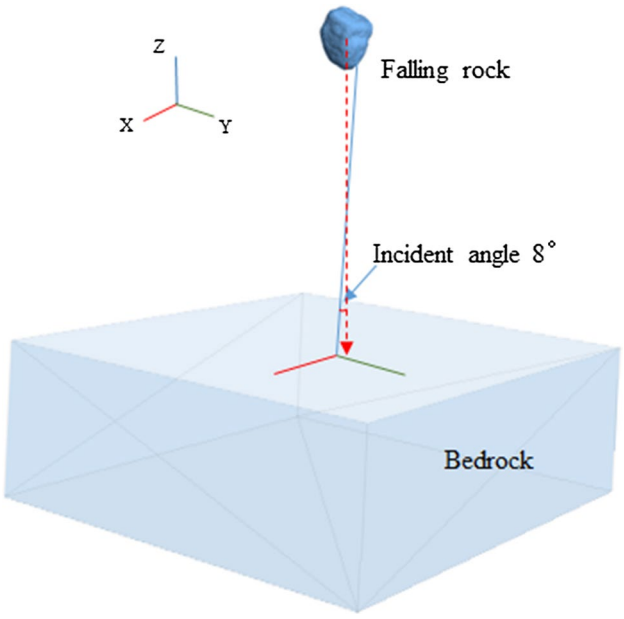

Fig. 13 Rockfall model of test A06 in Table 1 by 3D reconstruction

and field results. As simulated, falling block rotations occur during colliding and they are counted into the tangential restitution coefficient in the simulation by energy method. Hence, the simulated tangential restitution coefficients are bigger than measured ones.

5 Parameter Sensitivity Analysis

The effects of the falling block smoothness, volume, speed and incident angle, and the damp are discussed hereby for the case with smooth bedrock surface. Otherwise specified, the falling block parameter values in the following modeling are the same as given in Table 2.

5.1 Falling Block Smoothness

The evaluation of rock smoothness is based on its edge roundness, which is controlled by the degree of the spherical harmonics. Thus, three groups of rockfall tests with degree $N = 0$, 5, and 15 are simulated, respectively, to represent the sphere, pebble and rubble rocks. The colliding-rebounding velocities of the ten falling block cases in each group are shown in Fig. 16. It is observed that the rebounding velocities of the pebble cases and the rubble ones both have a great diversity, which is significantly different to the sphere cases that keep a constant rebounding velocity after multiple collisions. This phenomenon is further demonstrated in Fig. 17 that both the normal and tangential restitution coefficients decrease with increasing rockfall roundness.

Therefore, the falling block smoothness can increase the rockfall restitution coefficients, which indicates that it is very necessary to consider the falling block morphology in rockfall simulations.

5.2 Colliding Damping

The sensitivity of the restitution coefficient values to the damping is analyzed by setting the damping from zero to 0.2 for the rockfall cases with a given incident angle and the results are shown in Fig. 18.

It can be observed in Fig. 18a that the normal values are more sensitive to the normal damping than the tangential ones. For models with a given normal damping, the tangential damping introduced constraints the falling block rotation and thus contributes to the increase in the normal constitution coefficient. The normal restitution coefficient may not get the maximum point even when the damping is zero. It is mainly due to the presence of the angles between the falling rocks and the impacted ground surface, as well as between its falling centroid and trace.

It is shown in Fig. 18b that the values of tangential restitution coefficients decrease with the increase in both normal and tangential damping. However, the tangential values can get the maximum point when the damping is zero.

Therefore, the rockfall restitution coefficients are sensitive to both normal and tangential damping.

5.3 Incident Velocity and Volume

As shown in Fig. 19a, the normal restitution coefficients show a gentle change with increasing incident velocity of falling rocks. While the tangential ones experience firstly an increase phase and then a decrease phase. It can be explained that the increase in incident velocity reduces the ratio of the rotational energy in the total kinetic energy. Figure 19b suggests that the volume change does not show an evident effect on the rockfall restitution coefficients under the tested condition. These conclusions agree well with the precedent findings (Day 1997) for small blocks of falling rocks.

5.4 Incident Angle

The sensitivity of the restitution coefficients to the incident angle is studied by setting the normal and tangential incident angle in the range of −30° to 30°. The variations of restitution coefficient values are shown in Fig. 20 with respect to the normal and tangential incident angles.

It is seen in Fig. 20a that there is a pair of normal and tangential incident angle values at which the normal restitution coefficient reaches its maximum value of 0.65. Similarly, in Fig. 20b, there is a pair of normal and tangential angle at which the tangential restitution coefficient

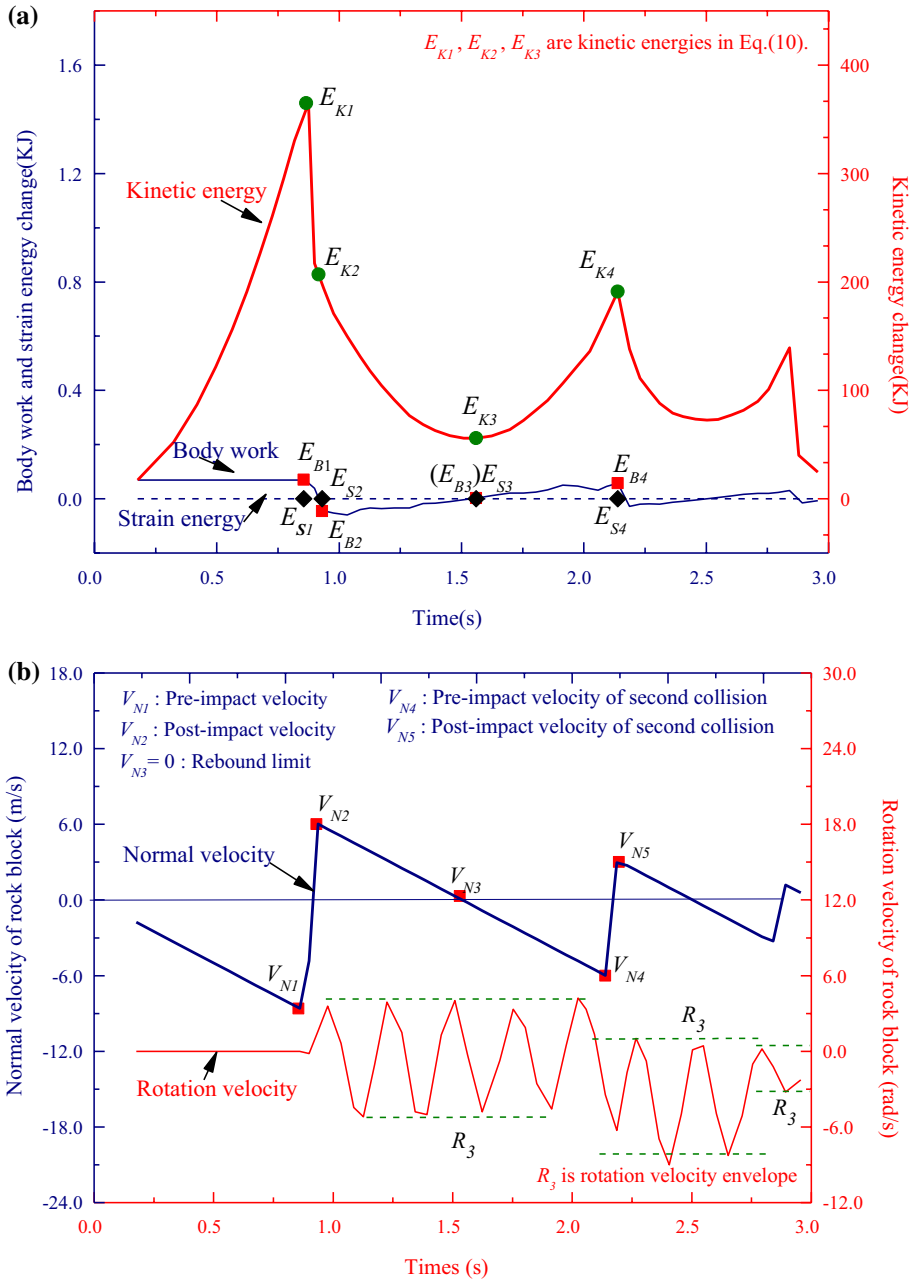

Fig. 14 Impacting rock energy and velocity obtained by 3D reconstructed model for test A06 in Table 1: **a** energy change, **b** velocity change

reaches its maximum value of 0.85 at the given condition. Thus, the restitution coefficient is very sensitive to the incident angle and can reach its peak value at a pair of given incident angles.

The normal and tangential restitution coefficient values obtained by the three-dimensional modeling primarily fall, respectively, within (0.1, 0.5) and (0.4, 0.9) as shown in Fig. 20. These values generally accord with the results of a former work (Guzzetti et al. 2002).

6 Discussion

The three-dimensional reconstruction method presented in this paper has obvious advantages in investigating the effects of falling block morphology and rotational effects on block impact analysis. The possible way to incorporate the effects of rockfall morphology in rockfall propagation tools is to establish an instance library that presents

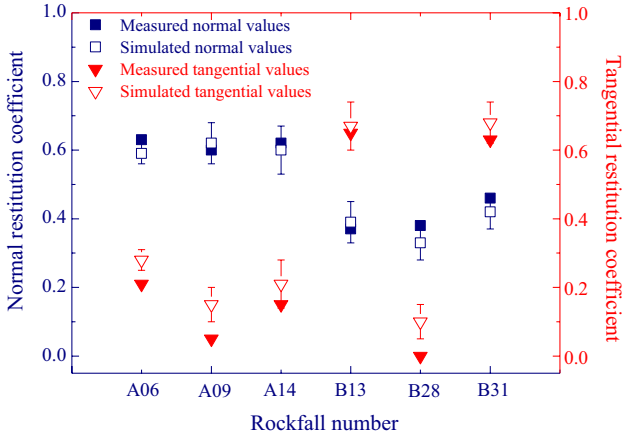

Fig. 15 Restitution coefficients of rockfall cases

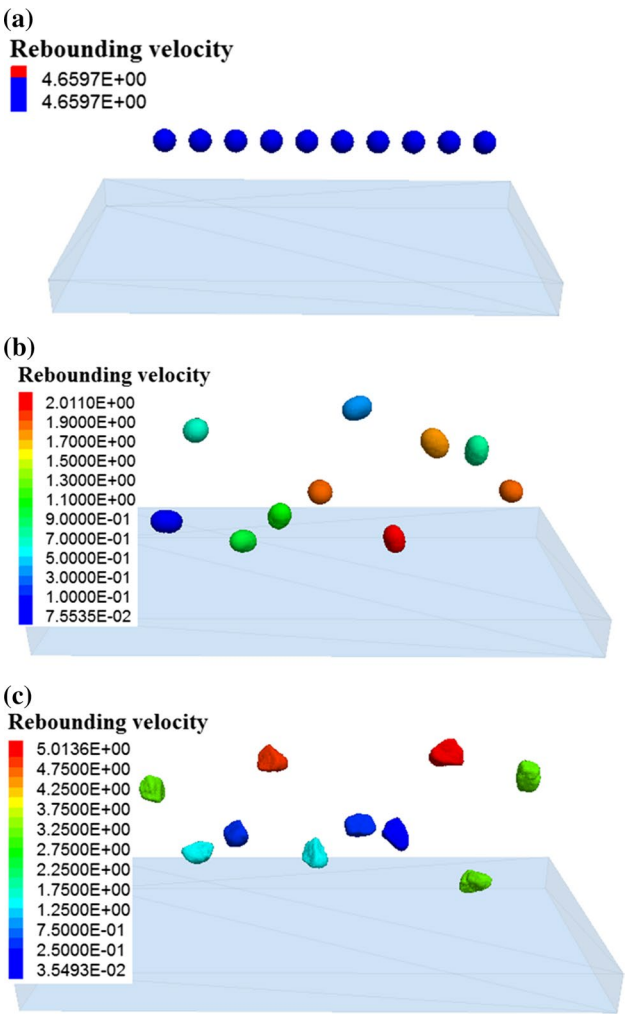

Fig. 16 Rebounding velocity of falling rocks with different smoothness after the first colliding-rebounding process: **a** sphere, **b** pebble, **c** rubble

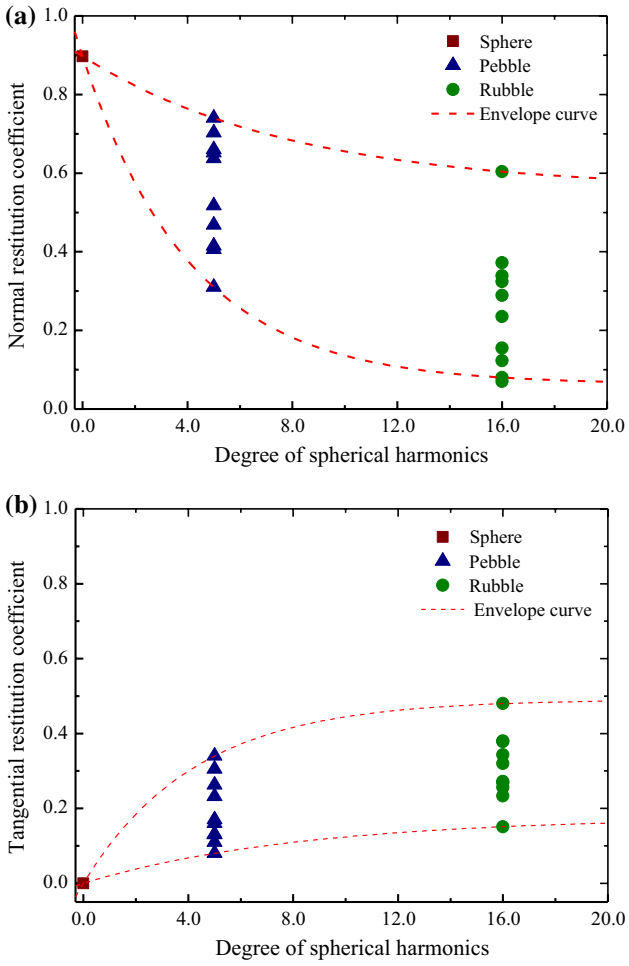

Fig. 17 Sensitivity of restitution coefficient of rockfall to rocks smoothness: **a** normal restitution coefficient, **b** tangential restitution coefficient

the basic morphology models for rockfall modeling based on the commonly observed rockfall cases. This instance library can be updated with new data if new models of rockfall cases are available. This morphology library can be then incorporated in the rockfall modeling tools for modeling blocks in falling rock projectile analysis.

If the block morphology is incorporated in the rockfall simulation tools, the rotational effects can be systematically taken into account during impacts. It is advantageous to what is done in hybrid rockfall simulation methods (Bourrier et al. 2009) that a large data set of numerical impacts are needed for statistical analysis purpose to reasonably consider the rotational effects. Therefore, the obtained realistic numerical model of block to soil impact can avoid the time-consuming statistical analysis of numerical impacts with the proposed method.

In addition, the three-dimensional reconstruction approach can be extended to investigate the effect of the block morphology on rockfall protection structures, either

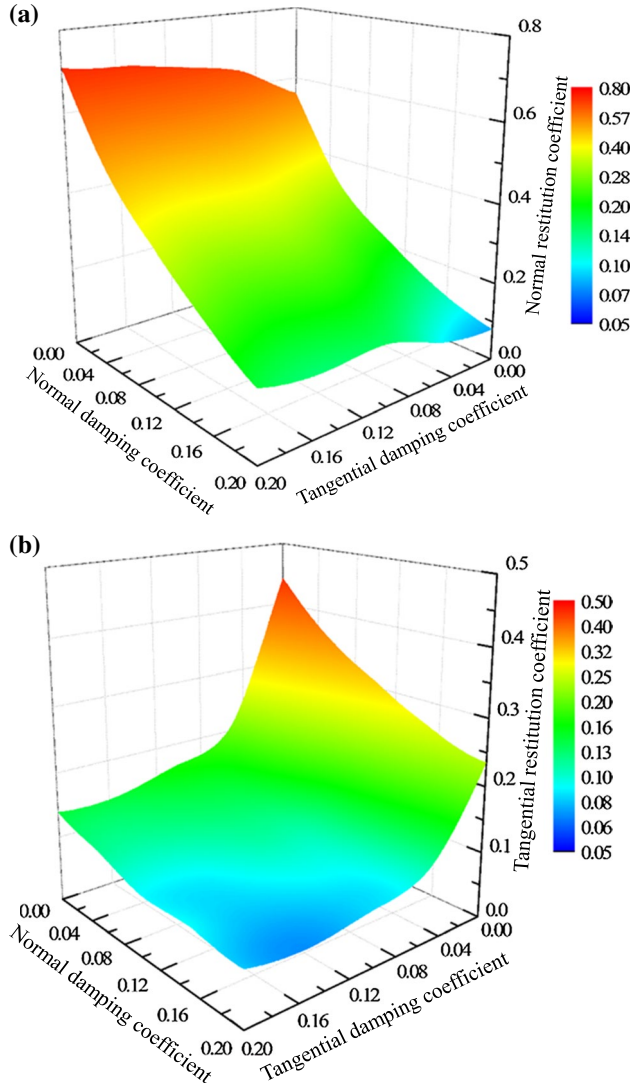

Fig. 18 Sensitivity of restitution coefficient to damps: **a** Normal restitution coefficient change, **b** tangential restitution coefficient change

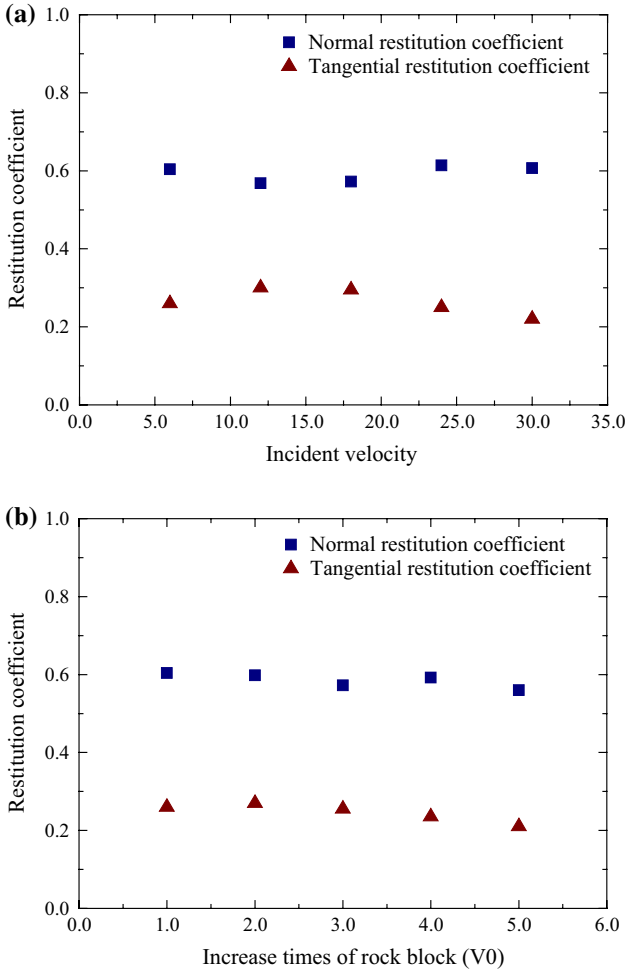

Fig. 19 Sensitivity of restitution coefficient to incident velocity and block volume: **a** impacting rocks with different incident velocity values, **b** impacting rocks with different volumes

rigid or flexible. A suitable description of the block morphology is indispensable for fragmentation study of blocks upon impact (Giacomini et al. 2009). Thus, a further possible application of the three-dimensional reconstruction method can be also related to the fragmentation modeling of blocks upon impact, which is a crucial aspect but traditionally neglected in rockfall analysis.

However, similar to other discrete modeling methods, the proposed method suffers from computing cost in modeling real scale applications. In the current modeling of a block impact to rigid boundary, it takes about 4 h in an updated personal PC for generating the block with 1500 particles and simulating the impact process with the particle flow method including the parameter calibration. If more particles are generated, it will take more time. Therefore, the extension of the modeling method from block scale to slope scale requires substantial computing cost in the reconstruction and computing of the particles. In addition, the energy dissipation is considered only by damping in the current study. For realistic rockfall cases, friction is also an important energy dissipation mechanism, especially for impact of boulders upon boundaries. Hence, further study to incorporate the friction mechanism in the modeling method is necessary.

7 Conclusion

Based on the investigation, conclusions can be drawn as follows:

(1) The degree of spherical harmonics enhances the precision of the reconstructed microscopic characteristics of the falling block outer contour. For a complicated morphology, the higher reconstruction degree can induce

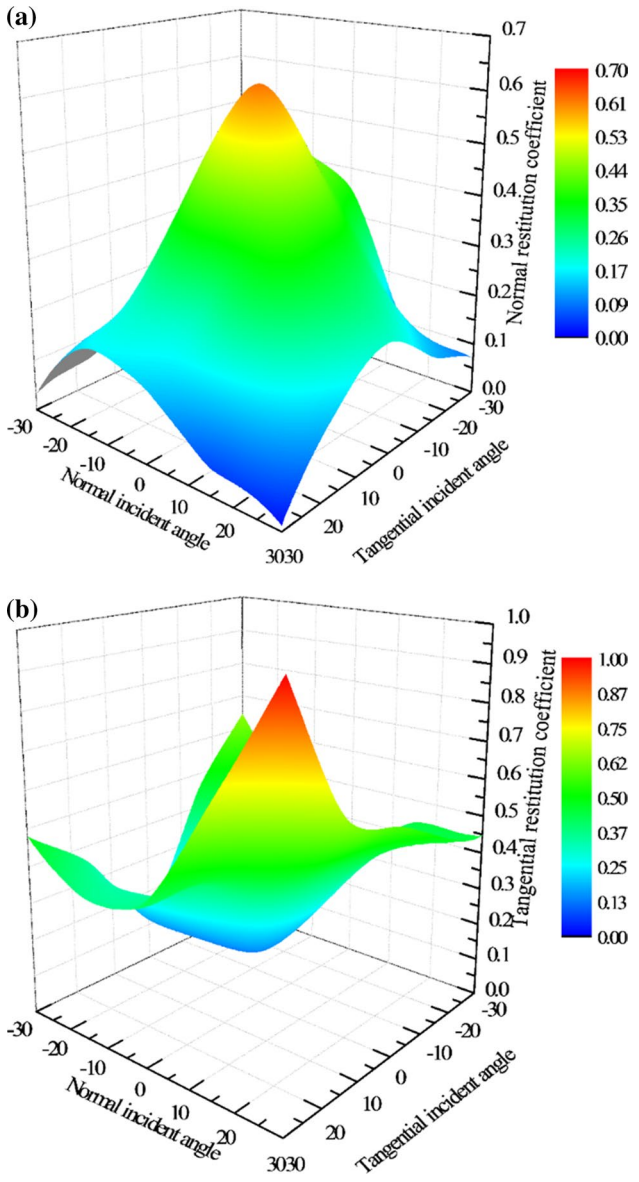

Fig. 20 Variation of rockfall restitution coefficient with incident angles: **a** Normal restitution coefficient change, **b** tangential restitution coefficient change

a greater divergence of rockfall restitution coefficient than the lower ones due to the effect of rock surface smoothness in collision.

(2) The three-dimensional reconstruction model is advantageous to the commonly used spherical models since it can consider the micromorphology of falling rocks, and the falling block rotation can be thus simulated during the impact of rockfall.

(3) There is a critical incident angle, at which no rockfall rotation occurs after collision and the normal restitution coefficient reaches its peak value. Damping method can be used for energy dissipation mechanism for the impact of hard falling block onto the bedrock surface. The rockfall is co-affected by both the normal and tangential damping and thus the models with only a single damping induces great errors.

(4) The incident velocities show some influences on the restitution coefficient values, but its volume change shows few influence.

Acknowledgements The work is partially supported by the National Basic Research Program of China (973 Program) (Grant No. 2015CB057903), which is acknowledged. The authors are grateful to the anonymous reviewers and the journal editors for their constructive comments and suggestions that have greatly improved the paper.

References

An B, Tannant DD (2007) Discrete element method contact model for dynamic simulation of inelastic rock impact. Comput Geosci 33(4):513–521

Ansari M, Ahmad M, Singh R, Singh T (2012) Rockfall assessment near Saptashrungi Gad temple, Nashik, Maharashtra, India. Int J Disaster Risk Reduc 2:77–83

Ansari M, Ahmad M, Singh R, Singh T (2015) Correlation between Schmidt hardness and coefficient of restitution of rocks. J Afr Earth Sci 104:1–5

Asteriou P, Saroglou H, Tsiambaos G (2012) Geotechnical and kinematic parameters affecting the coefficients of restitution for rock fall analysis. Int J Rock Mech Min Sci 54:103–113

Azzoni A, La Barbera G, Zaninetti A (1995) Analysis and prediction of rockfalls using a mathematical model. In: International Journal of Rock Mechanics and Mining Sciences & Geomechanics Abstracts, 1995. vol 7. Elsevier, pp 709–724

Bourrier F, Eckert N, Bellot H, Heymann A, Nicot F, Darve F (2008a) Numerical modelling of physical processes involved during the impact of a rock on a coarse soil. Adv Geomater Struct 501–506

Bourrier F, Nicot F, Darve F (2008b) Physical processes within a 2D granular layer during an impact. Granular Matter 10(6):415–437

Bourrier F, Dorren L, Nicot F, Berger F, Darve F (2009) Toward objective rockfall trajectory simulation using a stochastic impact model. Geomorphology 110(3):68–79

Chau K, Wong R, Liu J, Wu J, Lee C (1999) Shape effects on the coefficient of restitution during rockfall impacts. In: 9th ISRM Congress, 1999. International Society for Rock Mechanics,

Chau K, Wong R, Wu J (2002) Coefficient of restitution and rotational motions of rockfall impacts. Int J Rock Mech Min Sci 39(1):69–77

Cundall PA, Strack OD (1979) A discrete numerical model for granular assemblies. Geotechnique 29(1):47–65

Das N, Giordano P, Barrot D, Mandayam S, Sukumaran B, Ashmawy AK (2008) Discrete element modeling and shape characterization of realistic granular shapes. In: The Eighteenth International Offshore and Polar Engineering Conference, 2008. International Society of Offshore and Polar Engineers

Day RW (1997) Case studies of rockfall in soft versus hard rock. Environ Eng Geosci 3(1):133–140

de Almeida JA, Kullberg JC (2011) Rockfall hazard and risk analysis for Monte da Lua, Sintra, Portugal. Nat Hazards 58(1):289–310

Deng S, Li H, Ma G, Huang H, Li X (2014) Simulation of shale–proppant interaction in hydraulic fracturing by the discrete element method. Int J Rock Mech Min Sci 70:219–228

Evans SG, Hungr O (1993) The assessment of rockfall hazard at the base of talus slopes. Can Geotech J 30(4):620–636. https://doi.org/10.1139/t93-054

Giacomini A, Buzzi O, Renard B, Giani G (2009) Experimental studies on fragmentation of rock falls on impact with rock surfaces. Int J Rock Mech Min Sci 46(4):708–715

Giacomini A, Thoeni K, Lambert C, Booth S, Sloan S (2012) Experimental study on rockfall drapery systems for open pit highwalls. Int J Rock Mech Min Sci 56:171–181

Giani G, Giacomini A, Migliazza M, Segalini A (2004) Experimental and theoretical studies to improve rock fall analysis and protection work design. Rock Mech Rock Eng 37(5):369–389

Guzzetti F, Crosta G, Detti R, Agliardi F (2002) STONE: a computer program for the three-dimensional simulation of rock-falls. Comput Geosci 28(9):1079–1093

Itasca C (1999) PFC 3D-User manual. Itasca Consulting Group, Minneapolis

Jiang M, Yu HS, Leroueil S (2007) A simple and efficient approach to capturing bonding effect in naturally microstructured sands by discrete element method. Int J Numer Methods Eng 69(6):1158–1193

Jiang M, Yan H, Zhu H, Utili S (2011) Modeling shear behavior and strain localization in cemented sands by two-dimensional distinct element method analyses. Comput Geotech 38(1):14–29

PFC2D I (1999) Particle flow code in 2 dimensions. theory and background, Itasca Consulting Group, Minneapolis, MN:1-124

Pfeiffer TJ, Bowen TD (1989) Computer Simulation of Rockfalls. Bulletin of the Association of Engineering Geologists xxvi 1:135–146. https://doi.org/10.2113/gseegeosci.xxvi.1.135

Pöschel T, Schwager T (2005) Computational granular dynamics: models and algorithms. Springer, Berlin

Potyondy D, Cundall P (2004) A bonded-particle model for rock. Int J Rock Mech Min Sci 41(8):1329–1364

Richards LR (1988) Rockfall protection: A review of current analytical and design methods. Paper presented at the Meeting on Rockfall Dynamics and Protective Works Effectiveness, Politecnico di Torino

Shi C, Zhang Y-L, Xu W-Y, Zhu Q-Z, Wang S-N (2013) Risk analysis of building damage induced by landslide impact disaster. Eur J Environ Civ Eng 17(sup1):s126–s143

Shi C, Li D-j Xu, W-y Wang R (2015) Discrete element cluster modeling of complex mesoscopic particles for use with the particle flow code method. Granular Matter 17(3):377–387

Shi C, Shen J, Xu W-Y, Wang R, Wang W (2016) Micromorphological characterization and random reconstruction of 3D particles based on spherical harmonic analysis. J Cent South Univ 24(5):1197–1206

Thoeni K, Giacomini A, Lambert C, Sloan SW, Carter JP (2014) A 3D discrete element modelling approach for rockfall analysis with drapery systems. Int J Rock Mech Min Sci 68:107–119

Wei L-W, Chen H, Lee C-F, Huang W-K, Lin M-L, Chi C-C, Lin H-H (2014) The mechanism of rockfall disaster: a case study from Badouzih, Keelung, in northern Taiwan. Eng Geol 183:116–126

Woltjer M, Rammer W, Brauner M, Seidl R, Mohren G, Lexer M (2008) Coupling a 3D patch model and a rockfall module to assess rockfall protection in mountain forests. J Environ Manage 87(3):373–388

Zhang G, Xiang X, Tang H (2011) Field test and numerical calculation of restitution coefficient of rockfall collision. Chin J Rock Mech Eng 30(6):1266–1273

Zhou B, Wang J, Zhao B (2015) Micromorphology characterization and reconstruction of sand particles using micro X-ray tomography and spherical harmonics. Eng Geol 184:126–137

Chapter V

Conclusions and Perspectives

The main objective of this these is the extension and application of the discrete approach in solving some rock engineering problems, such as studies on mechanical behavior of cohesive rocks, hydraulic fracturing, and rockfall analysis.

Firstly for the purpose of describing mechanical strength and deformation of cohesive rocks like sandstone, a nonlinear failure criterion for inter-granular interface bonding is proposed and implemented in the particle flow code. After calibration of the proposed bond model using triaxial compression tests performed on representative sandstone, different type of tests have been carried out. The results show that,

1. The proposed bond model has the ability to describe strength and deformation of granular materials for a wide range of stresses, overcoming the problem that the overall strength of cohesive materials cannot be described by linear bond models such as contact bond model and parallel bond model.

2. Under the conventional compression condition, the tensile cracking is controlling the failure process under low confining pressure, while the shearing cracking becomes the dominating process when the confining pressure is high. There is a clear transition from a brittle to ductile behavior with the increase in confining pressure.

3. The loading path, as well as the intermediate stress, have important effects on deformation and failure of cohesive rock materials.

Secondly, in order to further investigate deformation and failure of anisotropic rocks, the proposed nonlinear failure criterion has been introduced in the framework of two coupled bond models, the bond model and the smooth joint model. Based on an effective procedure for characterizing micro-layer-structure in anisotropic materials, a large number of anisotropy investigations against mechanical strength and deformation have been performed on a representative inherent anisotropic material: Tournemire shale. Numerical

results are in good agreement with experimental data and show that,

1. The inherent properties of weakness layers as well as confining pressure both have significantly influences on macroscopic mechanical behaviors of anisotropic rocks.

2. The failure process is controlled by the weakness layer properties for low confining pressure, but is dependent on the combination role of weakness layers and rock matrix properties under high confining pressure.

3. The intermediate principal stress can also influence the strength and deformation. With the intermediate stress increase, the pressure-dependency of macroscopic strength will decrease and the failure model has a clear transition to a shear failure mode.

Thirdly, the hydraulic fracturing process in cohesive materials has been studied using the proposed bond model by considering effects of pore fluid pressure on strength and deformation of porous rocks. Effects of confining pressure, fluid viscosity and injection rate on fluid breakdown pressure and failure process have been investigated and the obtained results show that,

1. The comparisons between analytical solution of the breakdown pressure and numerical results show a good agreement and further demonstrate that, the modified fluid-coupled algorithm has the applicability to analyze the hydraulic fracturing process in cohesive materials.

2. With the increase of differential stress, the breakdown pressure significantly decreases and the propagation direction of hydraulic fractures is gradually close to the orientation of the maximum principal stress.

3. When the fluid viscosity is low, it can more easily penetrate through the interconnected spaces from the fracture into rock leading to that the breakdown pressure decreases and the fluid infiltration surface increases. Compared to fluid viscosity, the injection rate has a significant effect on breakdown pressure as well as hydraulic fracture propagation.

Finally, in the application of discrete approach for rockfall analysis, a series of numerical simulations have been performed to study the block impact to the bedrock and the obtained results show that,

1. For a complicated morphology, the higher reconstruction degree can induce a greater divergence of rockfall restitution coefficient than the lower ones due to the effect of rock surface smoothness in collision

2. The three-dimensional reconstruction model is advantageous to the commonly used spherical models since it can consider the micromorphology of falling rocks, and the falling block rotation can be thus simulated during the impact of rockfall.

3. The rockfall morphology, surface characteristics, velocity, and volume, colliding

damping and relative angle have different influences on restitution coefficients.

Moment effect at contact between particles should play an important role in application of the particle flow code to describe strength and deformation of cohesive granular materials, and this issue will be investigated in future studies. Three-dimensional numerical analyses should be developed in order to investigate geometrical effects on hydraulic fracturing process. As for rockfall analysis, the impacted bedrock has an obvious nonlinear property, further works remain to be carried out for considering this feature.

Bibliography

[Al-Busaidi et al., 2005] Al-Busaidi, A., Hazzard, J., and Young, R. (2005). Distinct element modeling of hydraulically fractured lac du bonnet granite. *Journal of Geophysical Research: Solid Earth*, 110(B6).

[Alshkane et al., 2017] Alshkane, Y., Marshall, A. M., and Stace, L. (2017). Prediction of strength and deformability of an interlocked blocky rock mass using udec. *Journal of Rock Mechanics and Geotechnical Engineering*, 9(3):531–542.

[Amadei and Savage, 1989] Amadei, B. and Savage, W. Z. (1989). Anisotropic nature of jointed rock mass strength. *Journal of Engineering Mechanics*, 115(3):525–542.

[Chen et al., 2015] Chen, Y., Nagaya, Y., and Ishida, T. (2015). Observations of fractures induced by hydraulic fracturing in anisotropic granite. *Rock Mechanics and Rock Engineering*, 48(4):1455–1461.

[Chiu et al., 2013] Chiu, C.-C., Wang, T.-T., Weng, M.-C., and Huang, T.-H. (2013). Modeling the anisotropic behavior of jointed rock mass using a modified smooth-joint model. *International Journal of Rock Mechanics and Mining Sciences*, 62:14–22.

[Cho et al., 2012] Cho, J.-W., Kim, H., Jeon, S., and Min, K.-B. (2012). Deformation and strength anisotropy of asan gneiss, boryeong shale, and yeoncheon schist. *International Journal of Rock Mechanics and Mining Sciences*, 50:158–169.

[Chu et al., 2013] Chu, W., Zhang, C., Hou, J., et al. (2013). A particle-based model for studying anisotropic strength and deformation of schist. In *ISRM SINOROCK 2013*, pages 60–69. International Society for Rock Mechanics and Rock Engineering.

[Cundall, 2004] Cundall, P. (2004). Pfc2d user's manual (version 3.1). *Minnesota: Itasca Consulting Group Inc*, 325.

[Cundall, 2008] Cundall, P. (2008). Pfc2d user's manual (version 4.0). *Minnesota: Itasca Consulting Group Inc.*

[Cundall and Strack, 1979] Cundall, P. A. and Strack, O. D. (1979). A discrete numerical model for granular assemblies. *geotechnique*, 29(1):47–65.

[Dahi-Taleghani et al., 2011] Dahi-Taleghani, A., Olson, J. E., et al. (2011). Numerical modeling of multistranded-hydraulic-fracture propagation: Accounting for the interaction between induced and natural fractures. *SPE journal*, 16(03):575–581.

[Dahi Taleghani et al., 2013] Dahi Taleghani, A., Olson, J. E., et al. (2013). How natural fractures could affect hydraulic-fracture geometry. *SPE Journal*, 19(01):161–171.

[Debecker and Vervoort, 2013] Debecker, B. and Vervoort, A. (2013). Two-dimensional discrete element simulations of the fracture behaviour of slate. *International Journal of Rock Mechanics and Mining Sciences*, 61:161–170.

[DU et al., 2008] DU, C.-z., MAO, X.-b., and BU, W.-k. (2008). Analysis of fracture propagation in coal seams during hydraulic fracturing [j]. *Journal of Mining & Safety Engineering*, 2:023.

[Duan and Kwok, 2015] Duan, K. and Kwok, C. (2015). Discrete element modeling of anisotropic rock under brazilian test conditions. *International Journal of Rock Mechanics and Mining Sciences*.

[Duveau et al., 1998] Duveau, G., Shao, J., and Henry, J. (1998). Assessment of some failure criteria for strongly anisotropic geomaterials. *Mechanics of Cohesive-frictional Materials: An International Journal on Experiments, Modelling and Computation of Materials and Structures*, 3(1):1–26.

[Eshiet et al., 2013] Eshiet, K. I., Sheng, Y., and Ye, J. (2013). Microscopic modelling of the hydraulic fracturing process. *Environmental earth sciences*, 68(4):1169–1186.

[Fairhurst, 2003] Fairhurst, C. (2003). Stress estimation in rock: a brief history and review. *International Journal of Rock Mechanics and Mining Sciences*, 40(7-8):957–973.

[Fatahi et al., 2017] Fatahi, H., Hossain, M. M., and Sarmadivaleh, M. (2017). Numerical and experimental investigation of the interaction of natural and propagated hydraulic fracture. *Journal of Natural Gas Science and Engineering*, 37:409–424.

[Fjær and Nes, 2014] Fjær, E. and Nes, O.-M. (2014). The impact of heterogeneity on the anisotropic strength of an outcrop shale. *Rock mechanics and rock engineering*, 47(5):1603–1611.

[Gao et al., 2014] Gao, F., Stead, D., and Kang, H. (2014). Simulation of roof shear failure in coal mine roadways using an innovative udec trigon approach. *Computers and Geotechnics*, 61:33–41.

[Gu et al., 2010] Gu, H., Weng, X., et al. (2010). Criterion for fractures crossing frictional interfaces at non-orthogonal angles. In *44th US rock mechanics symposium and 5th US-Canada rock mechanics symposium*, pages 1–6. American Rock Mechanics Association.

[Gu et al., 2012] Gu, H., Weng, X., Lund, J. B., Mack, M. G., Ganguly, U., Suarez-Rivera, R., et al. (2012). Hydraulic fracture crossing natural fracture at nonorthogonal angles: a criterion and its validation. *SPE Production & Operations*, 27(01):20–26.

[Haimson and Cornet, 2003] Haimson, B. and Cornet, F. (2003). Isrm suggested methods for rock stress estimation—part 3: hydraulic fracturing (hf) and/or hydraulic testing of pre-existing fractures (htpf). *International Journal of Rock Mechanics and Mining Sciences*, 40(7-8):1011–1020.

[Hamidi and Mortazavi, 2014] Hamidi, F. and Mortazavi, A. (2014). A new three dimensional approach to numerically model hydraulic fracturing process. *Journal of Petroleum Science and Engineering*, 124:451–467.

[Hazzard et al., 2002] Hazzard, J. F., Young, R. P., and Oates, S. J. (2002). Numerical modeling of seismicity induced by fluid injection in a fractured reservoir. In *Mining and Tunnel Innovation and Opportunity, Proceedings of the 5th North American Rock Mechanics Symposium, Toronto, Canada*, pages 1023–1030. Citeseer.

[He et al., 2018] He, J., Afolagboye, L. O., Lin, C., and Wan, X. (2018). An experimental investigation of hydraulic fracturing in shale considering anisotropy and using freshwater and supercritical co2. *Energies*, 11(3):557.

[He et al., 2017] He, P.-f., Kulatilake, P. H., Yang, X.-x., Liu, D.-q., and He, M.-c. (2017). Detailed comparison of nine intact rock failure criteria using polyaxial intact coal strength data obtained through pfc3d simulations. *Acta Geotechnica*, pages 1–27.

[Hoek and Brown, 1980] Hoek, E. and Brown, E. T. (1980). *Underground excavations in rock*. CRC Press.

[Itasca, 1999] Itasca, C. (1999). Pfc 3d-user manual. *Itasca Consulting Group, Minneapolis*.

[Jaeger, 1960] Jaeger, J. (1960). Shear failure of anistropic rocks. *Geological Magazine*, 97(1):65–72.

[Jiang et al., 2011] Jiang, M., Yan, H., Zhu, H., and Utili, S. (2011). Modeling shear behavior and strain localization in cemented sands by two-dimensional distinct element method analyses. *Computers and Geotechnics*, 38(1):14–29.

[Kwok et al., 2014] Kwok, C., Duan, K., Tham, L., et al. (2014). Numerical simulation of strength and deformation behavior of inherently anisotropic rocks. In *48th US Rock Mechanics/Geomechanics Symposium*. American Rock Mechanics Association.

[Lee and Pietruszczak, 2008] Lee, Y.-K. and Pietruszczak, S. (2008). Application of critical plane approach to the prediction of strength anisotropy in transversely isotropic rock masses. *International Journal of Rock Mechanics and Mining Sciences*, 45(4):513–523.

[Li and Chen, 2016] Li, X. and Chen, J. (2016). The implementation of the extended cohesive damage model for multicrack evolution in laminated composites. *Composite Structures*, 139:68–76.

[Ma et al., 2017a] Ma, X., Zhou, T., and Zou, Y. (2017a). Experimental and numerical study of hydraulic fracture geometry in shale formations with complex geologic conditions. *Journal of Structural Geology*, 98:53–66.

[Ma et al., 2017b] Ma, X., Zou, Y., Li, N., Chen, M., Zhang, Y., and Liu, Z. (2017b). Experimental study on the mechanism of hydraulic fracture growth in a glutenite reservoir. *Journal of Structural Geology*, 97:37–47.

[Manuals, 2008] Manuals, P. (2008). Pfc 3d-user manual, verison 4.0 itasca consulting group inc. *Minneapolis, MI*.

[Mehranpour and Kulatilake, 2016] Mehranpour, M. H. and Kulatilake, P. H. (2016). Comparison of six major intact rock failure criteria using a particle flow approach under true-triaxial stress condition. *Geomechanics and Geophysics for Geo-Energy and Geo-Resources*, 2(4):203–229.

[Mehranpour and Kulatilake, 2017] Mehranpour, M. H. and Kulatilake, P. H. (2017). Improvements for the smooth joint contact model of the particle flow code and its applications. *Computers and Geotechnics*, 87:163–177.

[Motamedi and Mohammadi, 2012] Motamedi, D. and Mohammadi, S. (2012). Fracture analysis of composites by time independent moving-crack orthotropic xfem. *International Journal of Mechanical Sciences*, 54(1):20–37.

[Munjiza et al., 1995] Munjiza, A., Owen, D., and Bicanic, N. (1995). A combined finite-discrete element method in transient dynamics of fracturing solids. *Engineering computations*, 12(2):145–174.

[Nagel et al., 2013] Nagel, N., Sanchez-Nagel, M., Zhang, F., Garcia, X., and Lee, B. (2013). Coupled numerical evaluations of the geomechanical interactions between a hydraulic fracture stimulation and a natural fracture system in shale formations. *Rock mechanics and rock engineering*, 46(3):581–609.

[Nasehi and Mortazavi, 2013] Nasehi, M. J. and Mortazavi, A. (2013). Effects of in-situ stress regime and intact rock strength parameters on the hydraulic fracturing. *Journal of Petroleum Science and Engineering*, 108:211–221.

[Niandou et al., 1997] Niandou, H., Shao, J., Henry, J., and Fourmaintraux, D. (1997). Laboratory investigation of the mechanical behaviour of tournemire shale. *International Journal of Rock Mechanics and Mining Sciences*, 34(1):3–16.

[Nova, 1980] Nova, R. (1980). The failure of transversely isotropic rocks in triaxial compression. In *International Journal of Rock Mechanics and Mining Sciences & Geomechanics Abstracts*, volume 17, pages 325–332. Elsevier.

[Olson et al., 2008] Olson, J. et al. (2008). Multi-fracture propagation modeling: Applications to hydraulic fracturing in shales and tight gas sands. In *The 42nd US rock mechanics symposium (USRMS)*, pages 1–8. American Rock Mechanics Association.

[Olson et al., 2009] Olson, J. E., Taleghani, A. D., et al. (2009). Modeling simultaneous growth of multiple hydraulic fractures and their interaction with natural fractures. In *SPE hydraulic fracturing technology conference*, pages 1–7. Society of Petroleum Engineers.

[Park and Min, 2015] Park, B. and Min, K.-B. (2015). Bonded-particle discrete element modeling of mechanical behavior of transversely isotropic rock. *International Journal of Rock Mechanics and Mining Sciences*, 76:243–255.

[Pietruszczak et al., 2002] Pietruszczak, S., Lydzba, D., and Shao, J.-F. (2002). Modelling of inherent anisotropy in sedimentary rocks. *International Journal of Solids and Structures*, 39(3):637–648.

[Potyondy and Cundall, 2004] Potyondy, D. and Cundall, P. (2004). A bonded-particle model for rock. *International journal of rock mechanics and mining sciences*, 41(8):1329–1364.

[Reinicke et al., 2010] Reinicke, A., Rybacki, E., Stanchits, S., Huenges, E., and Dresen, G. (2010). Hydraulic fracturing stimulation techniques and formation damage mechanisms—implications from laboratory testing of tight sandstone–proppant systems. *Chemie der Erde-Geochemistry*, 70:107–117.

[Sarmadivaleh and Rasouli, 2015] Sarmadivaleh, M. and Rasouli, V. (2015). Test design and sample preparation procedure for experimental investigation of hydraulic fracturing interaction modes. *Rock Mechanics and Rock Engineering*, 48(1):93–105.

[Shi et al., 2013] Shi, C., Zhang, Y.-L., Xu, W.-Y., Zhu, Q.-Z., and Wang, S.-N. (2013). Risk analysis of building damage induced by landslide impact disaster. *European Journal of Environmental and Civil Engineering*, 17(sup1):s126–s143.

[Shimizu et al., 2011] Shimizu, H., Murata, S., and Ishida, T. (2011). The distinct element analysis for hydraulic fracturing in hard rock considering fluid viscosity and particle size distribution. *International Journal of Rock Mechanics and Mining Sciences*, 48(5):712–727.

[Sosa and Karapurath, 2012] Sosa, J. C. and Karapurath, N. (2012). Delamination modelling of glare using the extended finite element method. *Composites Science and Technology*, 72(7):788–791.

[Tavallali and Vervoort, 2010] Tavallali, A. and Vervoort, A. (2010). Effect of layer orientation on the failure of layered sandstone under brazilian test conditions. *International journal of rock mechanics and mining sciences*, 47(2):313–322.

[Thiercelin et al., 2007] Thiercelin, M., Makkhyu, E., et al. (2007). Stress field in the vicinity of a natural fault activated by the propagation of an induced hydraulic fracture. In *1st Canada-US Rock Mechanics Symposium*, pages 1–9. American Rock Mechanics Association.

[Tien et al., 2006] Tien, Y. M., Kuo, M. C., and Juang, C. H. (2006). An experimental investigation of the failure mechanism of simulated transversely isotropic rocks. *International Journal of Rock Mechanics and Mining Sciences*, 43(8):1163–1181.

[Wang et al., 2017] Wang, T., Hu, W., Elsworth, D., Zhou, W., Zhou, W., Zhao, X., and Zhao, L. (2017). The effect of natural fractures on hydraulic fracturing propagation in coal seams. *Journal of Petroleum Science and Engineering*, 150:180–190.

[Wang et al., 2016] Wang, T., Xu, D., Elsworth, D., and Zhou, W. (2016). Distinct element modeling of strength variation in jointed rock masses under uniaxial compression. *Geomechanics and Geophysics for Geo-Energy and Geo-Resources*, 2(1):11–24.

[Wang et al., 2014] Wang, T., Zhou, W., Chen, J., Xiao, X., Li, Y., and Zhao, X. (2014). Simulation of hydraulic fracturing using particle flow method and application in a coal mine. *International Journal of Coal Geology*, 121:1–13.

[Yang et al., 2017] Yang, S.-Q., Chen, M., Jing, H.-W., Chen, K.-F., and Meng, B. (2017). A case study on large deformation failure mechanism of deep soft rock roadway in xin'an coal mine, china. *Engineering Geology*, 217:89–101.

[Yang et al., 2014] Yang, S.-Q., Huang, Y.-H., Jing, H.-W., and Liu, X.-R. (2014). Discrete element modeling on fracture coalescence behavior of red sandstone containing two unparallel fissures under uniaxial compression. *Engineering geology*, 178:28–48.

[Yao et al., 2016] Yao, C., Jiang, Q., Shao, J., and Zhou, C. (2016). A discrete approach for modeling damage and failure in anisotropic cohesive brittle materials. *Engineering Fracture Mechanics*, 155:102–118.

[Yao et al., 2015] Yao, C., Jiang, Q., and Shao, J.-F. (2015). Numerical simulation of damage and failure in brittle rocks using a modified rigid block spring method. *Computers and Geotechnics*, 64:48–60.

[Yun et al., 2017] Yun, K., Wang, Z., Ronald, S., and Pak, Y. (2017). An advanced continuum damage mechanics model for predicting the crack progress process based on the consideration of the influence of crack direction under quasi-static load. *International Journal of Mechanical Sciences*, 130:487–496.

[Yushi et al., 2016a] Yushi, Z., Shicheng, Z., Tong, Z., Xiang, Z., and Tiankui, G. (2016a). Experimental investigation into hydraulic fracture network propagation in gas shales using ct scanning technology. *Rock Mechanics and Rock Engineering*, 49(1):33–45.

[Yushi et al., 2016b] Yushi, Z., Xinfang, M., Shicheng, Z., Tong, Z., and Han, L. (2016b). Numerical investigation into the influence of bedding plane on hydraulic fracture network propagation in shale formations. *Rock Mechanics and Rock Engineering*, 49(9):3597–3614.

[Zeng and Yao, 2016] Zeng, Q. and Yao, J. (2016). Numerical simulation of fracture network generation in naturally fractured reservoirs. *Journal of Natural Gas Science and Engineering*, 30:430–443.

[Zeng et al., 2018] Zeng, Q.-D., Yao, J., and Shao, J. (2018). Numerical study of hydraulic fracture propagation accounting for rock anisotropy. *Journal of Petroleum Science and Engineering*, 160:422–432.

[Zhang et al., 2010] Zhang, G., Liu, H., Zhang, J., Wu, H., and Wang, X. (2010). Three-dimensional finite element simulation and parametric study for horizontal well hydraulic fracture. *Journal of Petroleum Science and Engineering*, 72(3-4):310–317.

[Zhang et al., 2017] Zhang, L., Zhou, J., and Han, Z. (2017). Hydraulic fracturing process by using a modified two-dimensional particle flow code-case study. *Progress in Computational Fluid Dynamics, an International Journal*, 17(1):13–26.

[Zhang et al., 2018a] Zhang, Y., Liu, Z., Shi, C., and Shao, J. (2018a). Three-dimensional reconstruction of block shape irregularity and its effects on block impacts using an energy-based approach. *Rock Mechanics and Rock Engineering*, 51(4):1173–1191.

[Zhang et al., 2018b] Zhang, Y., Shao, J., Liu, Z., Shi, C., and De Saxcé, G. (2018b). Effects of confining pressure and loading path on deformation and strength of cohesive granular materials: a three-dimensional dem analysis. *Acta Geotechnica*, pages 1–18.

[Zhao et al., 2016] Zhao, L., Zhi, J., Zhang, J., Liu, Z., and Hu, N. (2016). Xfem simulation of delamination in composite laminates. *Composites Part A: Applied Science and Manufacturing*, 80:61–71.

[Zhao and Paul Young, 2011] Zhao, X. and Paul Young, R. (2011). Numerical modeling of seismicity induced by fluid injection in naturally fractured reservoirs. *Geophysics*, 76(6):WC167–WC180.

[Zhou et al., 2008] Zhou, J., Chen, M., Jin, Y., and Zhang, G.-q. (2008). Analysis of fracture propagation behavior and fracture geometry using a tri-axial fracturing system in naturally fractured reservoirs. *International Journal of Rock Mechanics and Mining Sciences*, 45(7):1143–1152.

[Zhou et al., 2017a] Zhou, J., Zhang, L., and Han, Z. (2017a). Hydraulic fracturing process by using a modified two-dimensional particle flow code-method and validation. *Progress in Computational Fluid Dynamics, an International Journal*, 17(1):52–62.

[Zhou et al., 2017b] Zhou, J., Zhang, L., Pan, Z., and Han, Z. (2017b). Numerical studies of interactions between hydraulic and natural fractures by smooth joint model. *Journal of Natural Gas Science and Engineering*, 46:592–602.

[Zhu et al., 2016] Zhu, H., Nguyen, H. N., Nicot, F., and Darve, F. (2016). On a common critical state in localized and diffuse failure modes. *Journal of the Mechanics and Physics of Solids*, 95:112–131.

[Zou et al., 2016] Zou, Y., Zhang, S., Ma, X., Zhou, T., and Zeng, B. (2016). Numerical investigation of hydraulic fracture network propagation in naturally fractured shale formations. *Journal of Structural Geology*, 84:1–13.